POLITECNICO
MILANO 1863

School of Industrial and Information Engineering
Laurea Magistrale (M.Sc.) in Engineering Physics

Femtosecond laser writing of an integrated optical chip for quantum simulation

Supervisor: Dr. Roberto **Osellame**
Co-supervisor: Dr. Simone **Atzeni**

Candidate: Alessandro **Prencipe**
Student ID: 877285

Academic Year 2017/2018

Abstract

Quantum technology is a relatively new and rapidly developing field. There are several physical platforms which are considered to be promising for implementing a quantum hardware: encouraging results have been achieved using, among the others, cold atoms, trapped ions, superconductive circuits and photons. This Thesis deals with the realization of a reconfigurable integrated optical device which is going to be the core component of an experiment consisting in the photonic quantum simulation of many body systems, in particular of the Benzene molecule. The chip was fabricated using the femtosecond laser micromachining technique on a borosilicate glass substrate. Two metallic layer of Chromium and Gold were deposited on the surface of glass and thermal phase shifters were machined on it, in order to obtain a full reconfigurability of the optical circuit.

A classical characterization of the device showed the good properties of the chip both in terms of transmission and reconfigurability. The reproducibility of the new fabrication processes, developed to meet the stringent specifications needed for the quantum experiment, was also tested through the many prototypes realized before the final device.

Sommario

Negli ultimi decenni sono stati implementati diversi prototipi di computer quantistici, tuttavia la realizzazione di una macchina quantistica "universale", in grado di svolgere qualsiasi tipo di computazione, è ancora una sfida irrisolta. Lo stato dell'arte della tecnologia consente la realizzazione di sistemi "ad hoc" in grado di trattare problemi circoscritti: si parla di simulatori quantistici analogici. Essi poterebbero esser visti come l'equivalente odierno di quello che furono i circuiti elettrici usati nel secolo scorso per trovare una soluzione in modo non analitico di equazioni differenziali altrimenti non facilmente risolvibili.

Esistono diversi esempi di simulatori quantistici realizzati sfruttando singoli fotoni come quantum bits. Quel che rende i fotoni buoni quantum bits è il fatto che essi tendono ad interagire poco con l'ambiente e pertanto conservano il loro stato coerente senza perdere l'informazione che trasportano. D'altro canto sistemi ottici bulk sono soggetti a vibrazioni ed intrinsecamente limitati in termini di scalabilità, per questo, al fine di aumentare la complessità delle simulazioni implementate, si rende necessario il passaggio all'uso di circuiti ottici integrati. Questi sono assai più compatti e, essendo oggetti monolitici, sono anche più resilienti a perturbazioni esterne. Tuttavia una delle principali limitazioni dei circuiti ottici integrati nelle applicazioni in ottica quantistica sono le alte perdite, che possono portare a tempi estremamente lunghi per la realizzazione della misura.

L'obiettivo di questa Tesi è stato la fabbricazione di un dispositivo ottico integrato e riconfigurabile a basse perdite che possa esser utilizzato come simulatore quantistico analogico per ottenere una misura dell'energia dello stato fondamentale e di alcuni stati eccitati del Benzene. Trattandosi di un circuito completamente riconfigurabile, esso potrà esser adoperato per simulare anche altri sistemi come, per esempio, un sistema a sei spin. L'esperimento finale sarà svolto, usando coppie di fotoni entangled alla lunghezza d'onda di $1546\ nm$, nei laboratori dell' Istituto di Ottica ed Informazione Quantistica di Vienna, presso il gruppo del professor

Walther.

Durante questi mesi ci si è occupati dell'ottimizzazione di un processo di fabbricazione tramite femtosecond laser macromachining su un substrato di vetro borosilicato che consentisse di ottenere un dispositivo finale in grado di soddisfare le specifiche di progetto (ovvero birifrangenza trascurabile, perdite basse e comparabili tra le varie guide d'onda del dispositivo e completa accordabilità delle fasi).

Un'elevata accordabilità delle fasi può essere ottenuta tramite sfasatori termoottici fabbricati sulla superficie del substrato di vetro dopo la deposizione di un layer metallico. Affinché tali sfasatori siano efficaci occorre che le guide d'onda siano il più possibile prossime alla superficie del vetro. D'altro canto non è stato possibile trovare una finestra di fabbricazione che garantisse basse perdite per basse profondità di fabbricazione. Per questo si è resa necessaria l'introduzione di un nuovo step di fabbricazione: un etching isotropo del campione che disaccoppiasse la profondità di fabbricazione e la distanza delle guide dalla superficie.

Anche gli elettrodi sono stati fabbricati seguendo una nuova ricetta che sostituisce ad un singolo film metallico un doppio strato di oro e cromo. Questi nuovi resistori hanno mostrato tensioni di rottura di quattro volte superiore a quanto osservato con la ricetta precedente e, dopo un processo di annealling, una maggiore stabilità di funzionamento.

La caratterizzazione classica del dispositivo finale ha mostrato come il chip passivo abbia una trasmissione di circa il 60% (corrispondente a perdite di propagazione inferiori a $0.3\ dB/cm$) ed la possibilità di riconfigurare tra 0 e 2π tutte le fasi, come da specifiche.

Contents

List of Figures

List of Tables

Introduction

In the last decades several prototypes of quantum computers have been implemented, but the realization of a ”universal” quantum machine, able to perform any type of computation, is still an unresolved challenge. The state of the art technology allows the creation of application-oriented systems able to deal with circumscribed problems: we speak of analog quantum simulators. They could be seen as today's equivalent of what were the electrical circuits used in the last century to find a non-analytical solution of differential equations otherwise not easily solvable.

There are several examples of quantum simulators that have been realized by exploiting single photons as quantum bits. What makes photons good quantum bits is the fact that they tend not to interact with the environment or with each other and therefore retain their coherent state without losing the information they carry. On the other hand, bulk optical systems, subject to vibration and intrinsically limited in terms of scalability, make the use of integrated optical circuits necessary to improve nowadays performance. Integrated optical chips are much more compact and, being monolithic objects, they are much more resilient to external perturbations. One of the main limitations of these circuits used for applications in quantum optics are the high losses, which lead to extremely long times for the realization of the quantum measurement.

This Thesis dealt with the optimization of the fabrication process and the realization through femtosecond laser macromachining of a low-losses optical circuit that will be used for simulation by entangled photons of the fundamental state and of some excited states of Benzene.

Chapter 1

Quantum Simulation

This first chapter is devoted to the introduction of the fundamental concepts behind quantum simulation with photons in the framework of integrated optics. In particular, Section 1.1 introduces the problem of quantum simulation explaining why a quantum approach allows, in perspective, to outperform classical computers. In Section 1.2 the main notions regarding quantum computing are introduced, highlighting the building blocks for its photonic implementation. We proceed with a brief classification of quantum simulators in Section 1.3. Here a focus is put on photonic quantum simulators, also reporting a few examples from literature. Finally ,Section 1.4 is dedicated to the case of quantum photonic devices realized on the platform of integrated optics.

1.1 Motivation for quantum simulation

In a seminal work about quantum simulation[1], Richard Feynmann wondered whether physics could be properly simulated on a computer. Since in a classical picture physics is described by local differential equations, to simulate reality at that level, one needs to design some kind of numerical algorithm for solving differential equations and "get an approximate view of what physics ought to do". On the other hand, Feynman proceeded, the physical world "is quantum mechanics, and therefore the proper problem is the simulation of quantum physics". Working in a classical picture, to solve these differential equations one may need to discretize the system under observation, introducing an intrinsic uncertainty in the result. The fact that reality is by itself quantized, instead, leads to the idea that in some cases nature is transposable to a finite number of digits, in principle with no approximation. Moreover the kind of computer conceived by Feynman, thank to the phenomenon of state superposition, is such that doubling the size of the problem means doubling the solving time and not, as happens for many classical algorithms, having an exponential growth of the solving time itself. Basically, in that paper, Feynman had already conjectured all the essential characteristics of what nowadays we call quantum computers.

Unfortunately such computers still do not exist. At the moment we don't even know which physical platform could be the best for realizing them. For now, what we can do is thinking how to simulate a quantum system in a simpler way: without making a universal machine, suited for any kind of simulation, but implementing application-oriented "analog" devices requiring less control and easier to conceive.

A quantum simulator is a controllable quantum system used to mimic through a unitary transformation U another quantum system that we cannot directly access. A conceptual scheme of quantum simulation is shown in Figure 1.1. The main steps to implement it are: the preparation of an initial state, the simulation of its evolution obtained by means of the simulator and the measurement of the output simulated state. From the technological point of view, different examples and prototypes have already been made, exploiting a variety of physical systems (such as trapped ions[2, 3], spin-systems[4, 5], superconductive circuits[6] and photons[7, 8]). Quantum simulation promises to be a useful tool to solve problems in various fields, e.g. atomic physics, quantum chemistry, high energy and condensed matter physics[9].

A generic quantum simulation problem could be that of identifying the state

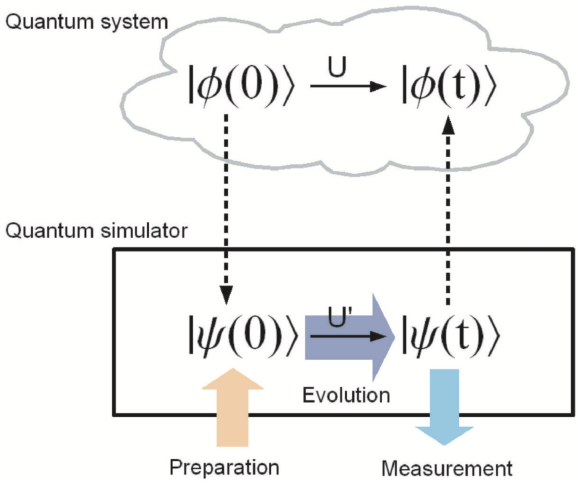

Figure 1.1: *In this Figure (taken from[9]) is illustrated a schematic of a quantum simulation process. There's a map linking the system we are interested in (whose wavefunction is indicated with $|\phi\rangle$) and the quantum system used to simulate it (described by $|\psi\rangle$). The simulation is implemented through U', mimicking the real evolution, U, of $|\phi\rangle$.*

evolution of a system described, at $t = 0$, by $|\phi(0)\rangle$ and by a time independent Hamiltonian H. From the Schrödinger equation we have:

$$i\hbar \frac{d}{dt}|\phi\rangle = H|\phi\rangle \tag{1.1}$$

and so $|\phi(t)\rangle = \exp\{-iHt\}|\phi(0)\rangle$. Using classical tools, the problem can be solved discretizing it. By virtue of state superposition, though, the amount of memory necessary to store the problem on a PC will grow exponentially with the size of the system. For instance, dealing with N spin-1/2 particles we have 2^N allowed configurations, computing the time evolution of such a system requires to deal with $2^N \times 2^N$ matrix elements. If we had $N = 40$ this would correspond to about $4\,TB$; when $N = 80$, $\sim 10^{12}\,TB$ would be needed[9]. This is the so-called exponential-explosion problem[1]. There are classical methods to tackle the problem in a stochastic way (Monte Carlo algorithms) or looking for approximate solutions (Green function method), but they do work well only when applied to "well-behaved systems" and problems related to fermionic or frustrated systems might not belong to this category[9].

A fully quantum approach could circumvent the computational complexity stemming from state superposition by exploiting it, in the first place, to simulate the

system of our interest. On the other hand, nowadays there are quantum computers relying only on few qubits which cannot outperform classical supercomputers. Considering that the number of required qubits scales linearly with the size of the basis set of the problem we're dealing with, only beyond $\sim$150 quantum bits quantum computers would beat any algorithm on a classical supercomputer[10], thanks to the fact that the storing capability of qubits is exponentially larger with respect to classical bits.

1.2 Quantum computing (with photons)

As already mentioned there are many physical systems that could be exploited to build a quantum computer. The goal of this Thesis work is the realization of an *optical* chip for quantum simulation, so in the following we will generally concentrate on the case of photonic quantum simulation. Before doing that, this Section goes through a summing up of the main concepts regarding quantum information to set the formalism in which quantum computations are devised.

1.2.1 Quantum bits

The quantum bit (or qubit) is the basic element for quantum computations. At variance with classical bits, presenting just two mutually exclusive states: either they are 0 or 1, qubits can, because of their quantum nature, represent an infinite set of states. Starting from a two states ($|0\rangle$ and $|1\rangle$) computational basis, the most generic expression for a single quantum bit is:

$$|\psi\rangle = \alpha|0\rangle + \beta|1\rangle \tag{1.2}$$

By virtue of the fact that α and β are complex numbers and that the only restriction on $|\psi\rangle$ is that it is normalized (namely $\langle\psi|\psi\rangle = 1$), an alternative representation for ψ reads:

$$|\psi\rangle = \cos\theta|0\rangle + e^{i\phi}\sin\theta|1\rangle \tag{1.3}$$

with $\theta \in [0, \pi]$ and $\phi \in [0, 2\pi)$. Taking into account that the modulus of ψ is always one and that we have two free parameters given by two angles, the qubit can be graphically represented in the Bloch or Poincaré sphere (Figure 1.2).

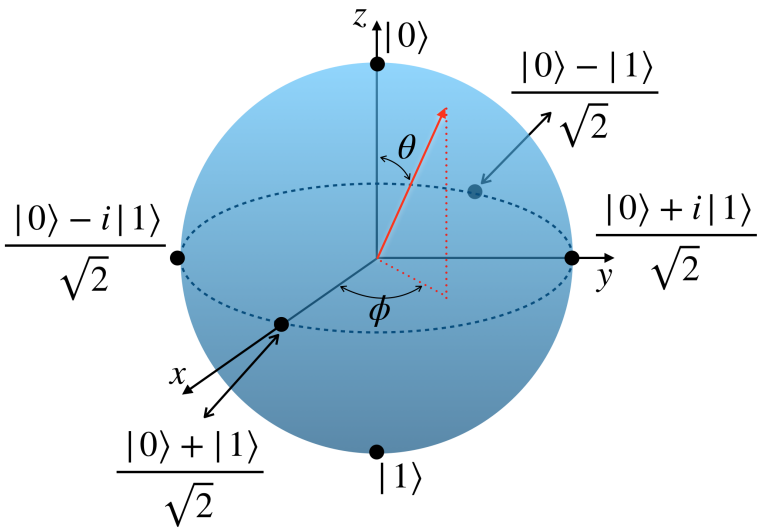

Figure 1.2: *This is the so-called Bloch sphere, a generic qubit is represented on it through the red arrow. In case the basis* $(0, 1)$ *is replaced with the polarization basis (and so, to fix the ideas,* $|0\rangle \to |H\rangle$ *and* $|1\rangle \to |V\rangle$*), it is usually referred to as the Poincaré sphere.*

Talking about photons, information could be encoded exploiting the degrees of freedom of light, i.e. propagation direction, time, momentum and light spatial distribution. In this section the analysis will be circumscribed to:

1. **polarization** encoded qubits. Polarization is the classical equivalent of spin for electromagnetic waves. Being photons ultra-relativistic particles, there are just two independent polarization states for photons: vertical and horizontal polarization or, in another basis, left and right circular polarization. Thus polarization degrees of freedom are suited to produce a binary representation. For example, using horizontal and vertical polarization: $|\mathbf{0}\rangle \equiv |H\rangle \equiv |1\rangle_H \otimes |0\rangle_V$ and $|\mathbf{1}\rangle \equiv |V\rangle \equiv |0\rangle_H \otimes |1\rangle_V$[1]. In this reference frame the most general expression for a qubit becomes:

$$|\psi\rangle = \alpha|H\rangle + \beta|V\rangle \tag{1.4}$$

   Polarization encoding is a *single rail encoding*: the two symbols are encoded in the same spatial mode, at variance with what happens in the so-called *dual rail encoding*.

[1]The symbol $\otimes$ denotes tensorial product. For the sake of brevity it will be omitted in the following of this work, so for example, $|H\rangle \equiv |1\rangle_H \otimes |0\rangle_V \to |1\rangle_H |0\rangle_V$.

2. **dual rail encoding**: in this case, instead of relying on two different polarizations, the two symbols are encoded on different spatial modes:

$$|\psi\rangle = \alpha|1\rangle_a|0\rangle_b + \beta|0\rangle_a|1\rangle_b \tag{1.5}$$

Photons are suited for being quantum bits because they can be produced as single particles, are not bound to a specific site in space (so could be used as information carriers) and have a long coherence time. Furthermore two identical photons are completely indistinguishable and this means that their *wavefunctions* can interfere. This is a completely different kind of interference with respect to the classical electromagnetic interference we would have in the case of classical light. This sort of wavefunction-interference is a fully quantum interference and can be verified, for example, in the so-called Hong Ou Mandel experiment[11], showing that, because of photon bunching, the behavior of a beam splitter on single photons is completely different with respect to the one we would have with classical light.
But probably the most peculiar manifestation of quantum nature of photons takes place through entanglement.

1.2.2 Photon entanglement and Bell's states

First of all, an entangled state is a state pertaining to a system made of more than one particle. Entangled particles have to be fully quantum particles, e.g. two single photons. Being entangled, they will show a very high correlation, not allowed in the framework of classical physics. Such a high correlation derives from the fact that they do share the same state, described by one sole wavefunction, even if they can be arbitrarily far from one another. Actually this nonlocal nature of entanglement has been the source of a great debate about the correctness and roots themselves of quantum mechanics. In any case, apart from this historical discussion, it's proven that, in quantum mechanics, entanglement is real and indeed it has been widely exploited in quantum experiments[12, 13].

From the mathematical point of view, the wavefunction describing an entangled state cannot be factorized in the product of wavefunctions related to just one part of the whole (entangled) system. In other words, given two particles, A and B, if the wavefunction of the whole system, containing both A and B, can be cast as $|\Psi_{AB}\rangle = |\psi_A\rangle|\psi_B\rangle$, we don't have an entangled state.

The simplest and most interesting case is the one regarding two maximally en-

tangled particles, that will be in one of the four Bell states:

$$|\psi^+\rangle = \frac{1}{\sqrt{2}}\left(|0\rangle_A|1\rangle_B + |1\rangle_A|0\rangle_B\right) \tag{1.6a}$$

$$|\psi^-\rangle = \frac{1}{\sqrt{2}}\left(|0\rangle_A|1\rangle_B - |1\rangle_A|0\rangle_B\right) \tag{1.6b}$$

$$|\phi^+\rangle = \frac{1}{\sqrt{2}}\left(|0\rangle_A|0\rangle_B + |1\rangle_A|1\rangle_B\right) \tag{1.6c}$$

$$|\phi^-\rangle = \frac{1}{\sqrt{2}}\left(|0\rangle_A|0\rangle_B - |1\rangle_A|1\rangle_B\right) \tag{1.6d}$$

It is interesting to note that swapping the two photons in 1.6a, 1.6c and 1.6d doesn't modify the wavefunction (which is defined up to global phase terms), whilst in the case of 1.6b it would change the things! This is a matter related to the symmetry of these states; actually $|\psi^+\rangle$, $|\phi^-\rangle$ and $|\phi^-\rangle$ are triplet states (so the total spin of the system is 1), while $|\psi^-\rangle$ is a singlet state (total spin 0).

Apart from the theoretical interest for Bell's states, those reported above are equations of particular interest because very often single photons are generated through spontaneous parametric down conversion (SPDC) by type II phase matching, which is a process producing maximally entangled photons with respect to polarization and mathematically expressed as

$$|\psi\rangle = \frac{1}{\sqrt{2}}\left(|H\rangle_A|V\rangle_B + e^{i\varphi}|V\rangle_A|H\rangle_B\right)$$

According to the phase lag φ between the two terms, one can produce both $|\psi^+\rangle$ and $|\psi^-\rangle$, or even "something in the middle", in the basis of vertical and horizontal polarization.

1.2.3 Quantum gates

In the circuit model for quantum computing, quantum logic gates are basic quantum circuits operating on a few qubits. They are the building blocks of a more complex circuit dealing with an arbitrary number of qubits, just like classical logic gates are the basis components of ordinary digital circuits.

To cope with laws of quantum mechanics the whole quantum circuit needs to be describable as a unitary transformation, i.e. a matrix U such that $U^\dagger U = UU^\dagger = 1$. This guarantees that as we start with a normalized initial state we will end up with another normalized wavefunction. In the circuit model the overall unitary transformation operating on N qubits is decomposed in other, "smaller", unitary

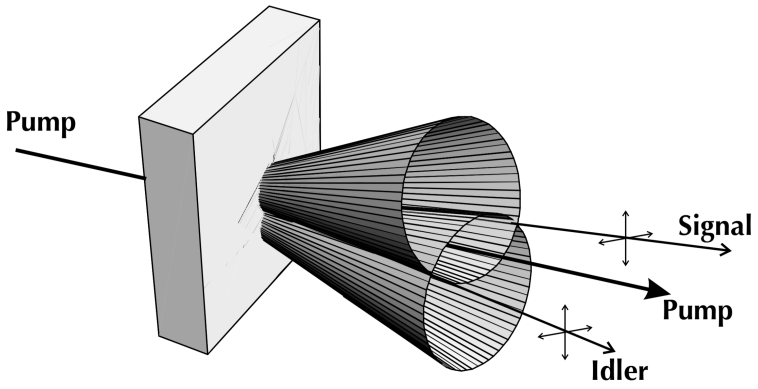

Figure 1.3: *A sketch of spontaneous parametric down conversion in the case of the so-called Type II phase matching. The signal and idler photons have orthogonal polarizations. Photons along the two intercepting cones are collected to obtain entanglement. The image is adapted from[14].*

transformations operating on one or two qubits. All these transformations (and so all quantum gates) are reversible.

When dealing with this circuital model qubits are typically represented as vectors, for the single qubit:

$$|\psi\rangle = \alpha|0\rangle + \beta|1\rangle = \begin{pmatrix} \alpha \\ \beta \end{pmatrix}$$

For a two-qubits gate input and output are in the form:

$$|\psi\rangle = \alpha|0\rangle|0\rangle + \beta|0\rangle|1\rangle + \gamma|1\rangle|0\rangle + \delta|1\rangle|1\rangle = \begin{pmatrix} \alpha \\ \beta \\ \gamma \\ \delta \end{pmatrix}$$

It was shown [5] that starting from a set of some one-qubit gates and at least one two-qubit gate any set of universal gates can be created. For this reason in the following we will report just a few examples of one-qubit gates and two two-qubits gates.

Single qubit gates

In the case of single qubit gates the unitary transformation U could be any rotation of the Bloch sphere. Possible gates are:

- **Hadamard gate**, creates a state superposition starting from a pure state. It is defined through:

$$H = \frac{1}{\sqrt{2}} \begin{pmatrix} 1 & 1 \\ 1 & -1 \end{pmatrix} \tag{1.7}$$

- **Pauli rotations**, i.e. any rotation defined through a Pauli matrix (see Figure 1.4), for example the quantum equivalent of a classical NOT gate, the Q-NOT:

$$X = \sigma_X = \begin{pmatrix} 0 & 1 \\ 1 & 0 \end{pmatrix} \tag{1.8}$$

  the π-shift:

$$Z = \sigma_Z = \begin{pmatrix} 1 & 0 \\ 0 & -1 \end{pmatrix} \tag{1.9}$$

  or the Y gate:

$$Y = \sigma_Y = \begin{pmatrix} 0 & -i \\ i & 0 \end{pmatrix} \tag{1.10}$$

Two-qubits gates

The simplest examples of two-qubits gates are the controlled version of the Q-NOT or of the π-shift, in which the operation implemented by the corresponding single qubit gate is performed on the second qubit only if the first one is in state $|1\rangle$:

- **CX** or **C-NOT** gate, flipping the second qubit, when operating:

$$CX = \begin{pmatrix} 1 & 0 & 0 & 0 \\ 0 & 1 & 0 & 0 \\ 0 & 0 & 0 & 1 \\ 0 & 0 & 1 & 0 \end{pmatrix} \tag{1.11}$$

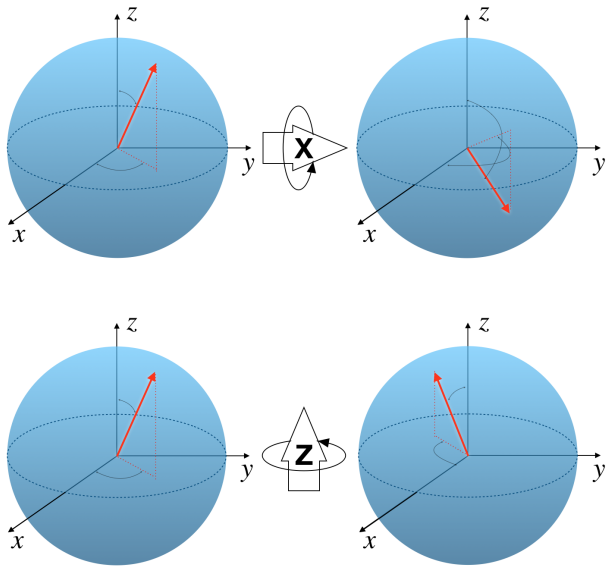

Figure 1.4: *The images schematize the effect of single qubit gates on a generic qubit. In the upper panel the result of a Q-NOT: the arrow representing the qubit (i.e. the red arrow) is rotated of π around the x axis. In the lower one: the Z-gate performs an analogous rotation about the z axis.*

- **CZ** gate, introducing a phase shift in the second qubit, when the first is in state $|1\rangle$:

$$CZ = \begin{pmatrix} 1 & 0 & 0 & 0 \\ 0 & 1 & 0 & 0 \\ 0 & 0 & 1 & 0 \\ 0 & 0 & 0 & -1 \end{pmatrix} \tag{1.12}$$

Another example of two-qubit gate is the **SWAP** gate, swapping two qubits. With respect to the basis $|00\rangle$, $|01\rangle$, $|10\rangle$, $|11\rangle$ it reads:

$$SWAP = \begin{pmatrix} 1 & 0 & 0 & 0 \\ 0 & 0 & 1 & 0 \\ 0 & 1 & 0 & 0 \\ 0 & 0 & 0 & 1 \end{pmatrix} \tag{1.13}$$

1.3 Quantum simulators

Quantum simulators, regardless of the technological platform through which they are implemented, can be subdivided into two main categories: those whose goal is the simulation of a collective property of the system (e.g. a phase transition), for which a relatively low level of control of quantum properties is sufficient; and those that provide informations at the mesoscopic and molecular level of the system, for these a precise local control and addressability is needed[10].

A further classification divides quantum simulators in digital quantum simulators (DQS) and analog quantum simulators (AQS):

- **Digital quantum simulators (DQS)**

  In this case the unitary transformation U which imitates the real system is implemented using a sequence of single and two-qubit gates. It could be demonstrated[15] that any possible Hamiltonian can be simulated as a series of unitary operations like the ones performed by those gates. This is why DQS are said to be universal: they could reproduce any Hamiltonian. The precision of the computation increases with the number of gates, so the simulation can be made as precise as desired, paying in circuital complexity.

  However there exist Hamiltonians that cannot be efficiently simulated: in some cases the number of ports scales exponentially (and not polinomially)

with the complexity of the system, so the implementation of DQS isn't always straightforward. Concerning the initial state preparation there is not a general rule[9]. For what regards the final state measure, instead, quantum state tomography (QST) is needed to get a full characterization of $|\psi(t)\rangle$, unless one wants just an estimation of certain physical quantities, in which case a simpler post processing could suffice[16].

- **Anolog quantum simulators (AQS)**

  The universality is a strong point in favor of DQS, but for the current state of technology AQS are the most feasible solution. At variance with DQS, analog quantum simulators are not at all universal, but rather "application-oriented".

  AQS are typically used to simulate many-body physics, so the key-point to realize them is finding a direct map between the Hamiltonian of the system to be simulated and the one of the simulator. This is why an AQS cannot be used for any other application but the one it was conceived for. Finding the map linking the simulator and the real system is not always straightforward, but in general, once it has been set, initial state preparation and the measurement are so, given the vicinity between the two systems.

  The accuracy of the simulation depends on how well the real system is reproduced. In analog quantum simulators there's a higher tolerance to errors with respect to DQS: in the "digital case" an error in a gate might completely change the implemented unitary transformation, in an analog quantum circuit an error would just reduce the accuracy of the final result, without necessarily changing the qualitative answer provided by the device[9].

  Finally, the specificity of the simulator, is sometimes compensated by the possibility of making tunable devices, probing the behavior of the wavefunction, instead of the Hamiltonian, in various conditions[7].

Figure 1.5 shows a comparison between two schematics of an analog and a digital quantum simulator.

Once that a proper platform for quantum simulations has been engineered one needs to implement an efficient algorithm to run on it and, also, an efficient way for extracting useful information from the quantum computation.

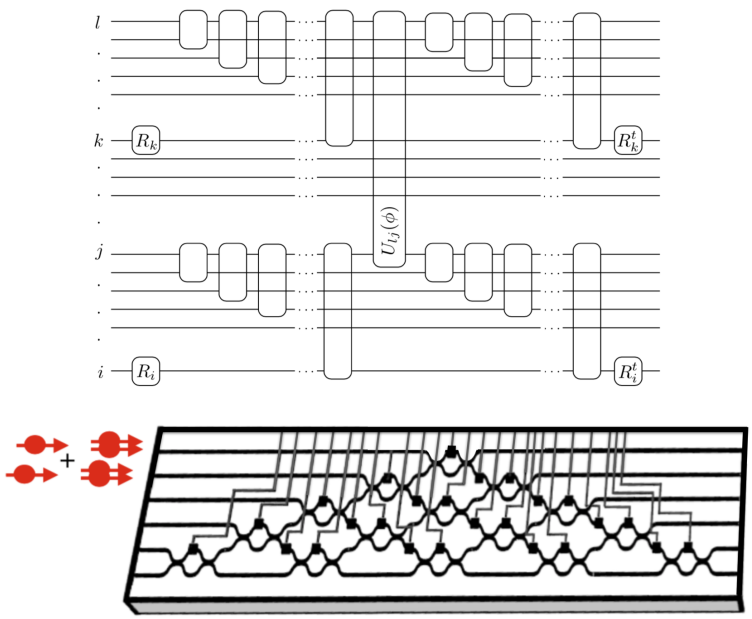

Figure 1.5: *These are two schematics representing quantum simulators. In the upper panel (taken from[17]) is shown a circuit performing a digital quantum simulation of a minimal Anti-de-Sitter/Conformal Field Theory model to be implemented on a superconducting circuit[17]. All gates are either single-qubit gates, or two-qubit gates. In the bottom panel, from[18], the schematic of the AQS used to simulate through photons, using squeezed states of light, the vibrational dynamics of some four-atoms molecules. All qubits enter a single "black box" which simulates the evolution in time of the initial state and that cannot be trivially decomposed into single- and two-qubit ports.*

1.3.1 Algorithms for quantum chemistry simulations

In this section, as an example for protocols that could be followed on quantum simulators, some quantum algorithms aiming at finding the spectrum of a known Hamiltonian will be presented. In general the goal of these algorithms is always the analysis of quantum many body systems, using a quantum computer which, in the end, is nothing but a quantum many body system itself.

Finding eigenvalues and eigenvectors of a known Hamiltonian

The first algorithm we are going through is named Quantum phase estimation (QPE). It is a very relevant quantum protocol: a good variety of quantum proto-

cols, not only used in quantum simulation, rely or take inspiration from it. For this reason it will be dealt with in detail.

First of all let us go back to the one dimensional Schrödinger equation, written in 1.1, and suppose that the initial state is $\psi_0(x)$. As time goes on, the system will be described by:

$$\psi(x,t) = U(t)\psi_0(x) \tag{1.14}$$

being $U(t)$ the evolution operator at time t associated to the hamiltonian H:

$$U(t) = e^{-iHt/\hbar} \tag{1.15}$$

Concerning the eigenstates of H, we have: $H\phi_k(x) = E_k\phi_k(x)$ (and thus, for U: $U\phi_k(x) = e^{-iE_kt/\hbar}\phi_k(x)$). Therefore $\psi_0(x)$ can be recast as

$$\psi_0(x) = \sum_k c_k\phi_k(x) \tag{1.16}$$

and calling $\omega_k = E_k/\hbar$

$$\psi(x,t) = \sum_k c_k e^{-i\omega_k t/\hbar}\phi_k(x) \tag{1.17}$$

From this last expression it's clear that the phase accumulated, as time passes, contains the information necessary to find the eigenvalues. Moreover it's easy to see, even without going through the calculations, that the Fourier transform $\widetilde{\psi}(x_0,\omega) = \mathscr{F}\{\psi(x_0,t)\}$ is going to exhibit peaks at the various ω_k [2], allowing one to extract the eigenvalues of the problem. Regarding the eigenfunctions, they can be retrieved by computing several times the Fourier transform at different x_0 and reconstructing the various $\phi_k(x)$ from the relative amplitudes of the peaks corresponding to the frequencies ω_k[19].

As the system complexity increases, though, the described procedure cannot be efficiently implemented on a classical computer, since the problem size would quickly explode. Let's suppose, instead, that we have at our disposition a quantum computer having a finite number of quantum bits. If one is interested in simulating the problem for $x \in [-L, L]$, exploiting n qubits to discretize the system with

[2] Actually a peak at a certain ω_k will be resolved through this approach provided that we let the system evolve for a time $\bar{t} > \frac{1}{\omega_k}$.

respect to space, we get 2^n nodes along the x axis, separated by $\Delta x = \frac{2L}{2^n-1}$. The state of the system could be encoded as:

$$|\psi\rangle = \sum_{i=0}^{2^n-1} \psi(i)|i\rangle \tag{1.18}$$

where $\psi(i) = \psi(-L + i\Delta x)$ represents the amplitude attributed to the i$^{\text{th}}$ element of the used basis [3]. So exploiting only n qubits we can store 2^n complex numbers: the quantum computer is itself a many body quantum system relying since the beginning on state superposition.

The time evolution in an interval Δt is described by the operator $U(\Delta t)$:

$$U(\Delta t) = e^{-iH\Delta t/\hbar} \tag{1.19}$$

and can be simulated on a quantum platform. The quantum circuit to be used to implement the quantum algorithm is shown in Figure 1.6. Its execution provides:

$$|\Psi\rangle = \frac{1}{\sqrt{2^l}} \sum_{j=0}^{2^l-1} |j\rangle \underbrace{U^j|\psi_0\rangle}_{\psi(j\Delta t)} \tag{1.20}$$

where l is the number of bits of an auxiliary qubits register defining the accuracy of the measurement. Recalling equation 1.16 and the effect of operator U, formula 1.20 can be rewritten as follows:

$$|\Psi\rangle = \frac{1}{\sqrt{2^l}} \sum_{j=0}^{2^l-1} |j\rangle \sum_{k=0}^{2^n-1} c_k e^{-i\omega_k j\Delta t}|\phi_k\rangle \tag{1.21}$$

that apart from the addition of the contribution belonging to the auxiliary qubit register (that is an auxiliary set of qubits), is nothing but a different expression for 1.17: it could be shown that its quantum Fourier transform with respect to the $|j\rangle$ is peaked at the various ω_k, permitting the reconstruction of the Hamiltonian spectrum[19].

It's worth pointing out that with the procedure described above only those eigenvectors on which the initial prepared state has a non-zero projection can be found. Furthermore, even if from the standing point of the required number of bits, the quantum approach is for sure convenient on the classical one, this algorithm doesn't always solve the problem in polynomial time. As a matter of fact the

[3] Having just two qubits, i would go from **0** to **3** and $|\mathbf{0}\rangle = |00\rangle$; $|\mathbf{1}\rangle = |01\rangle$; $|\mathbf{2}\rangle = |10\rangle$; $|\mathbf{3}\rangle = |11\rangle$.

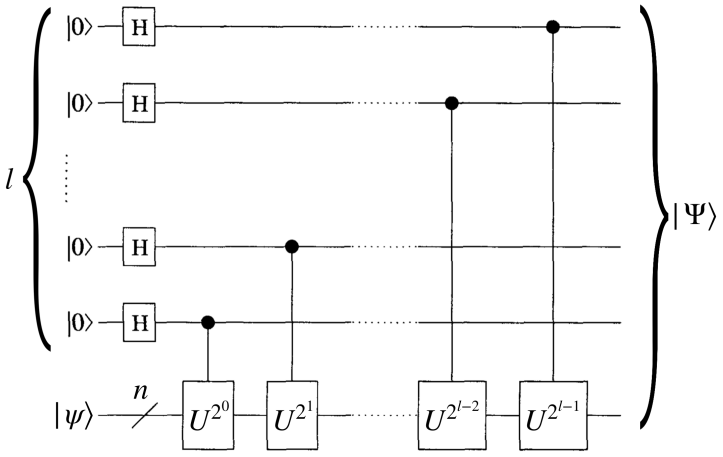

Figure 1.6: *This figure shows a quantum circuit implementing a phase estimation algorithm, indeed to retrieve the eigenvalues of the system we need to evaluate what phase is accumulated due to the evolution operator U. l quantum bits are used for a control register determining the accuracy of the estimation: the uncertainty ϵ on the measured ω_k is $\epsilon \propto \frac{1}{2^{l+1}}$[19]. n qubits, instead, are dedicated to encode the initial state. Adapted from[19].*

algorithm has to be run many times and, at each run, you find a single component (namely, in terms of eigenvalue, a single ω_k) with probability $|c_k|^2$: we have an actual advantage with respect to a classical computation if eigenvectors and eigenvalues are found after a polynomial number of trials, as usually happens at least for the fundamental state[20].

Quantum variational eigensolver

Quantum phase estimation algorithms offer an exponential speed up over classical method but suffer from a main drawback: the precision level of the estimation is limited not only by the number of qubits (which is mainly a technological limitation), but also by the naturally finite coherence time of the quantum register. Basically the quantum computer must remain coherent for the time of application of all the unitary operations implemented by the circuit. Such time scales like $O(1/p)$, where p is the required bit-precision on the calculation. For this reason an approach like the one proposed by Peruzzo *et al.* in 2013[21] is extremely helpful.

This algorithm relies on a quantum-variational eigensolver, whose conceptual

scheme is shown in Figure 1.7

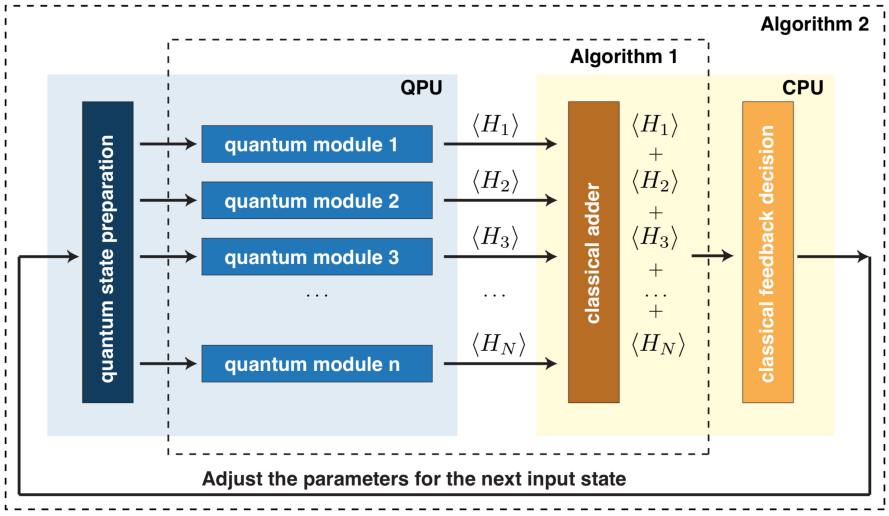

Figure 1.7: *Conceptual schematic (from[21]) of the algorithms followed to implement a Quantum variational eigensolver. In the case of "Algorithm 1" a trial state is fed to a set of quantum modules, each implementing a portion of the kind* $\sum_{ij\alpha\beta} h^{ij}_{\alpha\beta}\sigma^i_\alpha\sigma^j_\beta$ *of the Hamiltonian and providing the expectation value of that portion* $\langle H_i \rangle$*. These contributions are summed to get the expectation value of the original* H*. "Algorithm 2", instead, prepares iteratively the trial states to be fed. The idea is that an initial guess is fed to the first algorithm at the initial iteration. Algorithm 1 provides the energy corresponding to that initial guess and the guess itself is adjusted to minimize the energy by Algorithm 2.*

The fundamental idea is that any Hamiltonian H may be recast as:

$$H = \sum_{i\alpha} h^i_\alpha \sigma^i_\alpha + \sum_{ij\alpha\beta} h^{ij}_{\alpha\beta}\sigma^i_\alpha\sigma^j_\beta + \ldots \tag{1.22}$$

for real h, where α indicates a Pauli operator (e.g. $\alpha = x$) and Roman indices identify the subspace where the Pauli operator acts. In other words, a complex Hamiltonian can be rewritten as a sort of expansion of the combination of Pauli operators.

A wide variety of Hamiltonians can be decomposed in a number of terms which is polynomial in the size of the system. By virtue of linearity the expectation value of H reads:

$$\langle H \rangle = \sum_{i\alpha} h^i_\alpha \langle \sigma^i_\alpha \rangle + \sum_{ij\alpha\beta} h^{ij}_{\alpha\beta}\langle \sigma^i_\alpha\sigma^j_\beta \rangle + \ldots \tag{1.23}$$

Therefore to evaluate the expectation value of H we no longer need to solve at once a complex problem, but we can think of solving one after the other many, simpler problems, represented by the various combinations of σ. The expectation value of a tensor product of an arbitrary large number of Pauli operators is computable efficiently on a quantum platform[16]. Doing so, to obtain an estimate with precision p with the approach described above, the number of repetitions (needed for the measure on the single tensor product of Pauli operators) scales as $O(|h|^2/p^2)$. Thus the total cost of computing the expectation value passes from $O(1/p)$ (for the phase estimation) to $O(|h_{max}|^2 M/p^2)$ where M is the number of terms in the decomposed Hamiltonian. But since the coherence time on a single measurement of this kind scales like $O(1)$, coherence time requirements on the whole process are dramatically reduced (at the price of increasing polynomially the number of repetitions with respect to QPE, but still having an exponential improvement over the classical case). So far I dealt with what is called "Algorithm 1" in Figure 1.7. This procedure can be successfully implemented to find eigenvalues if and only if eigenfunctions are known. "Algorithm 2", instead, allows to find variationally the way to prepare the right eigenfunction for the fundamental state, recalling that such eigenfunction is the one minimizing the quantity

$$\frac{\langle\psi|H|\psi\rangle}{\langle\psi|\psi\rangle} \tag{1.24}$$

In principle, working with $|H-\lambda|^2$, scanning for many values of λ, also excited states could be estimated, relying on the folded spectrum method[22]. Nowadays only the problem of fundamental state was tackled. Obviously not any quantum state can be prepared with a polynomial number of operations. These algorithms were experimentally verified[21], showing the validity of this approach to solve eigenvalue problems with quantum hardware.

The WAVES protocol, a hybrid approach

Another approach for calculating the Hamiltonian spectrum is combining variational methods and phase estimation. This solution was recently proposed by Santagati *et al.*[23] and is implemented through a protocol called witness-assisted variational eigenspectra solver (WAVES). The main steps of the protocol are: (i) an ansatz-based variational search for the ground state; (ii) a witness-assisted variational search for excited states, starting with an initial guess obtained from the ground-state; and (iii) application of the iterative phase estimation algorithm (IPEA,

conceptually not dissimilar to QPE) for the accurate energy estimate of the eigenstates found.

From the practical point of view we start with a combined state $|+\rangle_C|\Psi\rangle_T$ where the first term correspond to a single qubit used as control variable (C), while the second is a generic wavefunction represented on a set of qubits. This second ket is the target (T) of the computation. Such combined state evolves through a controlled unitary $C-U$, where U stands for the time evolution operator. The emerging control qubit is then analyzed through quantum state tomography in order to estimate the von Neumann entropy of the state as $\mathcal{S}(\rho_T) = \mathcal{S}(\rho_C)$ (it is a sort of quantum analog of statistical entropy and attains the same value for the control and the target part of the wavefunction) . Entropy acts as an eigenstate witness: if it is zero, then $|\Psi\rangle$ is an eigenstate. From the off-diagonal terms of the control qubit's density matrix, one can also estimate the energy $\mathcal{E}$ and so construct the following objective function:

$$\mathcal{F}_{obj} = \mathcal{E} + T\mathcal{S}$$

where now T represents the absolute temperature. The local minima of $\mathcal{F}_{obj}$ (in the high T approximation) correspond to eigenstates of the problem. From the conceptual point of view, F_{obj} is similar to a free energy.

With reference to Figure 1.8,

1. E_{p_i} is a system dependent perturbation,
2. $|\Phi\rangle_T$ is an initial reference state modified from one iteration to the other to obtain the various trial states,
3. $A(\vec{\theta}_{e_i})$ represents a transformation preparing trial states via an ansatz. $\vec{\theta}_{e_i}$ is the control parameter of this transformation: $|\Psi\rangle_T = A(\vec{\theta}_{e_i})|\Phi\rangle$.

The algorithm is devised as follows:

1. Start the first iteration keeping $E_{p_i} = I$, identity matrix, and variationally search $\vec{\theta}$ that minimizes $\mathcal{F}_{obj}$, obtaining the ground state.
2. Construct a unitary matrix $E_{p_i}A(\vec{\theta}_{e_i})$, with $\vec{\theta}_{e_i}$ the adjustable parameter to minimize $\mathcal{F}_{obj}$.
3. Once that the eigenstate is known, perform the IPEA, which further projects each state onto the closest eigenstate and refines the energy estimate.

The WAVES protocol as been experimentally validated on a two-qubits silicon quantum photonic processor, and allowed the estimation for ground- and excited-states energies with a precision in the order of $10^{-9}\ eV$ for the states of an already known Hamiltonian.

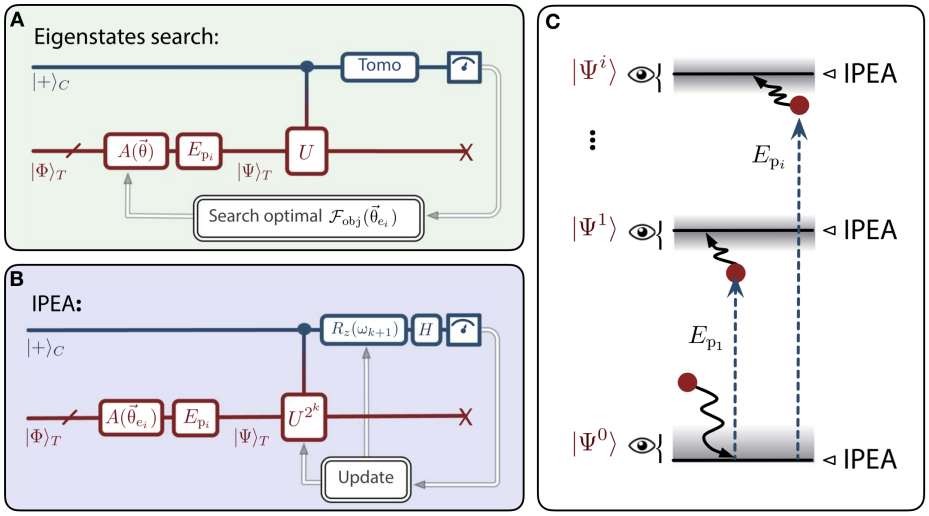

Figure 1.8: *These images, taken from[23], show the quantum circuits used to realize the WAVES protocol (**A** and **B**) and a schematic of the procedure (**C**): through the eigenstate search one finds the wavefunction and a rough estimation of the corresponding eigenvalue, which is then refined thank to the IPEA. Notice that the two circuits basically share the same structure.*

1.3.2 Implementation of photonic quantum simulators

Having reviewed a bunch of possible algorithms for quantum simulation, we now move to an overview of some experimental apparatus - namely, the quantum hardware - used to realize photonic quantum simulations. We will concentrate on the case of photonic-based simulators.

Calculation of the energy levels of a simple molecule

A seminal work in the field of quantum simulation is the paper by Lanyon *et al.*[24] that in 2010 got a 20-bit precision energy calculation of the hydrogen molecule spectrum. The procedure adopted relied on the already mentioned IPEA method.

The molecule was simulated using two entangled photons (C - control and R - register) going through an optical system like the one in Figure 1.9. At each operation the IPEA requires two qubits and the measure is to be repeated several times. At each step a different power of U, obtained changing the configuration of waveplates and polarizers, is implemented. Apart from this iteration process, the approach followed is the same described in the former section.

This was a first prove of principle both for the possibility of realizing quantum simulations and for the validity of the photonic platform. The authors highlighted that the main challenge to scale the solution to systems more complex and bigger than the hydrogen molecule lays in controlling more qubits and achieving longer coherence times.

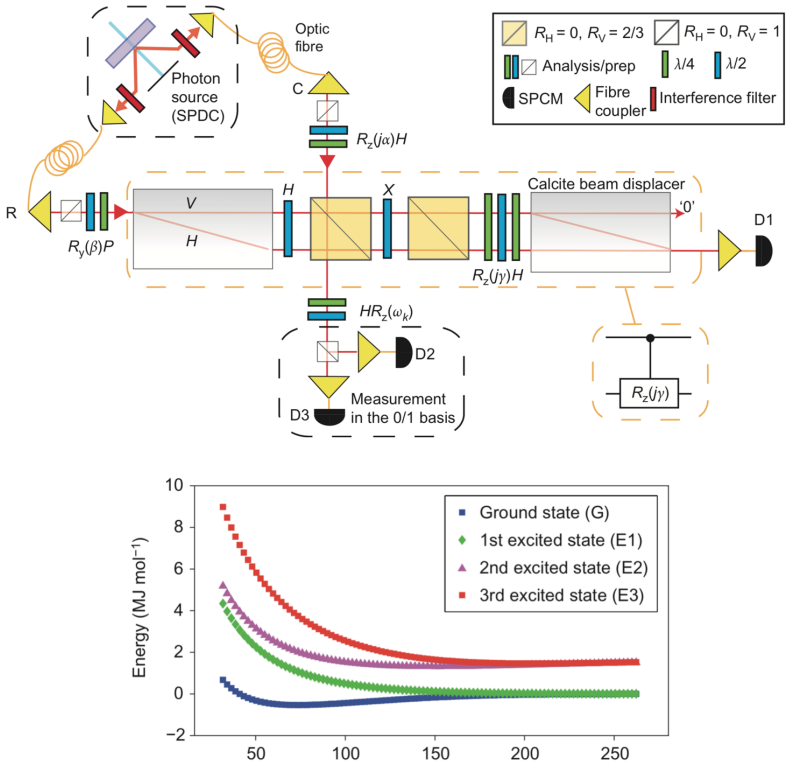

Figure 1.9: *In the upper panel the optical system used to mimic the hydrogen molecule is shown. Results are presented in the other panel: the ground and some of the excited states of the molecule were reconstructed through phase estimation algorithm. Taken from[24].*

Quantum simulation of a parametric wavefunction

There are cases in which a slightly different approach can be pursued to simulate a quantum system. Instead of studying the energy levels starting from the Hamiltonian, assuming that the wavefunctions are known, one could directly simulate the eigenstates and see how they behave under different conditions, for instance to infer the presence of a phase transition.

This idea was implemented by Xiao-song Ma *et al.*[7] to mimic on a photonic platform a frustrated systems consisting of four spin dipoles arranged in a rectangular shape (see Figure 1.10). The Hamiltonian of such a system, considering only interactions between the nearest neighbors, can be modeled as $H = J_1\mathbf{S}_1\mathbf{S}_3 + J_1\mathbf{S}_2\mathbf{S}_4 + J_2\mathbf{S}_1\mathbf{S}_2 + J_2\mathbf{S}_3\mathbf{S}_4$ where $\mathbf{S}_i$ is the Pauli spin operator for spin i. The important point is that this expression depends on two parameters: J_1 and J_2 related, ultimately, to the coupling between the various spin dipoles, i.e. to the geometrical length of the rectangle edges. Thus, since there exists an analytical solution for H, the wavefunction is parametrized itself and its expression is connected with J_1 and J_2. The experiment consisted in simulating, using single photons, the spin wavefunction to estimate directly the ground state energies for different values of J_1 and J_2. From the practical point of view this is achieved using the optical system depicted in the image: femtosecond laser pulses impinge onto two BBO crystals generating two pairs of entangled photons (1-2 and 3-4) whose spectral and spatial distinguishability is purified through other optical elements. Two of these photons interact in the Tunable Directional Coupler (TDC) allowing the exploration of all possible values for $\kappa = J_1/J_2$ so that, when detection takes place, the photon state corresponds to the wanted spin state is analyzed.

The core element to perform the experiment is a Tunable Directional Coupler, used to tune continuously some parameters of the quantum hardware simulating the system: this element makes the used optical system an archetype for analog quantum simulations. The quantum measurements performed on it permitted to get relevant insights into entanglement dynamics among individual particles and the direct extraction of ground-state energies of the system.

Study of the dynamic of a quantum system

In 2018 another successful example of optical quantum simulation using single photons was produced by Sparrow *et al*. The paper[18] shows how it has been possible to simulate the time evolution of the vibrational modes for different four-

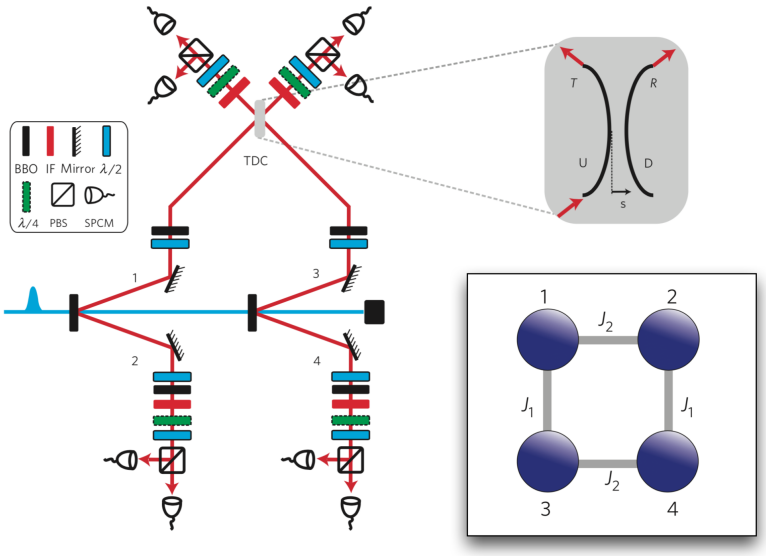

Figure 1.10: *The spin system is shown in the insert: dipoles are arranged in a tetramer. This geometry leads to a frustrated system. The optical system implements, as described in the text, the wanted state. The simulated wavefunction depends on the configuration of the TDC which can mimic the effect of all possible values of the ratio* $\kappa = J_1/J_2$*. The Figure is taken from[7]*

atom molecules, making use of the analogies between vibrational modes in molecules and optical modes in waveguides and between single photons and quantized vibrational excitations. The dynamic was reconstructed from the number of photons at each output port (the "statistic pattern"), corresponding to certain vibrational states. In this case the technological platform was an optical analog quantum simulator, the one shown in Figure 1.5 (bottom panel) controlled via an active feedback through which external electronics adjusted the tunable parameters of the circuit, according to the measured states. The system was a reconfigurable *silica-on-silicon* photonic circuit whose size (in terms of number of waveguides and tunable phases) shows how flexible and scalable the optical approach can get when pursued on an integrated platform.

Scalability is probably one of the greatest advantages of using **integrated photonic circuits**, rather than typical bulky optical systems. This is a crucial feature to reach the aforementioned target: a quantum system relying on a sufficient num-

ber of quantum bits, capable of outperforming classical machines.

The next section will deal with integrated optical circuits for quantum optics application.

1.4 Integrated quantum optics

Traditional optical systems, exploiting bulk optical components, can be used to realize optical circuits implementing quantum simulators. However, these systems have typically a big footprint and are particularly exposed to external perturbations and vibrations. To perform experiments with single photons, phase stability requirements are very demanding and hardly achievable using bulk optics. Integrated optical devices, instead, beside showing dimensions in the order of just a few centimeters, are much more resilient against perturbations and vibrations and for this reason more reliable and indicated for this kind of applications. In particular they could guarantee a better coherence with respect to other approaches. Moreover, as already touched above, they allow to obtain a much higher scalability, necessary for the implementation of a complex quantum hardware.

Now, getting one step back, in order to devise a quantum computer we need to implement a set of single-qubit gates and at least one two-qubit gate. The realization of a two-qubit gate operating on photonics quantum bits has been considered challenging in the past years[25]. This because photon-photon interaction is very weak (practically they don't interact with each other), thus engineering two-qubit gate operations or preparing multi-photon entanglement starting from single photons as input is not easy[10]. This is why the 2001 paper presenting the so-called KLM protocol[4] is considered a cornerstone for quantum computing with linear optics. In this paper, indeed, it is proved that efficient quantum computation is possible using only beam splitters, phase shifters, single photon sources and photo-detectors[25] exploiting one-qubit gates only with the aid of some ancillary qubits, with no need for non-linear optical components. In practice non linearity is achieved (in a probabilistic way) through a post selection process, making integrated optics a promising platform for implementing quantum computations.

If the KLM protocol is a cornerstone for quantum computing with optics in general, coming back to the specific case of integrated quantum photonics, an important turning point is due to Politi et al.[26] who in 2008 observed quantum interference between two single photons in a directional coupler. Since then photonic

[4]Named after the authors of the paper in object: Knill, Laflamme, and Milburn.

quantum circuits have been implemented on various technologies, e.g. on the platform of *Silicon photonics*, using the *Silica-on-silicon* technology and *Femtosecond Laser Micromachinig* (FLM). This last approach is one of the best suited for applications in quantum optics, since it allows a cheap and fast prototyping of devices that typically are supposed to be produced in low volumes. The technique will be described in detail in Chapter 2, however an overview of relevant results achieved using FLM is shown hereafter in Figure 1.11 which clarifies how promising the field looks.

At the state of the art, the most critical issues that we need to overcome, to hope that photonic quantum computing will actually outperform classical supercomputers, are[10]: the controlled generation of single photons (maybe exploiting quantum dots or nitrogen-vacancy centres in diamond), the reduction of coupling losses and the implementation efficient superconducting detection units capable of distinguishing the number of detected photons, to enhance the experimental fidelities. An illustration of a fully integrated quantum photonic simulator is depicted in Figure 1.12.

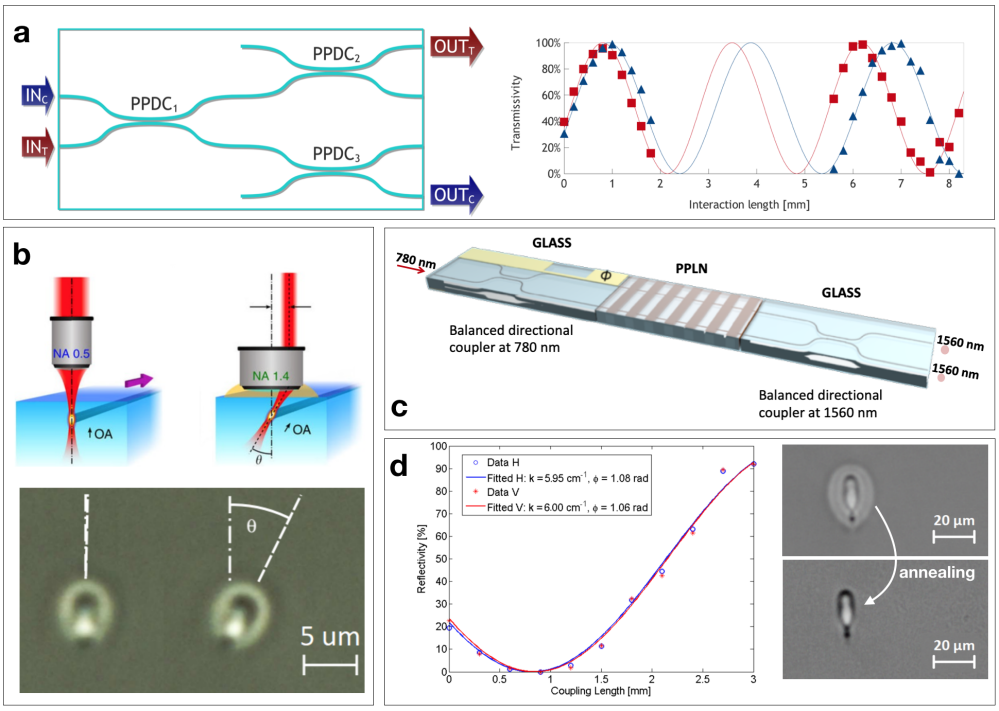

Figure 1.11: *Relevant achievements in integrated quantum optics obtained exploiting the FLM.* ***a****: Crespi et al. demonstrated in integrated optics a C-NOT gate for polarization encoded qubits[27]. Since the gate is realized using partially polarizing directional coupler, the output isn't fully polarization insensitive;* ***b*** *Corrielli et al. fabricated integrated waveplates exploiting the waveguides birefringence by tilting the optical axis[28]. More recently the same group proposed Integrated photon-pair sources[29] exploiting non-linear effects at the chip level and demonstrated polarization insensitive optical circuits[30], in panel* ***c*** *and* ***d*** *respectively. Images* ***a****-****d*** *are taken from:[31–34].*

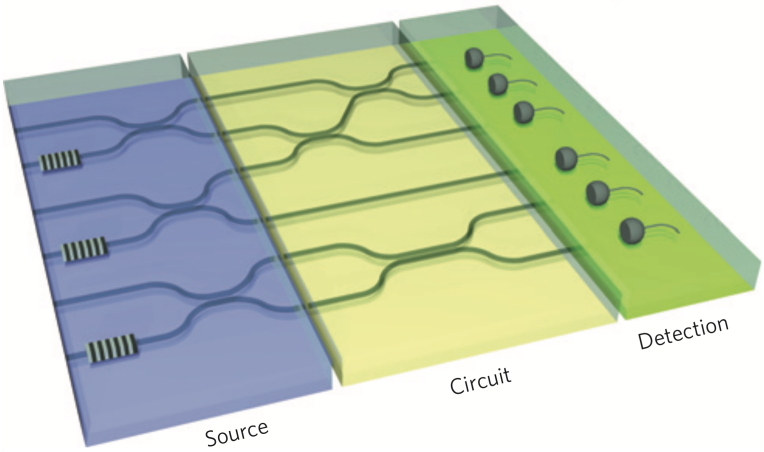

Figure 1.12: *In the picture, taken from[10], is shown the idealized schematic of a photonic quantum simulator where both photon sources and detectors are on-chip. In principle each block could be realized on a different platform, provided that there's a good coupling (and so acceptable losses) between different blocks.*

Chapter 2

Femtosecond Laser Micromachining

The one of interaction between matter and ultrashort pulses is an extremely vast field. In particular, this kind of interaction may be used both to study in a fully reversible way the structure and the dynamics of a material or to induce permanent modification and engineer structures at the dimensional scale of the beam focus. The latter case is the one of interest for this Thesis: Femtosecond Laser Micromachining (FLM) is actually a technique that uses in a controlled way the changes induced by short pulses in matter.

In this chapter the FLM technique is briefly presented: section 2.1 shows the peculiar features of FLM, those characteristics that make it different with respect to other direct inscription methods. Section 2.2 deals with the physics behind the technique, whilst in section 2.3 the dependence of the results obtained through FLM on relevant writing parameters is reported. Section 2.4 presents an overview on those integrated optical devices that are the ”building blocks” for more complex optical circuits.

2.1 Femtosecond Laser Micromachining, an overview

In the last couple of decades, Femtosecond Laser Micromachining proved itself capable of realizing optical devices in dielectric materials with some advantages with respect to other, more traditional, approaches (e.g. lithographic techniques, typically used in telecommunication and electronics industry).

Through FLM a modification in the sample is achieved thank to non linear optical effects taking place where the laser is focused. Introducing a relative motion between the laser beam and the chip itself, complex structures can be created in the substrate. Since laser pulses can be focused at different depths beneath the surface of the dielectric, tridimensional devices can easily be obtained. Moreover, while "low" energy pulses lead to a smooth change in the refractive index, compatible with the fabrication of integrated photonic devices, higher energy pulses could induce birefringent modification (typically periodic and perpendicular to the laser polarization), not ideal for optical circuits, but characterized by a higher selectivity to hydrofluoric acid exposure with respect to the non irradiated material. This permits to create microchannels in glass or crystals, useful for microfluidic application[35]. FLM can also be used to microstructure dieletric samples ablating the radiated material. So FLM is not necessarily a photonic-oriented-only technology, but is actually very versatile.

For the specific case of optical devices, the evident benefits of FLM with respect to lithographic techniques are:

- **low costs and time saving**, since FLM is mask-less and allows for a rapid change in the geometry of the chip (one just needs to change the irradiated path);
- **flexibility**, as many transparent substrates (either in passive or active) can be effectively modified with FLM;
- **tridimensinality**, as already mentioned, focusing the beam *in* the material and displacing the sample along three axes with respect to the beam, modifications can be obtained not only at the surface and complex 3D optical circuits can be realized.

Another relevant advantage of this technique consists in the possibility to obtain very low birifringent waveguides (thank to an annealing process)[36], extremely useful for applications in quantum optics and not easily possible with lithographic waveguides that typically show a higher birefringence. Moreover, for what regards

quantum experiments, silicon is not transparent in the visible and NIR wavelength range, where many single-photon devices (such as quantum dots or quantum memories) and detectors work. One more advantage is that coupling losses in FLM written waveguides are much smaller with respect to the ones in Silicon photonics.

Concerning the drawbacks of Femtosecond Laser Micromachining we can highlight that, at variance with lithographic techniques, allowing to get an index contrast between core and cladding of $\Delta n \approx 1$, in the case of laser written guides, Δn ranges from 0.001 to 0.01. This means curvature radii will need to be much larger to ensure the same curvature losses. Furthermore there exist other platforms capable of realizing optical circuits showing lower propagation losses with respect to FLM[37]. Finally, even if the production time for the single chip with FLM is not dramatically high, the technique doesn't allow to have a very efficient parallelization of the process. For this reason, for large scale production, lithographic techniques are still preferable.

2.2 Light-matter interaction at the femtosecond timescale

When ultrashort light pulses are tightly focused in a transparent material, very high peak intensities are reached (on the order of $10\ TW/cm^2$). In this situation different nonlinear absorption processes take place where a high amount of energy is deposited, *i.e.* in the region of the focus only. The consequences of this energy accumulation could lead to a localized modification of the refractive index[35].

The reason why this modification is limited to the focus region is the fact that the energy gap E_g of the dielectric material is greater than the laser photon energy. Thus linear absorption induces no change in the material. At higher intensities, like the ones that can be achieved in the focus using a laser in the mode-locking regime, photons can be absorbed through nonlinear phenomena, like multiphoton, tunneling and avalanche ionization[38].

Multiphoton ionization consists in the simultaneous absorption of n photons, so that the absorbed energy, $nh\nu$ is larger than E_g; this process typically dominates tunneling ionization that takes place as the very high electric field of the laser pulse lowers the energy barrier of the Coulomb potential, enabling electrons to tunnel from the valence to the conduction band. Finally, in avalanche ionization,

the strong electric field accelerates a free electron at the bottom of the conduction band, leading its kinetic energy to a value so high that this first electron can ionize another carrier. The free electron density, so, grows exponentially[38].

The duration of the pulse strongly influences its energy peak. As a consequence, by virtue of the fact that longer pulses would allow the avalanche effect only, to have all the three processes femtosecond pulses are needed[39].

The combined effect of these processes is responsible for the creation of a plasma and, even if the mechanism at the origin of the femtosecondlaser machining is still not fully characterized, it is well accepted that the energy transfer from the free electron gas to the lattice causes the modification. In particular, when the plasma has a low energy, the result is an isotropic modification; for intermediate energies the result will be a birifringent change of the refractive index n; finally for higher energy, empty voids and micro explosions will appear because of the ultrahigh pressure arising in the focal volume[35].

When avalanche ionization is taking place the electron density keeps growing, so that the plasma frequency is lowered. As it matches the laser frequency, photons are directly absorbed by electrons in the focal volume (through linear absorption): a consistent amount of the pulse energy is directly deposited in the plasma. That energy is then released to the ionic lattice in the phase of "plasma relaxation", which is the ultimate responsible for the material modification. The whole process takes place on a time scale ranging between tens of picoseconds and microseconds. This ensures that the laser action and the real machining of material will happen at different timescales allowing to have a more precise and controlled modification. With pulses longer than femtoseconds, let's say in the range of picoseconds, this disentangling wouldn't be that effective. Furthermore the plasma, as already mentioned, would be generated mainly because of avalanche ionization which means it would have a more distributed seed with respect to the well confined plasma obtained in the presence of the other nonlinear processes too.

Other relevant mechanisms are thermal or photostructural. As a matter of fact the high temperatures in the focal volume melt the material in that confined region which is then rapidly re-solidified, inducing density variations (and so changing the refractive index too). An analogous change in density might be induced by a rearrangement of chemical bonds due directly to laser pulses. In crystals this rearrangement causes a decrease in density (since the starting point is an ordered lattice optimizing the atomic disposition) and generally n decreases. In amorphous glasses, instead, the refractive index will grow[41][42].

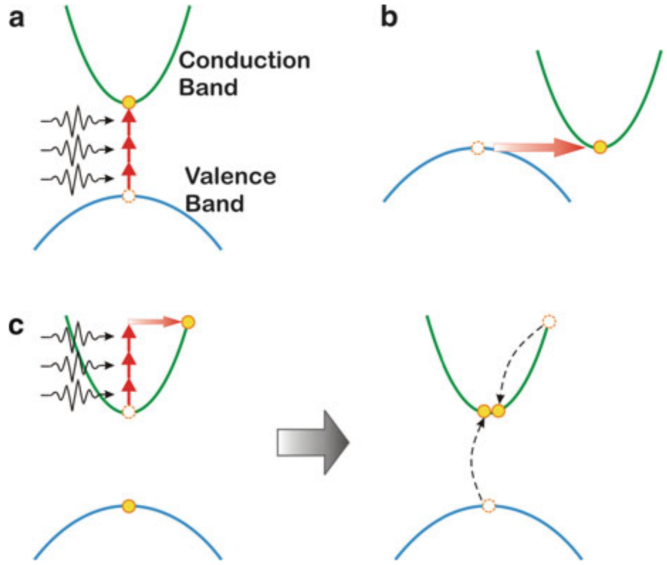

Figure 2.1: *This figure shows a schematic of the processes involved in femtosecond laser micromachining described in section 2.2: a. represents multiphoton absorption, b. tunneling ionization and c. avalanche ionization. The image is taken from[40].*

2.3 Fabrication parameters

2.3.1 Focusing

Let's start assuming that the femtosecond laser beam, focused through a lens, can be described as a Gaussian beam. In this situation the diffraction-limited waist radius is:

$$w_0 = \frac{M^2 \lambda}{\pi \mathrm{NA}}$$

where M^2 is the Gaussian beam propagation factor[43], λ is the free space wavelength and NA is the numerical aperture of the focusing objective. The quantity w_0 corresponds to half the spot size. The focus size in the direction of propagation is described by the Rayleigh range z_0, equal to half the depth of focus and given by the following expression:

$$z_0 = \frac{M^2 n \lambda}{\pi \mathrm{NA}^2}$$

being n the refractive index of the transparent material in which the beam is focused.

Aberrations, both chromatic and spherical, lead to a non ideal intensity distribution in the proximity of the focal volume (see also Figure 2.2), so that the equations above are no longer valid approximations. A distorted focus could result in an alteration in the waveguides fabrication, since the spatial region where nonlinear absorption is triggered is changed.

Chromatic aberration stems from dispersion (*i.e.* because $n = n(\lambda)$) thus it can be compensated using aberration-corrected optics for the wavelength range of interest. Spherical aberration comes from the fact that rays far from the optical axis, even if parallel to the axis itself, impinge with different angles on the lens surface. The larger the distance from the optical axis , the larger the angle, the less valid the paraxial approximation. Consequently they see a different refractive power from the lens and are focused in different points. Using aspherical lenses one can overcome this issue.

On the other hand, the fabrication of buried waveguides implies that some contributions to spherical aberration will be introduced by the air-glass interface. The entity of such contribution depends on the fabrication depth[33]. Thus a hardly avoidable dependence of the properties of waveguides on this parameter is introduced.

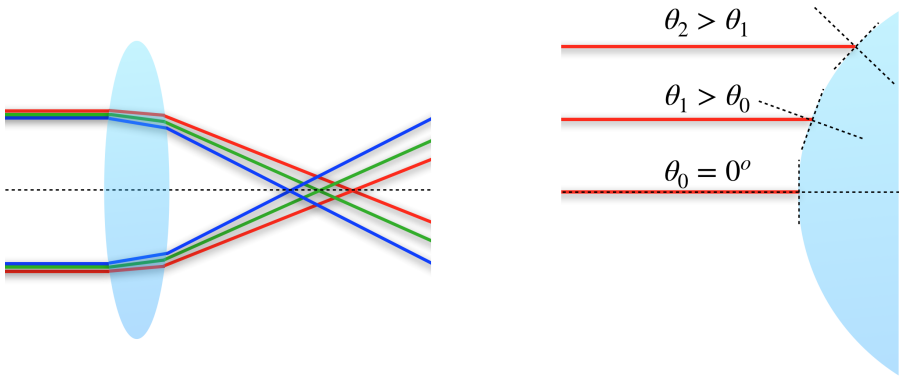

Figure 2.2: *Chromatic and spherical aberration prevent us from obtaining an ideal focus. The further the beam from the optical axis, the more relevant the spherical aberration.*

Other phenomena that influence the propagation of the beam in the material, and so, the energy distribution in the focal region, altering the fabrication are non linear effects such as self focusing and plasma defocusing.

When light propagates through a dielectric amorphous material ($\chi^{(2)} = 0$) there

are two contributions to polarization: the linear one and the one proportional to $|\mathbf{E}|^2\,\mathbf{E}$ which becomes non negligible for high-intensity fields (like the ones of ultrashort pulses). Because of this second contribution the overall refractive index becomes dependent of the field itself:

$$n = n_0 + n_2' \,|\mathbf{E}|^2 = n_0 + n_2 I$$

where $n_0 = \sqrt{1+\chi^{(1)}}$ is the linear refractive index, $n_2 = 3\chi^{(3)}/4\epsilon_0 c n_0^2$ is the nonlinear refractive index and I the laser intensity. We speak about Kerr's effect.

For most materials n_2 is positive, so there's an extra focusing effect. From a theoretical point of view, this self focusing could lead to the collapse of the focus to a point (instead of a spot). However the high intensity brings to the formation of a free electron plasma that besides absorbing linearly the radiation acts also as a diverging lens, counterbalancing the Kerr focusing effect[35]. Self focusing can be avoided making sure not to exceed the critical power.

2.3.2 Writing configuration

The standard writing geometries used to fabricate optical waveguides are the longitudinal and the transverse configuration[44].

- **Longitudinal configuration** The direction of relative motion between sample and beam is parallel to the beam itself. In this way the cross-section of waveguides is symmetric. The main drawback of this approach comes from the limited working distance of the writing optics (typically in the order of millimeters).
- **Transverse configuration** The sample is now scanned along a direction orthogonal to the beam. With this geometry there's no limit to the length of waveguides whose cross-section, though, will be elliptical (since $z_0/w_0 = n/\text{NA} \neq 1$). The asymmetry of the cross-section can be compensated with beam shaping techniques or multiscan writing approach, as described in section 2.3.4.

2.3.3 Repetition rate

Another important parameter for laser microfabrication is the repetition rate: the higher it is, the smaller the time between two consecutive pulses becomes. When two pulses are extremely close in time, the radiation absorbed from the first pulse

won't have diffused out of the focal volume when the second arrives, influencing the characteristics of written waveguides.

With a repetition rate of $1 - 200\ kHz$ we are in the so-called low-frequency regime. In this regime the modification is induced by the interaction between the material and single pulses. In this regime the typical values for the pulse energy and for the pulse width are a few μJ and $50-200\ fs$, respectively. The low repetition rate implies the need to work at very low processing speeds ($20 - 100\ \mu m/s$) and only low refractive index changes are achievable[38]. Moreover there's a big dependence of the waveguide cross-section on the focus shape: often beam shaping is needed to obtain good quality waveguides, as explained in the following section. The main advantages of this regime are:

- the possibility of working on a wide variety of materials.
- widespread availability of regeneratively amplified Ti:Sapphire lasers at $800\ nm$, which produce highly energetic femtosecond laser pulses with $1 - 200\ kHz$ repetition rate.

Moving to a high repetition rate, e.g. $5 - 25\ MHz$, the writing speed can be appreciably enhanced (up to tens of centimeters per second) and tuned to adjust the overlap between subsequent pulses so to change the relevance of thermal effects which influences the size of waveguides. On the other hand, with the energy range typical of this regime ($20 - 100\ nJ$ for the single pulse) there's the necessity of using tightly focused beams. As a result one needs to work close to the surface, frustrating the 3D capabilities of FLM[38]. Moreover[45] just a limited range of materials is processable in the high repetition rate regime.

There's also an intermediate working window, in the repetition rate range between $100\ kHz$ and a few MHz. Sources for this regime are Yb-based lasers[1], providing $\approx 300\ fs$ pulses in the Infrared region of the spectrum with energies around $1\ \mu J$ per pulse, so there's no need for tight focusing and the 3D capabilities of the process can be fully exploited. Moreover the combination of high energetic pulses and sufficiently high repetition rate allows to use good writing speeds and to get symmetric structures.

2.3.4 Multiscan approach and beam shaping

The cross-section of integrated optical waveguides influences the number of supported transverse modes and the spatial distribution of each guided mode. Fur-

[1] Which are typically compact and cost effective systems

thermore, because of form birifringence, it also determines the polarization dependency of various properties of the guide. For these reasons engineering the cross-section is crucial for many applications, in particular in the case of transverse writing configuration. In some cases the cross section can be determined using a multiscan approach[46][47] (in the order of twenty scans for the single guide) consisting in using a rotationally-symmetric laser beam to inscribe the waveguide. In the inscription process, at each scan, the irradiated path is translated along a line perpendicular both to the the sample translation axis and the beam propagation axis. Alternatively, since the cross-section is directly connected with the spatial distribution of the induced electron plasma in the single-pulse interaction regime, beam shaping techniques can be exploited too. These, though, are less flexible and straightforward with respect to multiscan. Indeed techniques like the astigmatic beam focusing[48, 49] or slit beam shaping[50, 51] don't allow a proper cross-section control in bends. A possible way to overcome this limitation, without moving to multiscan, is using computer controlled active optics (for example spatial light modulator and deformable mirror[52]) to make sure that the beam shape tailors properly the instantaneous relative motion between sample and laser.

2.3.5 Other considerations

For the sake of completeness we add the following list, containing a brief description of other interesting parameters that it is always worth considering at the inscription stage:

- **Translation velocity**: it determines the energy deposited per unit volume and so the property of the free electron plasma and, ultimately, of waveguides.
- **Writing direction**: it might change the laser-substrate interaction in the presence of a pulse front tilt, according to the so-called quill effect[53].
- **Pulse duration**: it influences the nonlinear propagation of the beam and, by extension, the intensity profile.
- **Laser wavelength**: like pulse duration affects non linear propagation, in particular determines the minimum number of photons to have a multiphoton absorption.

- **Light polarization**: it is for sure important in the intermediate power fabrication window, especially in the case of microstructures obtained after wet etching, as mentioned above.

2.4 FLM for integrated optics

This last section slightly departs from the previous ones, since here, instead of dealing with the fabrication process itself, we are going to describe two of the most useful elements of integrated optics: directional couplers and Mach Zehnder interferometers. These are pretty standard devices, but can be seen as the "building blocks" of more complex optical circuits.

Finally, the very last section of this chapter introduces a simple process to get active photonic devices with FLM.

2.4.1 Directional coupler

This is probably the most common device in the framework of integrated optics; as a matter of fact Mach Zehnder interferometers themselves, analyzed in the following section, are based on a couple of simple directional couplers. Its functioning principle can be explained by the coupled mode theory[54]. In a directional coupler two waveguides are, at least for a portion of their total length, brought close enough to be coupled through the evanescent field of each of the two guides. Even small imperfections in the fabrication would affect sensibly the behavior of the device, so it is a good benchmark for testing the capabilities of the fabrication process[31]. After that directional couplers were first obtained in borosilicate glasses in 2001[55], they have actually been fabricated in a good variety of substrates, proving the validity of FLM for writing waveguides. Moreover the capability to fabricate 3D optical elements allowed to demonstrate new configurations for directional couplers (like the so-called X-coupler or 3-port couplers: see also figure 2.4).

From a mathematical point of view, as any other optical element, directional couplers can be described in a matrix formalism. Let's start considering, with reference to figure 2.3, the case in which light is launched in the upper waveguide only. Define:

$$R = \frac{P_{out,1}}{P_{in,1}}$$

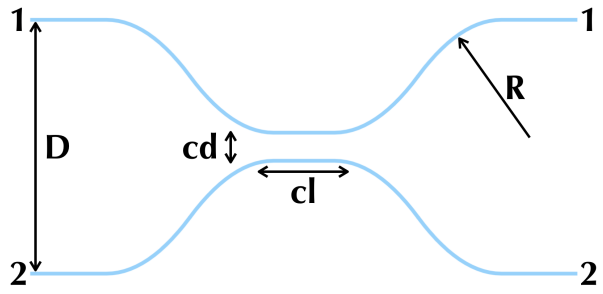

Figure 2.3: *This is a schematic of a directional coupler: when the two waveguides are at a distance D they are decoupled and there's no energy exchange between the two arms. As the guides bend, reducing the distance between them, there's an effective overlap of modes, maximum when the distance is cd (coupling distance). This overlap allows a power transfer that takes place over a total length $L = cl + L_{eff}$, where cl is the coupling length and L_{eff} accounts for mode-coupling along the bends. Another important parameter is the bending radius R: the milder the curvature the smaller the bending losses.*

$$T = \frac{P_{out,2}}{P_{out,1}}$$

which are, respectively, reflectivity and transmission of the directional coupler. Obviously $P_{out,2} + P_{out,1} = P_{in,1}$. The field transfer matrix for a loss-less coupler of this kind is:

$$\begin{pmatrix} E_{out,1} \\ E_{out,2} \end{pmatrix} = \begin{pmatrix} \sqrt{R} & i\sqrt{T} \\ i\sqrt{T} & \sqrt{R} \end{pmatrix} \begin{pmatrix} E_{in,1} \\ E_{in,2} \end{pmatrix} \tag{2.1}$$

In case of a balanced directional coupler $R = T = 1/2$. This is the only case which permits a full energy transfer between the two arms. Reasoning in terms of single photons, equation 2.1 can be recast in terms of the creation and the annihilation operator:

$$\begin{pmatrix} \hat{a}_{out,1} \\ \hat{a}_{out,2} \end{pmatrix} = \frac{1}{\sqrt{2}} \begin{pmatrix} 1 & i \\ i & 1 \end{pmatrix} \begin{pmatrix} \hat{a}_{in,1} \\ \hat{a}_{in,2} \end{pmatrix} \tag{2.2}$$

2.4.2 Mach Zehnder interferometer

A Mach Zehnder interferometer (in the following also MZI) can be realized using two balanced directional couplers adding in between them a phase shifter, as shown in figure 2.5.

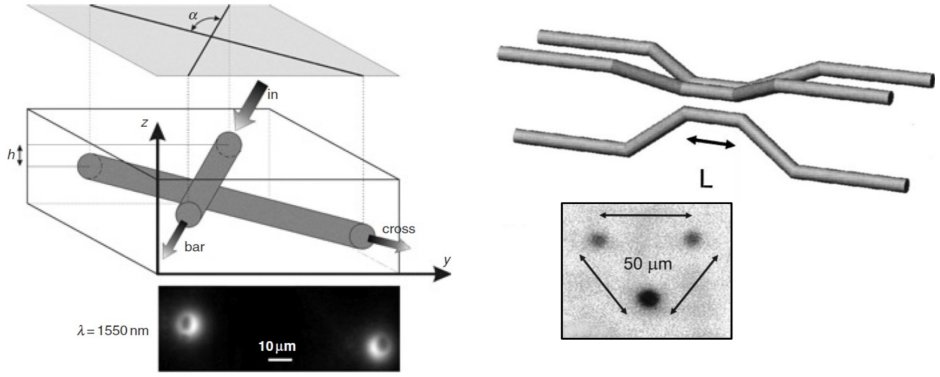

Figure 2.4: *In this figure, in the left panel, is represented a different configuration for a directional coupler: the so-called vertical X-coupler, where the two waveguides are on different planes. This solution is feasible thank to the 3D capabilities of FLM[56]. In the right panel, the schematic of a 3 $\times$ 3 symmetric directional coupler is shown. Again, this geometry is obtained exploiting the tridimensionality of the technique[57]. Pictures of the near field output are also reported.*

The working principle is basically the following: suppose to inject light in one arm only. The first coupler divides a light beam in the two outputs of the first stage. In the middle stage the two arms see different optical paths, so the two components acquire different phases. The last stage recombines light. For a lossless device the total power will be conserved, but the power at each output port will depend on the phase difference introduced at the second stage.

The first laser written MZI was accomplished in 2002 cascading two X-couplers[58]. Since then Mach Zehnder interferometers were fabricated on various substrates both using classical directional couplers and bifurcations.

Concerning the mathematical description: the transfer matrix for the second stage (*i.e.* for the phase shifter) reads:

$$\begin{pmatrix} e^{i\Delta\phi} & 0 \\ 0 & 1 \end{pmatrix} \tag{2.3}$$

Thus the fields at the output of the MZI can be found with the following expression:

$$\begin{pmatrix} E_{out,1} \\ E_{out,2} \end{pmatrix} = \begin{pmatrix} \sqrt{R_2} & i\sqrt{T_2} \\ i\sqrt{T_2} & \sqrt{R_2} \end{pmatrix} \begin{pmatrix} e^{i\Delta\phi} & 0 \\ 0 & 1 \end{pmatrix} \begin{pmatrix} \sqrt{R_1} & i\sqrt{T_1} \\ i\sqrt{T_1} & \sqrt{R_1} \end{pmatrix} \begin{pmatrix} E_{in,1} \\ E_{in,2} \end{pmatrix} \tag{2.4}$$

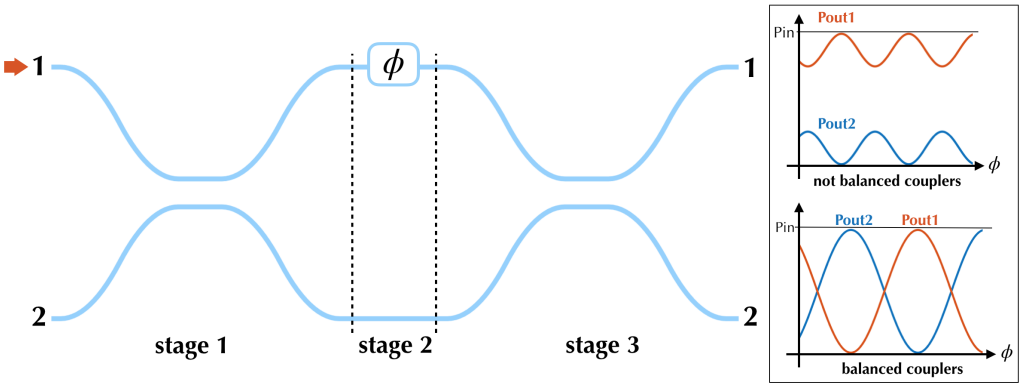

Figure 2.5: *As mentioned in the text, a Mach Zehnder interferomter is obtained cascading two directional couplers, in case with a phase shifter in between them. As depicted in the insert, if these couplers are balanced, a full power transfer is achievable, provided that that the two arms of the second stage present two identical optical paths. To compensate for differences due to the fabrication process a phase shifter is typically introduced.*

Being R_j and T_j the reflectance and the transmittance of the j^{th} coupler. Assuming $R \equiv R_1 = R_2$, and so $T \equiv T_1 = T_2$, form equation 2.4 one gets:

$$\begin{pmatrix} E_{out,1} \\ E_{out,2} \end{pmatrix} = e^{i\frac{\Delta\phi}{2}} \begin{pmatrix} Re^{i\frac{\Delta\phi}{2}} - Te^{-i\frac{\Delta\phi}{2}} & 2i\sqrt{RT}\cos\left(\frac{\Delta\phi}{2}\right) \\ 2i\sqrt{RT}\cos\left(\frac{\Delta\phi}{2}\right) & Re^{-i\frac{\Delta\phi}{2}} - Te^{i\frac{\Delta\phi}{2}} \end{pmatrix} \begin{pmatrix} E_{in,1} \\ E_{in,2} \end{pmatrix} \tag{2.5}$$

which could easily be recast in terms of single photons in the same fashion of equation 2.2.

2.4.3 Thermal phase shifters

A crucial feature of integrated optical devices is reconfigurability, which allows to compensate imperfections at the fabrication stage and implement dynamic circuits. A practical method to realize a reconfigurable chip is exploiting thermo-optics effect to tune locally the refractive index of waveguides. Basically a resistive heater is placed on the top of the optical chip, in the proximity of the waveguide whose refractive index has to be tuned. Then exploiting Joule's effect, a temperature gradient is induced in the glass, so that the closest waveguide (the one to be

tuned) is exposed to the highest temperature, and its refractive index will be the one that changes the most in the device.

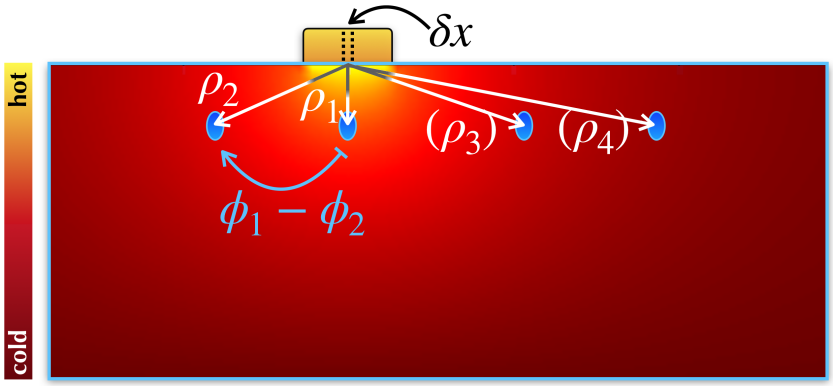

Figure 2.6: *The picture shows the section perpendicular to waveguides of an optical chip with a single heater. With respect to an infinitesimal portion of this heater we define* ρ_i *as the distance between that portion and the* i^{th} *waveguide. Ideally, being the heater placed above a specific waveguide, we would like the refractive index of that guide to be the only one that changes. Instead, because of thermal cross-talk, all waveguides are influenced. Such cross-talk cannot be avoided, however using many electrodes we can still obtain the wanted phase configuration.*

It's clear, from the discussion above and from image 2.6, that the properties of all waveguides are influenced by the presence of a single heater: we speak about thermal cross talk, which is actually unavoidable. Fortunately it doesn't prevent the realization of reconfigurable quantum circuits with FLM as shown by Flamini *et al.*[59], mapping the effect of each resistor on each phase and tuning consequently the various dissipated powers. In the same paper a theoretical analysis of the induced phase shift between two waveguides is carried out. It is proved that such phase difference is linear with the dissipated electrical power:

$$\phi = \phi_1 - \phi_2 = \Phi_0 + \alpha P$$

where Φ_0 is the phase shift between to the two guides in the passive device and the proportionality constant α reads:

$$\alpha = \frac{2n_T}{\lambda}\frac{1}{\kappa}\frac{L_{arm}}{L_{wire}}\ln\frac{\rho_1}{\rho_2} \tag{2.6}$$

With n_T we indicate the thermo-optic coefficient, λ is the wavelength, κ is the

thermal conductivity of the substrate, L_{arm} is the length of the straight segment in the interferometer's arms and L_{wire} is the length of the heater, assumed to be wire-like. Starting from this expression one can evaluate the expected phase change, for a given dissipated power. Moreover, in the case of a chip hosting more resistors, we have:

$$\phi = \Phi_0 + \sum_i \alpha_i P_i \tag{2.7}$$

where the subscript i runs on every couple phase shifter-resistor. Equation 2.7 accounts for the effect of every heater on the single phase shift (*i.e.* accounts for cross talk). Starting from this equation one can evaluate the optimal position of heaters to minimize both control effort and crosstalk[60].

From the practical point of view realizing an active optical circuit with FLM consists of these steps:

- Fabrication of a **passive device**, exploiting the standard FLM approach, but taking care to have the physical space on the chip to fabricate and wire the heaters. This might seem trivial, but actually isn't always that straightforward. As a matter of fact to have the maximum efficiency in introducing a phase shift through a heater, this should be placed in the straight part of the waveguide[2]. So at the design stage of the device the necessity of tunability should be accounted for.

- Deposition of a **metallic layer** on the top of the dielectric substrate. The choice of the material(s) for this metallic layer(s) should be driven by its(their) electrical properties (resistivity, resilience against oxidation, easiness of bonding) and how good the adhesion on glass is.

- The selective **ablation** of metal to define the electrodes in the correct position, as shown in figure 2.7.

[2]Even if, actually, electrodes might be realized on bends too[60].

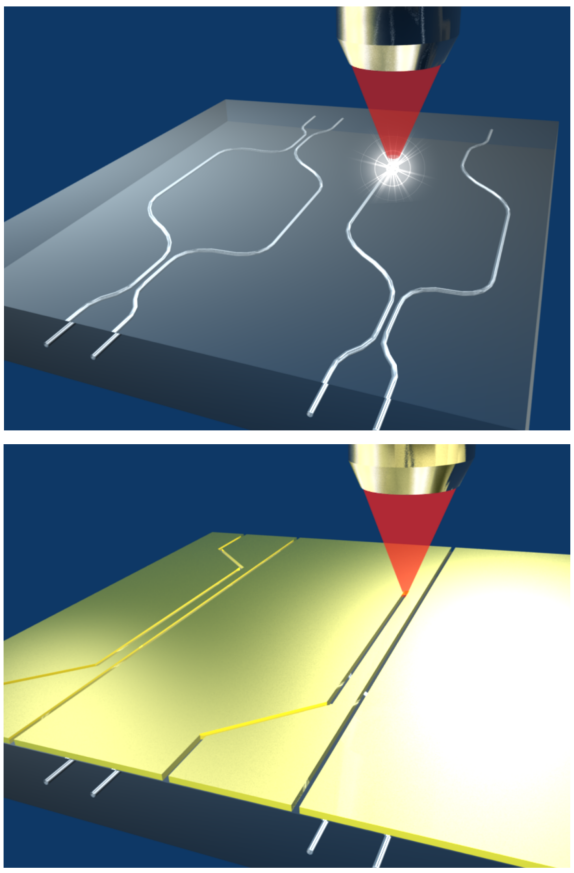

Figure 2.7: *After that waveguides are fabricated through FLM, as depicted in the upper panel, a metallic layer is deposited onto the glass. Then, as shown in the lower image, ablation are performed, focusing the laser beam at the metal surface: in this way the pattern of electrodes is defined. Schematic taken from[59].*

Chapter 3

Materials and methods

This chapter deals with the experimental work behind the Thesis. In particular the experimental setup, both for what concerns the fabrication and the characterization stages of optical waveguides, will be presented. Section 3.1 describes the femtosecond laser source used to write optical chips and the motion system needed to get relative motion between laser beam and sample. In Section 3.2 three procedure that have been implemented on the glass substrate before characterization are exposed. Specifically thermal annealing, wet etching and facet polishing will be described. Section 3.3 deals with the main steps of characterization: visual inspection, mode analysis, losses measurement and polarization behavior characterization.

3.1 Fabrication set up

The experimental setup used to fabricate the optical waveguides is shown is Figure 3.1. The output beam of a laser source at $1030\ nm$ goes through a half waveplate

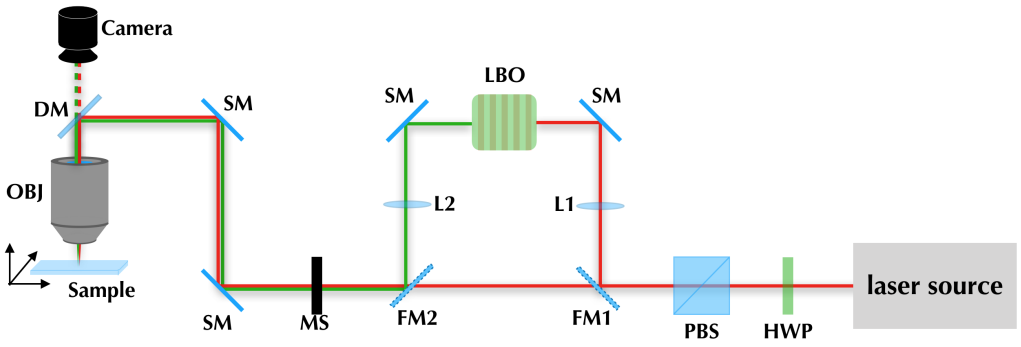

Figure 3.1: *Schematic of the fabrication set up. The output of the laser source is in the infrared region of the spectrum. It goes through a half waveplate (HWP) followed by a polarizing beam splitter (PBS), so that the output power can be tuned by rotating the waveplate. After the PBS a filp mirror (FM1) permits to choose whether using the first of the second harmonic. In the second case the beam is focused through a lens (L1) onto a lithium triborate crystal (LBO), then its former size is restored thank to another lens (L2) and a second flip mirror (FM2) redirects the second harmonic onto the path followed by the IR beam when FM1 is not reflecting the laser output. Phase matching is achieved tuning the crystal temperature. Regardless of the wavelength, the beam is not stopped only when the mechanical shutter (MS) is open. Thank to some silver mirrors (SM) and a dichroic mirror (DM) the laser beam reaches the objective (OBJ) that tightly focuses it onto the sample. The dichroic mirror lets the back-reflection from the sample surface impinge onto a CCD camera, allowing to choose the correct working distance and a good tilting of the holder on which the sample is glued.*

(HWP) followed by a Glenn-Thomson polarizer (PBS) in order to adjust the average energy per pulses. After these optical elements a reconfigurable set of dielectric mirrors allows to choose whether to use the first or the second harmonic (at 515 nm) of the source and to align the beam in the machining area. The second harmonic is obtained through a non-linear crystal whose temperature can be finely tuned to meet the phase matching condition.

There are two reasons that justify the presence of this line for second harmonic generation. First of all to improve (or, in some cases, allow) the machining of cer-

tain dielectric materials with a high energy gap (e.g. fused silica): a smaller wavelength enhances the efficiency of nonlinear absorption. Moreover, even in cases in which the writing wavelength is $1030\ nm$, by measuring the second harmonic efficiency we get a rough characterization of the repeatability of pulse duration among different fabrications. Indeed the pulse shape is highly dependent on conditions such as temperature, humidity or dumping and to make sure that a fabrication is as repeatable as it can be, apart from obvious parameters as the writing power, or speed, also the pulse shape needs checking.

Going back to the setup, at the machining area a microscope objective focuses the beam inside the sample. The chip is mounted onto a high precision three-axes stage. The laser beam is focused in the glass substrate through an objective mounted above this stage. Different objective might be used depending on the purpose of the fabrication. To fabricate the device waveguides we used an objective with numerical aperture, NA $= 0.6$ and magnification, M $= 50$. Such a high magnification permits to get a small focus and thus a high intensity in the focal region, necessary to have nonlinear optical effects. For metal ablation, instead, we opted for a different objective, with NA $= 0.25$ and M $= 10$. The smaller magnification leads to a bigger focus that eases the definition of the pattern of resistors, making negligible the bow of the glass surface and allowing a more continuous ablation of the metal.

At the alignment stage, a CCD camera collects the collimated light of the laser beam back-reflected by the substrate. This allows to obtain a precise and reproducible position of the sample with respect to the writing reference frame which is particularly important when an optical chip needs to undergo a second fabrication (for example to ablate the electrodes on the metal layer deposit onto glass, as already touched in section 2.4.3). The tilting of the sample is adjusted using a gimbal with two angular degrees of freedom. Finally a mechanical shutter, synchronized with the motion stage, enables the laser beam to reach the sample during the machining and blocks it when needed.

3.1.1 The laser source

The laser source is a cavity-dumped oscillator[61] developed in a collaboration between the Max Planck Institut of Heidelberg (Germany) and HighQLaser GmbH (Austria). The active medium is a $KY(WO_4)_2$, doped at 5% concentration with Ytterbium. Laser emission takes place at $1030\ nm$ wavelength. A InGaAs multiemitter laser diode bar at $980\ nm$ wavelength acts as a pump (absorbing around $15\ W$).

The cavity is long $8.9\ m$, but by the use of several mirrors its footprint is reduced to $90\ cm \times 50\ cm$. The laser system works in the mode-locking regime thank to a semiconductor saturable absorbing mirror (SESAM) which allows to achieve a mode-locking pulse train with a frequency of $17\ MHz$. The repetition rate at the output can tuned from few kHz to $1.1\ MHz$ with the adopted cavity-dumping system, realized through a Pockels cell followed by a thin film polarizer (see also figure 3.2). The electronics controlling the Pockels cell is synchronized with the pulses train by

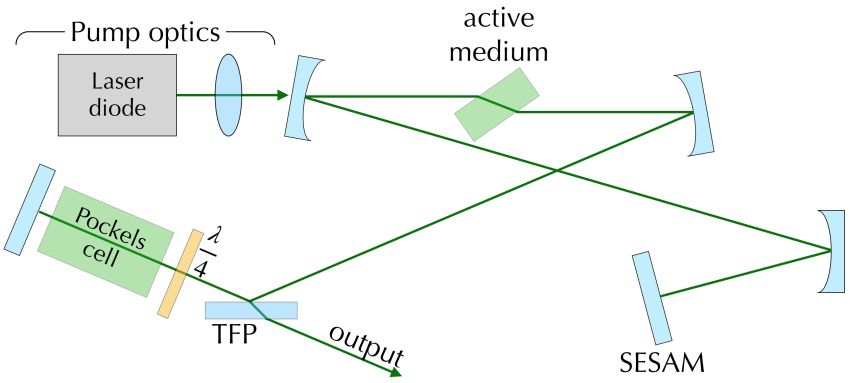

Figure 3.2: *The image represents the schematic of the typical set up of a cavity dumped laser. The system works in the mode locking regime thank to a semiconductor saturable absorbing mirror (SESAM) and is dumped by means of a Pockels' cell that properly rotates the beam polarization, allowing a part of the radiation to get out from the cavity through a thin film polarizer (TFP).*

mean of a fast photodiode placed into the cavity and the polarizer allows to dump a pulse only when the Pockel cell has properly rotated the beam polarization. Acting on the pump power and on the dumping ratio, the pulse energy can be tuned up to $1\ \mu J$ and the pulse duration can be tuned from $250\ fs$ to $400\ fs$, according to the pseudo-soliton regime sustained into the cavitypseudo-soliton-regime.

3.1.2 The motion stage

Aerotech 3D FIBERGlide three-axis motion stage enables the relative motion of the sample with respect to the focal point. The system is controlled by a PC and the motion programmed by G-CODE language (commonly used in CNC machining). Any arbitrary trajectory can be defined in a volume of $100\ mm \times 150\ mm \times 5\ mm$. The system combines air-bearing and non-contact brushless linear motors, which

enable very low friction between the moving parts, guaranteeing elevated smoothness in the translation. A very high precision in the positioning of samples is achieved: stage positions are controlled by optical encoders with a $1\ nm$ resolution, with errors smaller than $100\ nm$.

3.2 Post processing of optical chips

3.2.1 Thermal annealing

It has been proved[62] that post-processing multimode waveguides by thermal annealing it is possible to obtain single mode guides with enhanced confining properties and lower losses. The physical reason of this effect lies in the relaxation process induced by high temperatures. This relaxation releases the stress in waveguides both reducing the core size and increasing the core-cladding contrast. Furthermore the birefringence of annealed waveguides fabricated through multiscan FLM was found to be around twenty times smaller than the usual birefringence of FLM fabricated guides[34, 36]. This result extends the capabilities of laser-written optical waveguides permitting the fabrication of circuits dealing with polarization entangled photons. Now, before proceeding let's introduce the following characteristic temperatures for glasses, defined with respect to viscosity:

1. *Strain point*: Temperature corresponding to a viscosity of $10^{14.5}$ Poise ($10^{13.5}$ Pa·s). In this condition stresses in glass are released in few hours. The material is still solid and its shape is fixed. Below this point glass can be quickly cooled down without introduce any additional stress.

2. *Annealing point*: Temperature corresponding to a viscosity of $10^{13.4}$ Poise ($10^{12.4}$ Pa·s). At this temperature stresses are released in few minutes by viscous relaxation.

3. *Softening point*: Temperature corresponding to a viscosity of $10^{7.65}$ Poise ($10^{6.65}$ Pa·s). The glass is soft enough to deform under its own weight at a rate of 1 mm/min.

The idea is bringing the optical chip above the annealing point, without exceeding the softening point, then to cool it very slowly (mimicking an adiabatic transformation) below the strain point, so to release all the stresses, without deforming the sample. Since the device object of this Thesis was realized in a Borosilicate glass,

we followed a recipe for annealing already tried in our laboratories for the same glass, but for different waveguides[34]. The recipe prescribes to heat the sample with a rate of $100°$C/h until it reaches $600°$C, then with a ramp of $75°$C/h for two hours, for a peak temperature of $750°$C, above the annealing point for this material ($722°$C). Finally the chip is brought back to room temperature with a ramp of $-12°$C/h. The total annealing time is around 72 hours. Performance of the resulting waveguides are analyzed in the second part of this elaborate.

3.2.2 Etching

The importance of fabricating reconfigurable chips has already been exposed in Section 2.4.3. Consider now Figure 3.3, representing an electric model of the thermal resistances constituted of glass between the heater and the waveguide (R_1) and between the waveguide and the bottom of the substrate, where we assume to have a uniform temperature, (R_2). To maximize the efficacy of thermal phase shifter, R_1 should be as small as possible.

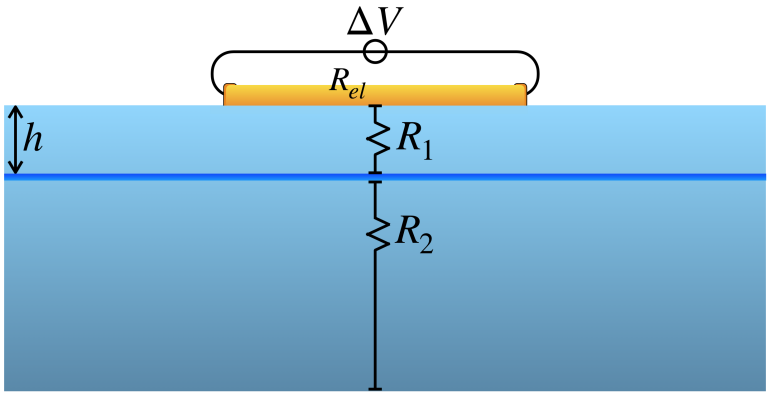

Figure 3.3: *Schematic of a micro-heater placed on the top of the sample in correspondence of a waveguide. To maximize the efficacy of the induced phase shift, R_1 should be as small as possible, thus h has to be minimized.*

From Fourier's law for heat conductivity the theoretical expression for thermal resistance is:

$$R_\theta = \frac{\rho}{A \cdot \kappa}$$

where ρ is the resistance length, A its area and κ the thermal conductivity of the material. Thus, to act on the value of R_1, one should either modify the thermal

conductivity κ of glass or change the geometrical parameters of the system. Obviously κ cannot be modified without altering the properties of the whole substrate, that implies changing the material of the substrate itself, and so the properties of waveguides as well. Therefore we must act on the only accessible geometric parameter to minimize R_1: the distance h between the glass surface and the waveguide. So it turns out that minimizing R_1 letting $\rho \to 0$, is completely equivalent to maximize the absolute value of coefficient α (see equation 2.6 where ρ, distance between the heater and the waveguide whose refractive index is the one want to change, is indicated as ρ_1; α is the proportionality constant between the phase shift induced and the dissipated electric power). From the practical point of view a smaller thermal resistance R_1 permits to reduce ΔV needed to perform a 2π phase shift, with benefits both for power consumption and cross talk. A good value for ρ is in the order of $15 - 30\ \mu m$: going below $15\ \mu m$ could lead to losses from light coupled out of the guide at the top surface of the sample.

The simplest way to reduce h is changing the fabrication depth. The main drawback is: the smaller the fabrication depth is, the higher the sensitivity to surface effects becomes, with the risk of having damaged or interrupted waveguides in correspondence of imperfections, dirt or dust on the sample at the writing stage. In some cases this approach has been successfully adopted[36], but it's not always feasible.

As a matter of fact, varying the wavelength at which optical guides are supposed to work, fabrication parameters change as well. There are situations where there's no fabrication window coping with both acceptable losses and small fabrication depth. A possible solution in these cases is writing optical waveguides at a higher depth, then etching the whole sample to reduce h.

This approach is the one that has been pursued in case of waveguides at $1550\ nm$, for which an optimal fabrication window was found at a fabrication depth of $220\ \mu m$ beneath the glass surface. The characterization of the etching process will be discussed in Chapter 5.

3.2.3 Glass polishing

In order to obtain a good coupling between waveguides and fibers or laser beams focused by an objective, both at the input and at the output ports, we need that:

1. the roughness of facets is low enough not to scatter the laser beam;

2. the cross-section of guides exposed at the glass sides is not dramatically different with respect to the one in the bulk of the sample[1];

A high roughness could stem from the fact that glass has been cut, before or after FLM. For example when cutting a sample with a diamond wire saw the resulting facets appear opaque at the inspection of the naked eye, so they clearly display a roughness sufficient to scatter visible light which is not acceptable for our applications. Concerning the cross-section of waveguides at the edge of the sample, it could be different with respect to the one in the bulk of glass because of the so-called tapering effect; it consists in the reduction of the waveguide cross-section as the laser approaches the edge of glass, due to surface effects affecting the shape of the writing beam.

Both issues can be overcome with a polishing process allowing to expose, on a low-roughness facet, good quality cross-section optical waveguides. This process is carried out with a polishing machine that removes from the facets a few hundreds of microns of glass with the aid of abrasive pads. The sample needs to undergo this process a few times, changing from one time to the other, the used pad (moving from higher to lower rugosity: the first disc shows a nominal roughness around $30\ \mu m$, the final one of $0.3\ \mu m$).

3.3 Characterization set up

Chip characterization is constituted of different passages, which are briefly described in the following, together with the instrumentation needed for each step.

3.3.1 Visual inspection

The fist characterization step is a vision inspection of the fabricated waveguides to make sure, by looking at the top of the sample, that they are not interrupted or damaged. The observation of the lateral facets, instead, permits a rough evaluation of the waveguides cross-section and of the sample polishing. In order to do this a Nikon ME600 microscope is used. It is equipped with a Differential Interference Contrast module, exploiting interference effects to improve the vision of small index variations. To take picture of the microscope image a CCD camera is mounted on it.

[1]This is for sure true for the waveguides fabricated for this Thesis, in other cases an "adiabatic tapering" of the guide might be helpful to reduce coupling losses.

3.3.2 Classical light characterization

Even if the goal of this work is the realization of an integrated optical circuit for a quantum optics experiment, the device characterization can be performed using classical light. As a matter of fact, measuring the behavior of the device with a classical light signal, is much more practical and time saving with respect to the quantum approach, but completely equivalent from the standing point of losses, internal phases and polarization behavior.

The source used for this passage is typically a laser diode at the same wavelength of the source needed for the final quantum experiment. There are two possible configurations, as depicted in Figure 3.4a and 3.4b. In the first case an objective or an aspherical lens is used to focus a collimated beam at the input facet. In the other one, the so-called "fiber-butt-coupling" is shown: a single mode

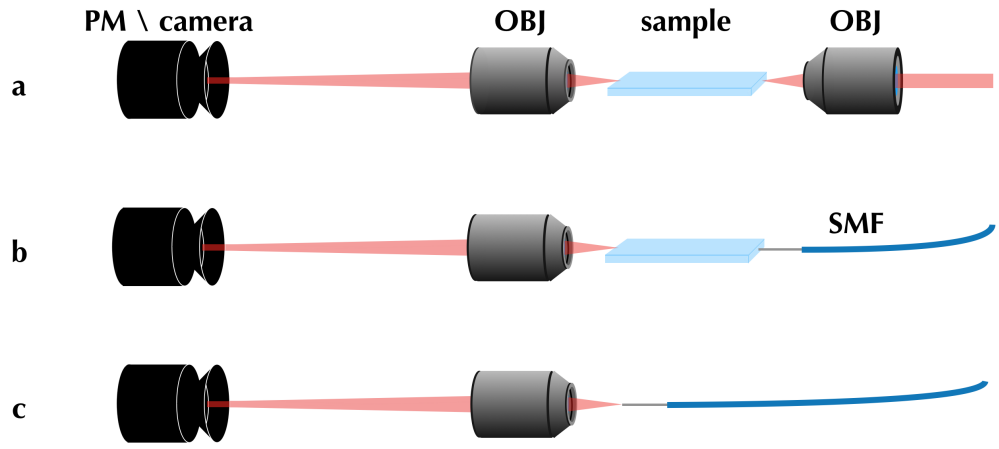

Figure 3.4: *These figure schematizes the typical arrangements used for the characterization set up. In case **a** two objectives are used to launch and collect light from the sample, this allows to have a quick alignment and a good estimation of the output ratios. Launching light with a fiber (as in Panel **b**) permits a better estimation of losses, which could be further improved using a fiber also to collect light. For a correct estimation of losses one needs to know what's the transmission of the fiber-collection objective system, measured as in **c**.*

fiber (SMF) is cut, peeled and used to launch the laser beam into a waveguide. A good efficiency is obtained provided that the beam waist of the focal point, if using an objective, and the mode size, in the case of fiber-butt-coupling, are similar to the mode radius of waveguides. In the case of an objective, the numerical

aperture of the launching optics and the one of waveguides should be comparable as well. For both configurations a precise and stable mounting is required. For this reason some precision micropositioners are exploited. In standard measurements the fiber (or the objective) is mounted on a manual three-axes manipulator (NanoMAX, Melles Griot). The same arrangement is used for the collection objective, which, like the excitation optics should ensure relatively low losses at the wavelength of interest. The sample, instead is fixed on a four axes micropositioner (MBT 402, Thorlabs).

In case of measurements requiring the use of fiber arrays or, in general a very high precision, a couple of Hexapods (PI, H-811 Hexapod Microrobots) replaced the three-axes manipulators, allowing an optimal alignment thank to the possibility of aligning not only along the x, y and z axes (with the very high spatial resolution of $40\ nm$), but also the "roll", "pitch" and "yaw" angles. In particular the rotations around these axes can be obtained fixing arbitrarily the pivot point and thus reaching the highest possible precision in the alignment.

3.3.3 Mode profile

The analysis of the spatial distribution of the intensity profile $I_{wg}(x, y)$ of a guided mode is of particular interest for the characterization of a waveguide. First of all such analysis allows to understand whether the guide supports one or more modes: having single mode devices is crucial for many applications. Furthermore, knowing the mode profile of the waveguide one can estimate the coupling losses by comparing it with the mode profile of the fiber that is going to be used to launch light in it.

To measure $I_{wg}(x, y)$, when the waveguide is coupled using the fiber-butt configuration, the near field profile of the output mode is imaged onto a high sensitivity vidicon camera (Hamamatsu C2400-03A), revealing the whole visible range and the near infrared region of the spectrum up to $1800\ nm$. The waveguide output is typically attenuated to make sure that the dynamic response of the camera is not saturated. The intensity profile is correctly retrieved through a MATLAB analysis of the acquired image, thank to the comparison of this with the near field image of the output of the launching fiber (with a well known mode). The fiber is imaged with the magnification previously used for the waveguide, in order to allow the proper calibration.

In the case of a single mode waveguide, by virtue of the fact that no inversion takes place in the expression of the profile of the fundamental mode, the expres-

sion of the electric field distribution is directly linked to the one of the intensity and:

$$|E_{wg}(x,y)| = C\sqrt{I_{wg}(x,y)} \tag{3.1}$$

C is a constant which can be neglected, since we are interested in the normalized profile. The overlap integral of the guided mode and the fiber mode allows to find an estimate for coupling losses.

3.3.4 Losses characterization

In general, to characterize losses, light is launched in the device using a fiber (which allows a better estimation of losses with respect to an objective), like in Figure 3.4b, and collecting the device output with a lens or a microscope objective.

Let P_{out} be the measured power at the output of the waveguide and P_{in} the one at the input, i.e. the fiber output imaged on a power meter head with the same optical system used to collect light from the device, like in Figure 3.4c. By definition, we call **Insertion losses** (IL) the total losses caused by the presence of device in between the fiber and the collection objective. They are typically expresses in a logarithmic scale and their mathematical expression reads:

$$(IL)_{dB} = -10\, log_{10}\left(\frac{P_{out}}{P_{in}}\right) \tag{3.2}$$

An alternative expression for IL, in the case of a straight waveguide, is the following:

$$(IL)_{dB} = CL + FL + PL \cdot l \tag{3.3}$$

Where CL indicates Coupling losses, FL stands for Fresnel losses, PL represents propagation losses and l is the device length.

Coupling Losses originate from mode mismatch between the fiber launching the light signal and waveguides. They can be evaluated numerically from the measured mode profiles starting from the following expressions:

$$CL = -10\, log_{10} O \tag{3.4}$$

being O is the so-called overlap integral,

$$O \equiv \frac{|\iint E_{wg} E_f dx dy|^2}{\iint |E_{wg}|^2 dx\, dy \iint |E_f|^2 dx dy} \tag{3.5}$$

where E_{wg} and E_f are respectively the field profile of the waveguide and of the fiber.

Fresnel losses are due to Fresnel reflection at the fiber-air-device interface at the input and at the device-objective interface at the output. For the single interface, from basic optics, we have:

$$FL_1 = -10\,log_{10}T_F = -10\,log_{10}\left\{1 - \frac{(n_{glass} - n_{air})^2}{(n_{glass} + n_{air})^2}\right\} \tag{3.6}$$

Corresponding, for an air-glass interface, to a loss around the 4%. Thus Fresnel losses are usually assumed to be 0.18 dB for the single interface, which means their total contribution in equation 3.3 is 0.36 dB.

Propagation Losses are theoretically zero, since in a perfect waveguide, light should propagate with no loss at all thank to total internal reflection. Naturally in real waveguides this is not the case because of non-uniformities and roughness in their structure. Propagation losses are defined per unit length and can be extracted from 3.3 once that the other two contributions are known:

$$PL = \frac{1}{l} \cdot (IL - CL - FL) \tag{3.7}$$

Finally, in case of non-straight waveguides one needs to account for **bending losses** too. Their origin stems from the deformation of the mode as the waveguide bends. In other words, a straight waveguide hosts perfectly the propagating electric field whose wave-vector is position and time independent, and so the bend isn't compatible with the natural path of the hosted mode itself. The field has to readapt its shape continuously as the curve takes place. Bending losses (BL) are referred to straight guide losses according to the definition:

$$BL = -\frac{1}{l_{bend}} \cdot 10\,log_{10}\frac{P_{out\,bend}}{P_{out\,straight\,guide}} \tag{3.8}$$

Where l_{bend} is the length of the bending trait, $P_{out\,bend}$ and $P_{out\,straight\,guide}$ are, respectively, the measured output power from the bended and of the straight guide.

It can be inferred, from the description above, that the milder the bend, the more progressive the readjusting of the mode, the smaller the losses. Therefore a high curvature radius leads to smaller bending losses, but implies to have a longer device, which means higher propagation losses. In conclusion the final expression for IL is:

$$(IL)_{dB} = CL + FL + PL \cdot l_{straight\,traits} + BL \cdot l_{bending\,traits} \tag{3.9}$$

At the design stage, the optimization of the device geometry, requires to minimize this quantity.

3.3.5 Polarization behavior characterization

For application like quantum optics experiments based on polarization entangled photons, as the one analyzed in the second part of this Thesis, it becomes necessary to fabricate polarization insensitive circuits. This is achievable exploiting the annealing process exposed above. To verify that a device is actually polarization insensitive one has to characterize it for different polarization states of light, comparing the power distributions at the output for the various cases.

This can be done in an objective-objective setup putting in front of the launching lenses a polarizer (could be a polarizing beam splitter, PBS) that fixes a specific polarization (e.g. vertical) followed by a half-waveplate (HWP) allowing to quickly rotate the polarization state of light (from vertical to horizontal). For instance, if the splitting ratio measured at the output of a directional coupler is independent of the waveplate orientation, one can say that coupler to be polarization insensitive. Directional couplers are, in general, the fundamental building block of all the circuits we dealt with throughout this Thesis. For this reason having verified at the beginning of the process that we are working with polarization insensitive couplers, we can proceed with the following fabrications, checking just the polarization insensitivity of the final device.

Chapter 4

Quantum simulation of Benzene

In this Chapter we start moving towards the actual project of this Thesis: the realization of a tunable integrated optical chip for the quantum simulation of the Benzene molecule. This chip is going to be used at the Institute for Quantum Optics and Quantum Information in Vienna, where the quantum measure will be performed in the next months. The main constraints and specifications about the design and performance of the device were set by the typical limitations of single photon measurements: high losses and the necessity of preserving the coherence of single photons from the source to the detector.

If the preservation of coherence is somehow granted by the use of integrated optics itself, the reduction of losses, instead, has been one of the challenges of the project. Another relevant specification was the necessity to get a high reconfigurability of the optical circuit. This allows to have a more versatile device, capable of simulating different systems (or different states of a certain system) depending on the chosen parameters.

This Chapter presents the theory behind the quantum experiment and an overview of the design of the device, clarifying the origin of the project specifications.

4.1 Valence bond and Spin function

Electrons in molecules cannot be pictured as classical particles: their dynamics can be properly described in a quantum framework only. The molecular orbital theory could be a relatively effective and simple approach, as long as we are neglecting the breaking of chemical bonds. According to this picture electrons are not attributed to any specific bond, but they are, on the contrary, free to move across the whole molecule under the influence of nuclei. The analytical expression of these orbitals is going to be of the form:

$$\psi_j = \sum_{i=1}^{n} c_{ij}\chi_i$$

being χ_i the orbitals of the atoms of which the molecule is made of and c_{ij} the coefficients of the summation. They could be extracted by solving the Schrödinger equation and applying the variational principle.

More refined models, like Density Functional Theory (DFT) or Configuration Integral (CI), instead, are extremely heavy from the computational point of view. In this scenario, the so-called Heitler-London (HL) method, identifying the origin of covalent bonds in exchange effects, turns out to be a useful tool in modern Valence bond theory. As a matter of fact it is more complete than basic methods, still being, typically, less demanding than other approaches.

This exchange effect stems from the overlap between the wavefunctions of the atoms participating to the bond. Such overlap comes from the fact that the orbitals involved in the chemical bond are intrinsically non-orthogonal, which is actually the reason of the difficulty in describing physical systems of this kind. Furthermore, it is known that in covalent bonds between different atoms an ionic structure is present too, *i.e.* the distribution of electrons allows to identify an atom to which we can attribute a positive charge and one we consider negatively charged. Basically the electronic cloud is deformed by the different electronegativity of the various nuclei. For this reason a wavefunction describing this model needs to account both for a covalent and for an ionic part.
The most general expression, already accounting for both contributions, is known as Spin-Coupled wavefunction[63] and reads:

$$\Psi_{SC} = \mathcal{A}\{\psi_1^2 ... \psi_{n_c}^2 \phi_1 ... \phi_N \Theta_{00}^{2n_c} \Theta_{S,M}^{N}\} \tag{4.1}$$

where

- $\mathcal{A}$ is an antisymmetrizing operator.

- n_c is the number of core electrons, those electrons that do not take part in chemical bonds.
- N is the number of valence electrons, which may be involved in bonds.
- ψ_1, ..., ψ_{n_c} represent core orbitals that, being so, are doubly occupied. These wavefunctions are normalized and orthogonal to each other.
- ϕ_1, ..., ϕ_N stand for the valence orbitals, so they are singly occupied and, to lead to an effective overlap allowing the formation of a bond, are non-orthogonal among them: $\langle\phi_i|\phi_j\rangle = \Delta_{ij}$. They are anyway supposed to be orthogonal to core orbitals.
- $\Theta_{00}^{2n_c}$ is a many electron spin function. It describes the coupling of the spin of the $2n_c$ core electrons. Since each orbital is doubly occupied the net spin pertaining to a specific orbital is going to be zero. Considering all couples, $\Theta_{00}^{2n_c}$ can be expressed as:

$$\Theta_{00}^{2n_c} = \frac{1}{\sqrt{2}}(\alpha_1\beta_2 - \beta_1\alpha_2)\,...\,\frac{1}{\sqrt{2}}(\alpha_{2n_c-1}\beta_{2n_c} - \beta_{2n_c-1}\alpha_{2n_c})$$

- $\Theta_{S,M}^{N}$ is an electron spin function too, but here orbitals are not doubly occupied: valence electrons are going to be active electrons and they are going to show an overall spin S, with z-component M. Being singly occupied, there's plenty of possibilities for combining these N valence electrons. It could be shown that, actually, the number of permutations is:

$$f_S^N = \frac{(2S+1)N!}{(\frac{1}{2}N+S+1)!(\frac{1}{2}N-S)!}$$

  In particular, $\Theta_{S,M}^{N}$ is the linear combination of all the linearly independent spin functions:

$$\Theta_{S,M}^{N} = \sum_k c_{sk}\Theta_{S,M,k}^{N}$$

  There are various ways to construct these functions. Since we are interested in the case of Benzene, that has six valence electrons, we can use the so-called Rumer basis method.

  These spin functions contain an appreciable amount of information about the correlation between the various electrons participating to a bond. In particular this is the part of the wavefunction embedding the distribution of charge among the different ions constituting the molecule when this attains a certain state.

4.1.1 The Rumer basis method

As stated above, the electron spin function $\Theta^N_{S,M}$ can be expressed on various bases. The advantage of using the Rumer basis approach consists in having a straightforward method to visualize which particles will concur (and how) to a certain element of the basis.

The procedure, having N valence electrons, is the following: place N numbered dots in a circle and join them in pairs such that the joining lines do not cross. The simplest case is the one with $N = 4$ [63].

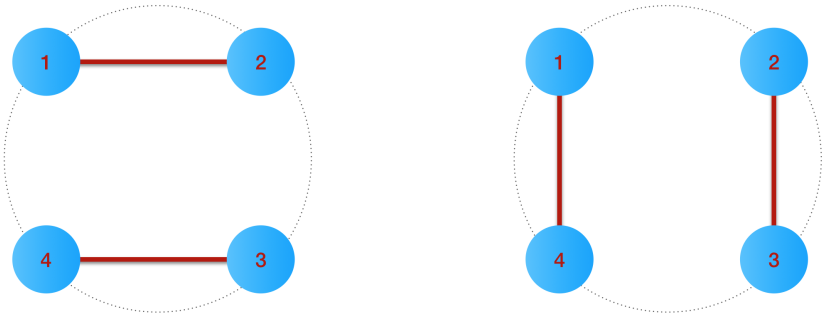

Figure 4.1: *These are the elements of the Rumer basis for a system counting four electrons. They are obtained connecting couples of dots in such a way that the connections never intercept.*

So it follows that the basis counts two elements:

$$\Theta^4_{0,0,1} = \frac{1}{\sqrt{2}}(\alpha_1\beta_2 - \beta_1\alpha_2)\frac{1}{\sqrt{2}}(\alpha_3\beta_4 - \beta_3\alpha_4)$$

$$\Theta^4_{0,0,2} = \frac{1}{\sqrt{2}}(\alpha_1\beta_4 - \beta_4\alpha_1)\frac{1}{\sqrt{2}}(\alpha_2\beta_3 - \beta_3\alpha_2)$$

For $N = 6$, *i.e.* for the Benzene molecule, we have five possibilities[64]: see Figure 4.2.

Combining the elements of this basis one can construct the proper spin wavefunction for any electronic state of a six valence electrons system.

4.2 Overview of the experiment

The goal of the experiment is the simulation of some of the electronic states of Benzene so to be able to measure their energy. In this way an experimental recon-

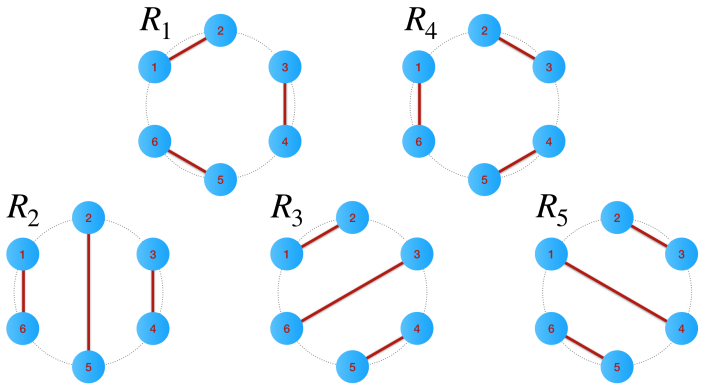

Figure 4.2: *Elements of the Rumer basis for a system counting six valence electrons, like Benzene.*

struction of the spectrum of the molecule could be obtained. The idea is to use an optical circuit implementing five unitary transformations (with five tunable parameters) to interact three couples of entangled photons and reproduce the molecule states.

Since the overall spin of the Benzene molecule is zero, three singlet photon pairs will be used. In this way the total spin of the wavefunction representing the photons launched in the chip will be the same (*i.e.* zero) of the one describing the electrons in the real system. Basically we will be mimicking each singlet electronic state with a singlet photonic state. In particular, exploiting the polarization insensitivity of the device, information will be encoded in the photons polarization starting from three entangled anti-symmetric Bell states:

$$|\Psi^-\rangle = \frac{|HV\rangle - |VH\rangle}{\sqrt{2}}$$

obtained from spontaneous parametric down conversion.

Being the SPDC a spontaneous process, the probability P of generating an entangled photon pair per each photon in the pump is $P \approx 10^{-3}$. The three pairs are independent of each other, thus the probability of having six single photons (three entangled couples) is P^3. For a set up like the one that is going to be used, taking into account both losses at the source and at the detection level, this means the six-photons event (in the absence of the chip) can be detected with a rate slightly smaller than 1Hz.

This clarifies why a high transmission in each waveguide is crucial. Being γ the losses for the single guide, the success rate, considering also the device, is going

to be rescaled by a factor $SR = (1-\gamma)^6$, as we are dealing with a six photons experiment. For example having $\gamma = 0.4$, $SR \approx 4.6\%$, whilst for $\gamma = 0.6$, $SR \approx 0.4\%$: one order of magnitude smaller than before. This is a non negligible improvement, especially considering that we were starting from a relatively low rate (smaller than 1Hz). Moreover, even in the cases in which all six photons reach the output of the device, still one cannot be sure that the measure was successful. This because the unitary transformation realized by the chip is not deterministic: there's the need to post-select only those events in which different photons didn't bunch on the same spatial mode. Finally, the probability of producing a certain wavefunction is state dependent: just to fix a figure, it can estimated to be on the order of 5%. Putting everything together the overall rate can be estimated to be in the order of approximately 10^{-2} Hz. This is just an estimation, but allows to understand the necessity of having low losses to make sure that the measurement time will be acceptable.

Dropping the experimental details and getting back to the theoretical ones, we can retrieve the energy spectrum from the output states considering the following Hamiltonian, that describes the Benzene according to the valence bond theory on the Rumer basis:

$$\begin{aligned} H = J_1(S_1S_2 + S_2S_3 + S_3S_4 + S_5S_6 + S_6S_1) + \\ + J_2(S_1S_3 + S_2S_4 + S_3S_5 + S_4S_6 + S_5S_1 + S_6S_2) + \\ + J_3(S_1S_4 + S_2S_5 + S_3S_6) \end{aligned}$$

where J_1 is related to the interaction strength between nearest neighbors, J_2 and J_3 to the one between second-order and third-order neighbors, respectively.

Given the high overall losses the implementation of a full quantum tomography on the output state, to reconstruct the density matrix of the system, is practically unfeasible, unless using a different and more efficient source, with a higher generation efficiency. But, as briefly mentioned in the first part of this work, QST is not always necessary to retrieve interesting information from an analog quantum simulation. Thus the main idea is implementing single qubit measurements on each single photon. In particular, to characterize the state, the expectation values of S_i will be measured, reconstructing a normalized value for the energy of the simulated state: knowing $\langle S_i \rangle$ for all the photons and for many states one gets an estimation of the Hamiltonian spectrum.

To implement this procedure (reconstructing the spectrum without having the

density matrix of the system), one needs to know the Hamiltonian and the eigenstates of the system under analysis since the beginning. Then, starting from these eigenstates one gets an experimental reconstruction of eigenvalues. To fix the ideas let us consider some examples for the case of Benzene described according to the Hamiltonian written above.

It is known[64] that, on the Rumer basis, the ground state and one of the excited state of Benzene (for what concerns their "spin part", as explained in the former section) are expressed as:

$$|g\rangle = (|R_1\rangle + |R_4\rangle) + \alpha_g \left(|R_2\rangle + |R_3\rangle + |R_5\rangle\right)$$

$$|e\rangle = (|R_1\rangle + |R_4\rangle) + \alpha_e \left(|R_2\rangle + |R_3\rangle + |R_5\rangle\right)$$

These states can be prepared tuning properly the splitting ratio of the circuit represented in Figure 4.3, that allows to control all the interesting phases needed to construct any linear superposition of three couples of entangled photons in a singlet state. At this point one measures for several runs the polarization of all the output photon (which encodes the spin) and gets an estimate of the eigenvalue.

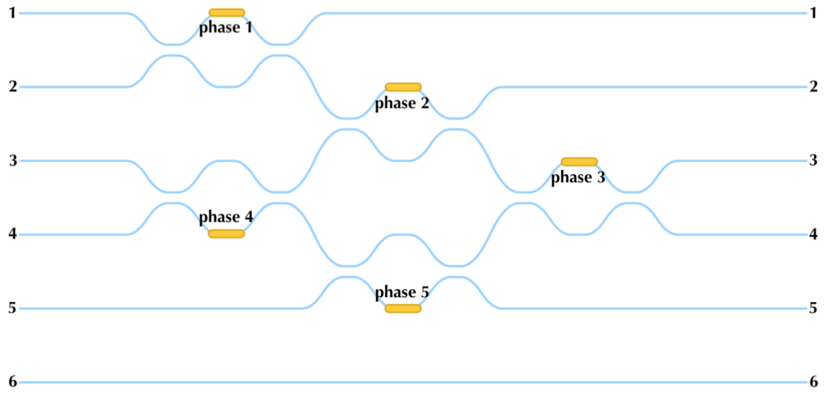

Figure 4.3: *This is a schematic of the optical device. It presents six waveguides and five tunable phases (tuned using the phase shifters represented as golden boxes), thus permitting to obtain any liner combination of the five Rumer basis for a six particles system.*

Were the eigenfunctions $|g\rangle$ and $|e\rangle$ unknown, one could find the expression of the ground state trying to minimize the measured normalized energy. The problem of excited states could be solved proceeding in a way similar to the one described in Section 1.3.1: implementing a witness operator that allows to find all the eigenvalues. Since this operator is based both on the energy and on the entropy of the

output state, which could be retrieved from the density matrix, a quantum state tomography would be required.

Other applications

The simulation of Benzene is for sure extremely interesting not only as a proof of principle for quantum simulation. Because of the presence of its aromatic ring, which is a crucial structure determining the behaviour of many other systems too, Benzene is an interesting case study also for chemistry and biology. On the other hand, the circuit shown in Figure 4.3 allows to control all the relative phases among the various photons, permitting, in principle, the simulation of other systems described through a six elements basis. For example it could allow to simulate the spin-interaction in a checkerboard lattice made up of six spins arranged in a fashion not far from the one consisting of four particles exposed in Section 1.3.2. Simulations of this kind could allow to study the presence of particular phase transitions in these spin systems and verify the validity of the models used so far to describe them. Thus, even if we are still far from having a universal quantum simulation, the device object of this work, thank to its flexibility, will show how versatile and effective nowadays devices can be.

4.3 The final device

Before proceeding with the next Chapter, we report here a possible design of the final device with a few additional features that may allow to make the quantum measurement easier. For what concerns the alignment, the six input (and the six outputs too) should be evenly spaced in order to allow their coupling by means of a fiber array. Furthermore, before aligning these optical elements, it is necessary to characterize the three photon sources. A possible way to do this, for a single SPDC source, is launching pairs of entangled photons in the inputs of a beam splitter and then measuring both the outputs. Were the beam splitter balanced, a perfect source of indistinguishable photons would lead to always have both photons on the same output of the beam splitter.

In our case three SPDC sources are present, so three beam splitters are needed to characterize all the sources and synchronize them. Clearly this could be done using bulky optical elements. A better option, to preserve the rest of the set up and have it ready for the ”6 photon chip”, is using a second integrated chip composed

of three directional couplers. On the other hand, the aforementioned alignment of six-input- and six-output- fiber arrays can be particularly time consuming. So aligning a first chip to characterize the sources, removing it and then placing on the set up the final device and re-optimizing the alignment would be very inefficient with respect to having both devices (couplers and six waveguides circuit) on a single sample.

For this reason, 50 μm under the actual device, three directional couplers will be fabricated. In this way, once the characterization of the sources has been done, one has simply to shift along the z direction the fiber arrays and quickly re-optimize the tilting, before making the final measurement (see also Figure 4.4).

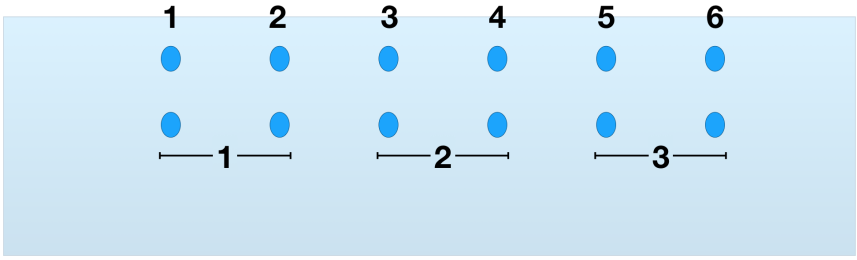

Figure 4.4: *Cross section of the (passive) final device. Under the optical circuit needed to implement the simulation, three directional couplers are fabricated to allow a quick characterization and synchronization of the three photon sources. It's worth pointing out how, even if there was no need to fabricate a 3D circuit for the quantum simulation, still the tridimensional capabilities of FLM came in handy for the final design.*

Chapter 5

Fabrication of the integrated photonic device

In this Chapter we will present in detail the recipes adopted for the fabrication of the final device. In particular, the choice of the process parameters will be motivated taking into account both the specifications given by the quantum simulation experiment and the technological constraints of FLM. In order to have a reasonable time of measurement and make the quantum experiment feasible, beside a full reconfigurability of all phases, the chip has to show the highest possible transmission. Another important feature is the repeatability of losses among different waveguides, which means bending losses should be negligible.

Regarding the active part, an overview about operation stability of the induced phases will be presented. As a matter of fact the final measure is going to last several weeks: each phase-configuration of interest will be acquired a number of times, to properly reconstruct the quantum state. In other words the device will be operated in a quasi static regime and for this reason the effect of micro-heaters has to remain stable as time passes.

5.1 High transmissivity

As already reported, the device has to be fully reconfigurable and it should exhibit a very high transmission. To satisfy the former requirement, we need the waveguides to be as close as possible to the surface. As depicted in Figure 3.3, indeed, this maximizes the control of phases through thermal shifter. The most obvious solution would be fabricating in the first place the device close to the top surface of glass, focusing the beam of the femtosecond laser at a depth of around $15-30\ \mu m$. Doing so, though, it was not possible to identify a good fabrication window, ensuring low losses and repeatable fabrications. Often waveguides turned out to be interrupted, probably due to surface effects (Figure 5.1). For this reason, as already described in Chapter 3, we introduced a new fabrication step, consisting in the isotropic etching of the sample. Thus fabrication depth became a free parameter we had the possibility to choose afterwards, selecting the distance between the top surface and waveguides as a function of the etching time.

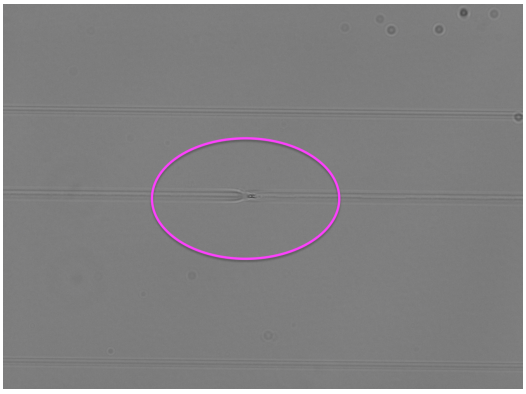

Figure 5.1: *In this microscope image the poor quality of waveguides directly fabricated close to the surface can be appreciated: often they were interrupted or presented unwanted scattering points.*

5.1.1 Etching process

First of all it was necessary to identify a good fabrication window for waveguides, ensuring both high transmissivity for straight waveguides and a low selectivity to hydrofluoridric acid attack. As a matter of fact it was demonstrated (mainly in other types of glass, e.g. fused silica) that the irradiated material typically shows a

much faster etching with respect to non-irradiated glass.

Therefore a set of different straight waveguides was fabricated in a substrate of borosilicate glass (Corning, EAGLE XG), scanning different fabrication velocities ($20\,mm/s$, $30\,mm/s$, $40\,mm/s$), powers (from $460\,mW$ to $580\,mW$ with step of $30\,mW$) and number of scans (from 4 to 10). These parameters were chosen relying on the results of past experiments performed with the same fabrication set up. The fabrication depth was still to be chose.

At the beginning we decided to fabricate this trial device at a depth of $170\mu m$ beneath the top surface. This depth was chosen since it had shown remarkable results for past experiments with the same fabrication set up and substrate. Being aware of the need of fabricating a set of couplers beneath the six photon device, we also studied transmission and the response to etching of a second set of waveguides $50\mu m$ deeper [1], meaning $220\mu m$ under the surface. Beside the single mode behavior, it was found out that waveguides at the latter depth were actually performing slightly better in terms of transmission, as can be inferred from the following table, showing parameters and propagation losses for the optimal waveguides at the two different depth:

Table 5.1: *In this Table the fabrication parameters and losses of the best waveguides fabricated at two different depth (*$170\ \mu m$ *and* $220\ \mu m$*) are reported. The best performing ones are the guides at higher depth.*

Depth	Power	Writing speed	Scans	Propagation Losses
$170\ \mu m$	$520\,mW$	$40\,mm/s$	8	$0.34dB/cm$
$220\ \mu m$	$520\,mW$	$40\,mm/s$	6	$0.29dB/cm$

Figure 5.2 shows the mode of the waveguide at $170\ \mu m$. It was verified that this waveguide supports a single mode with a mode size (calculated with the method described in Section 3.3.3) of $8.3\ \mu m \times 9.1\ \mu m$. The same analysis was performed for the waveguides at $220\ \mu m$. In this case the mode size was: $8.0\ \mu m \times 8.8\ \mu m$.

The overlap integral, estimated numerically comparing the waveguide mode with the one of a standard single mode fiber (SMF-28) at telecom wavelength used to couple light in the device, is larger than the 98% for the waveguides at $170\mu m$

[1] The distance of $50\ \mu m$ was selected to prevent any coupling between the two top and bottom groups of waveguides

and around 95% the ones at $220\ \mu m$. Corresponding to coupling losses of $0.09dB$ and $0.22dB$ respectively.

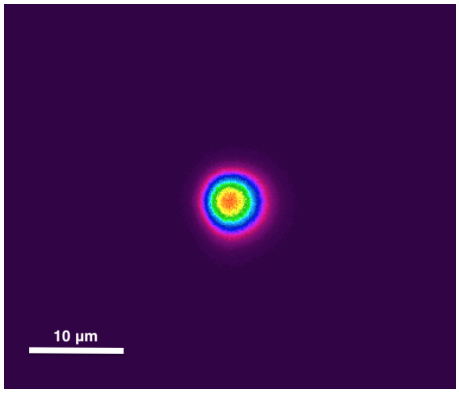

Figure 5.2: *The Figure shows the mode of the waveguide at* $170\ \mu m$ *of depth. We clearly have a single mode whose overlap with the one of the single mode fiber used for the characterization is larger than 98%.*

Taking into account the performance of waveguides at $220\ \mu m$ with respect to the ones at $170\ \mu m$ we studied the transmission at other fabrication depths, to find whether there was an even better set of parameters. Results at $245\ \mu m$, $270\ \mu m$ and $295\ \mu m$ were comparable with the ones at $220\ \mu m$. Considering the drawbacks of etching more material (time consumption and brittleness of the sample given by a thinner glass), we decided, when selecting the parameters for directional couplers, to circumscribe our study of curvature losses for waveguides at $170\mu m$ and $220\ \mu m$.

Before doing that, though, we had to define the etching parameters. The etching rate for the Borosilicate glass used as substrate for our fabrications was (from data-sheet parameters) in the order of $1\ \mu m/min$ when using a 10% HF solution at 22 Celsius degrees.

As expected, during the etching process, the irradiated material was removed faster than the non-irradiated one. This can be appreciated in Figure 5.3. Luckily the waveguides written with the parameters optimizing losses turned out to be among the ones with the closest etching rate to the substrate, allowing to preserve good quality waveguide in the bulk of the sample. Clearly one has to polish again the surface, removing a few hundreds of microns of glass, to cancel completely the effect of etching on the facet of the sample and be able to couple light into the device. We didn't notice any dramatic difference in the etching among the various depth.

A full characterization of the etching process was done on a sample with waveguides at a depth of $170\ \mu m$. So we had to remove around $140\ \mu m$ of glass from the top of the surface. In ideal conditions, this would correspond to around two hours and 20 minutes of exposure to HF solution. On the other hand, we wanted to make sure that the top surface only got etched and that no material was removed from the bottom facet of the sample. This because the sample was supposed to be as thick as possible to minimize its mechanical brittleness, compatibly with the necessity of making the waveguides close to the top surface. To make sure that the top face only was etched, we mounted the chip onto another slab of glass, gluing the two with some sealing wax, which is immune to HF attack. The sample immersed in the etching solution was pretty big (the overall exposed surface is around $25\ cm^2$). In this conditions the etching rate slowed down to $0.75\ \mu m/min$, on average. After something more than three hours of etching, we ended up with a sample around $850\ \mu m$ thick, with waveguides as close as $25\ \mu m$ to the top surface.

It's worth pointing out that we couldn't obtain the same result with a mechanical finish by virtue of the fact that it is not possible to get a micro-metric precision in such machining. Moreover a slight misalignment could have led to an uneven distance of waveguides from the top surface in different points of the device (meaning that the same waveguides in the proximity of the input facet could be, for instance, tens of microns closer to the top surface than in the proximity of the output one), compromising the efficacy of some thermal shifters.

These waveguides, after polishing, showed the same transmission they had before being etched. As expected, the buried devices hadn't been influenced by the chemical attack.

5.1.2 Directional couplers

At this point we had two candidate set of parameters for the straight waveguides, and we had to choose which one to use depending on the performance of couplers. These had to be balanced directional couplers. Only in this way one can ensure that the Mach Zehnder interferometers realized starting from those couplers are going to be fully reconfigurable. Couplers were realized according to the geometry presented in Figure 2.3, thus four parameters needs choosing: the curvature radius (R), the coupling length (cl), the coupling distance (cd) and the distance between guides at the input and output of the device (D). This last parameter, though, was actually supposed to be $82\ \mu m$, since our collaborators prepared for the quantum experiment a set up in which the device is coupled to two fiber arrays

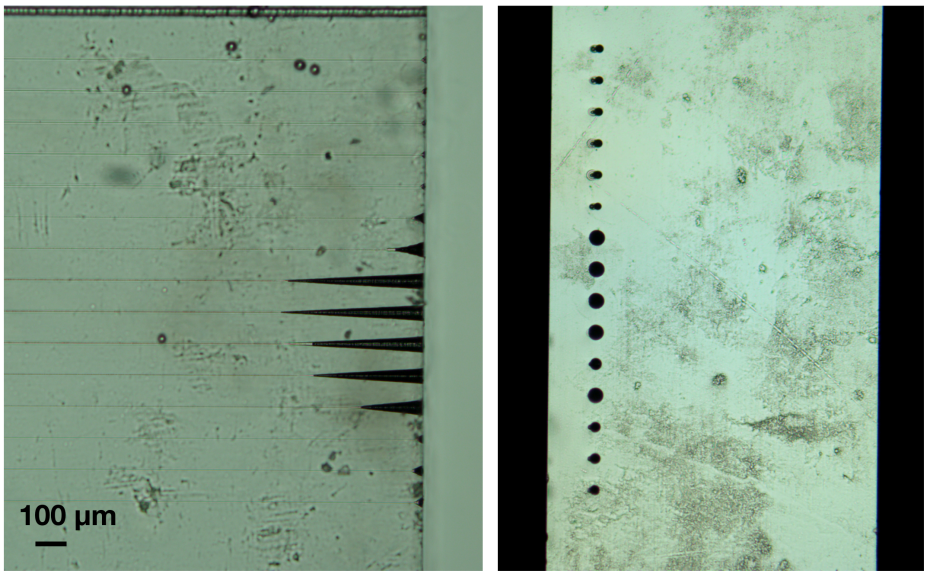

Figure 5.3: *This is a microscope image of the sample after thirty minutes of exposure to HF solution. As mentioned in Chapter 2, one could use femtosecond laser micromachining to define a pattern to be etched in a bulky sample and obtain microchannels in the glass substrate, as it seems about to happen for the central waveguides. In our case, though, we would like to limit as much as possible this effect, since we are interested in an isotropic etching with the goal of reducing the distance between the top surface of the glass and waveguides. The waveguides with the highest transmission (in the picture the ones at the top) were fortunately less sensitive to etching than others, so they are suited for our purposes. Waveguides fabricated at a different depth showed a comparable response to chemical attack.*

with step of exactly $82\ \mu m$.

Bending losses and curvature radius

The necessity of having comparable losses among all the waveguides implied the need of finding a bending radius mild enough to ensure that the third or the forth waveguide (the ones with more bends) have a transmission as close as possible to the one of the straight guide. The milder the curve, the more adiabatic the adaptation of the mode to the guide during the bend and the less relevant the losses.

To find the best compromise between minimal losses and compactness of the device, a set of bending guides with growing R, from $15\ mm$ to $120\ mm$ was fabricated using the fabrication parameters chosen for straight waveguides at $170\ \mu m$ and $220\ \mu m$ of depth. The measured losses are reported in Figure 5.4. In both cases the transmission of the straight waveguide was perfectly comparable with the one of the bend with radius $120\ cm$, whilst for smaller curvature radii (*e.g.* $15\ mm$), bending losses become more and more relevant. This effect is particularly evident for waveguides at $170\ \mu m$, while bending losses for waveguides at $220\ \mu m$ were appreciably lower. This is compatible with the fact that they showed a slightly smaller mode. Therefore we opted for the $220\ \mu m$ depth and $R = 60\ mm$ (with losses slightly smaller than the ones with the same R at $170\ \mu m$) granting negligible curvature losses and a reasonable compactness. Synchronization couplers, so, will be fabricated at $270\ \mu m$. The following table summarizes the chosen parameters for the waveguides of the final device:

Table 5.2: *Chosen fabrication parameters*

Description	Depth	Power	Writing speed	Scans
six photon chip	$220\ \mu m$	$520\ mW$	$40\ mm/s$	6
underlying couplers	$270\ \mu m$	$520\ mW$	$40\ mm/s$	4

Coupling length and coupling distance

The choice of the coupling distance should be driven by the coupling coefficient that takes into account the energy transfer between the two waveguides takes place according to the overlap of the tail of the mode in the first waveguide with the one in the second. In our case the mode diameter was around $10\ \mu m$ and we chose to test, as possible cd, $10\ \mu m$ and $12\ \mu m$. Since the balanced coupler in the first case corresponded to a coupling length of zero, we preferred the second option, which should be more resilient against fluctuations amongst different fabrications. As shown in Figure 5.5, the correct coupling length to have balanced couplers, when $cd = 12\ \mu m$, is $cl = 700\ \mu m$. The same figure also shows how the fabricated waveguides are polarization insensitive, since the output for vertical and horizontal polarization are perfectly similar along the whole period.

Finally, as a benchmark to estimate the stability of the chosen fabrication pa-

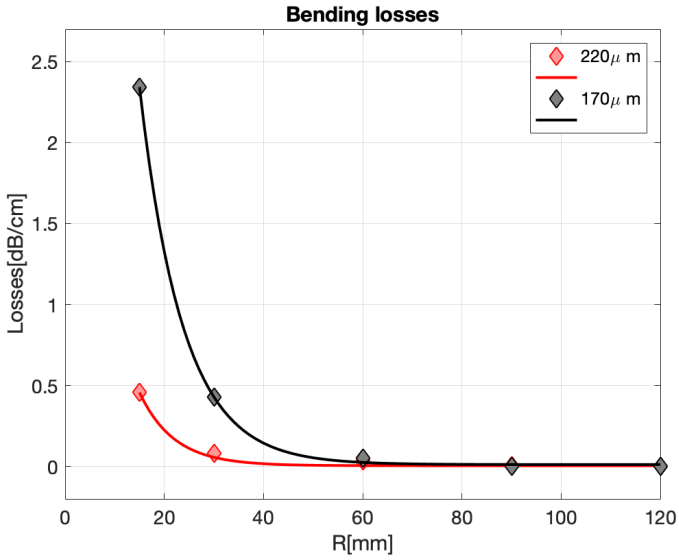

Figure 5.4: *In this Figure the experimental points representing the bending losses observed for various curvature radii at two different depths are presented. The behavior of losses as a function of R can be fitted with a decreasing exponential: Losses $\propto e^{-R/d_0}$, as shown in the plot. Clearly the deeper waveguides are the best performing ones. The points shown are referred to vertically polarized light.*

rameters, a set of Mach Zehnder Interferometers was realized and their phases estimated assuming known the splitting ratio of their coupler (thank to former fabrications). The reconstructed phases showed a variability comparable with the one reported in other integrated circuits realized through FLM.

5.2 High reconfigurability and stability

Having all the parameters necessary to fabricate the passive device, we still had to optimize the recipe of micro-heaters to ensure the wanted reconfigurability.

5.2.1 Thermal phase shifters: a new recipe

As already mentioned, in order to have a reconfigurable optical circuit, we need to fabricate some micro-heaters to locally modify the refractive index. The previous fabrication process was based on the deposition of a single gold thin film on the

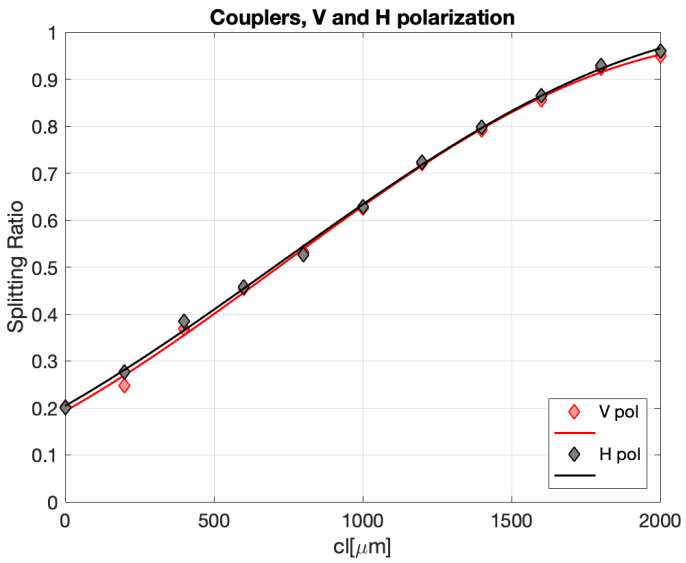

Figure 5.5: *The Figure represents the period of directional couplers with $cd = 12\ \mu m$ for different coupling length. When $cl = 700\ \mu m$ we have balanced couplers. The red and black traces correspond to vertical and horizontal polarization respectively. Being one superimposed on the other we have polarization insensitive devices.*

glass substrate on which the waveguides are written. However, our preliminary characterization demonstrated that this approach does not lead to reliable micro-heaters that meet the requirements of our application. First of all, the value of the resistance changed during the usage being not stable during the heating (and even after thermalization). This can be seen in Figure 5.6 where we observed a drift in R of around 3.5% in just three hours of operation, when injecting a power of $500\ mW$. This phenomenon is probably due to a restructuring of the metal film caused by the high temperature reached during the heating. Such change in the value of resistors is actually a major issue when performing the single photon measurement on an active chip, implying the necessity to recalibrate the system every few hours. Secondly, the adhesion of Gold on the top of the glass substrate is particularly poor, and, for this reason, the layer is extremely fragile from the mechanical point of view, as verified by simple peeling tests.

For this reasons, we started developing a new recipe with the goal to overcome these problems for the micro-heaters fabrication. First of all the adhesion had to be improved. In order to do so one could replace Gold with Chromium, since the

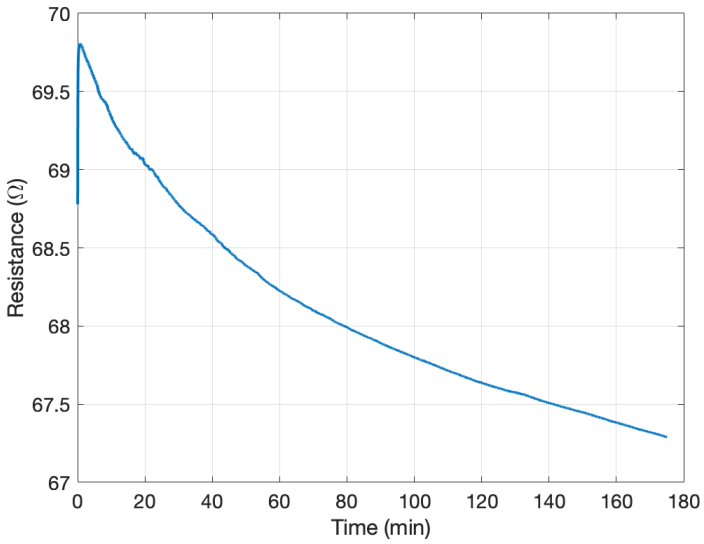

Figure 5.6: *The plot shows the value of the measured resistance as a function of time when dissipating* $500\ mW$*. R drifted of about 3.5%*

adhesion of the latter on glass is quite good. On the other hand, Chromium is extremely prone to oxidation, making critical the connection of the resistors to the external power supply. So we moved to a different recipe, with the addition of a Chromium layer beneath the Gold film (see the insert in Figure 5.9) as an adhesion layer[65], knowing that the sticking of the two metal components is quite good.

We started with a balanced composition, where the thickness of the two materials was comparable. It was observed that, with such a composition, Chromium atoms started to diffuse in the Gold film as soon as the heaters were turned on, compromising the quality of the resistance. Thus the thickness of the Chromium layer was progressively reduced to minimize this side effect. More specifically, we decided to use a $3\ nm$ layer of Chromium and a $100\ nm$ film of Gold on it. This recipe guarantees good adhesion on glass, high mechanical stability and prevents the interdiffusion of Chromium atoms inside the Gold film during the heating, a side effect that would introduce a further cause of instability on the heater operation[66]. Finally, it is worth noting that the new design is electrically equivalent to the former one, since the very different resistivity of the two materials (more than an order of magnitude) and the very different thickness of the two films make sure that the current will flow ”only” in the Gold layer.

Nevertheless, the issue concerning operating stability still had to be faced, by virtue of the fact that with this recipe R still drifted. For this reason we introduced an annealing step of the film with the aim of having, before the usage, all the restructuring induced by the high annealing temperature. The final recipe prescribes a rising ramp at $10°$C/min until $400 - 500°$C (the process is relatively insensitive to this temperature) followed by a plateau of around 30 minutes at that temperature. It is worth pointing out that, being this temperature smaller than the strain point of the glass substrate ($669°$C), this process has no effect on the optical properties of the waveguides. After the thermal recovery overnight down to room temperature, a high stability over time is achieved, as depicted in Figure 5.7. Now, even after 8 hours of operation at $600\ mW$, very small fluctuations were observed in the value of R (around 0.05%).

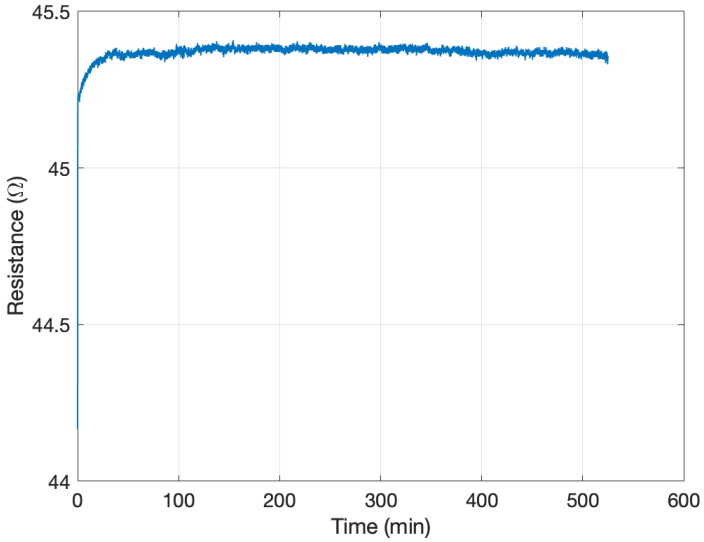

Figure 5.7: *Here can be seen how, at variance with Figure 5.6, the heaters realized with the final recipe were stable in time: when injecting a fixed power, once they have reached a stable temperature, R remains constant in time.*

We also tested the performance at high dissipated power of the new resistors, in order to set an upper bond for a safe operation, namely without inducing permanent modifications or damages to the device. As shown in Figure 5.8 the heater can sustain a power dissipation up to $3.6\ W$, which is about four times larger than the breaking point achieved with the former recipe, for resistors of equal dimen-

sions. Furthermore, the reliability of the micro-heaters was tested not only with an IV characterization, but also with stability measurements that demonstrated a correct operation up to many hours with similar dissipated powers.

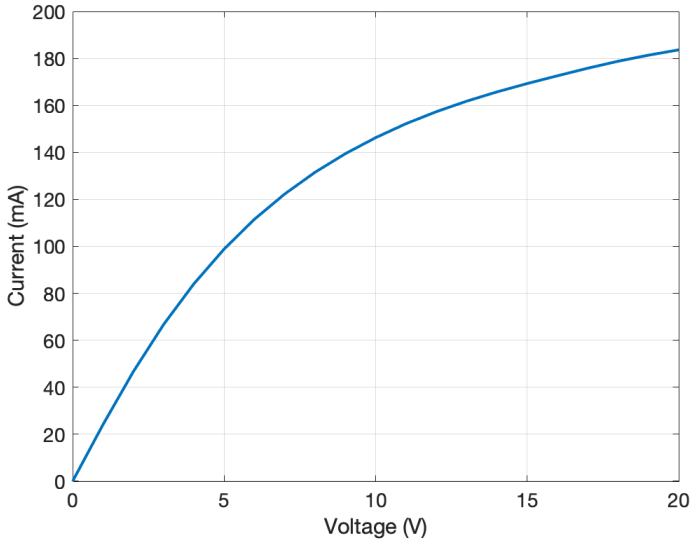

Figure 5.8: *The plot shows the current - voltage plot for the new heaters. Resistors are clearly non-linear, because of temperature effects, but they can dissipate powers much higher than before.*

It is clear, as touched in Chapter 2, that the efficiency of a thermal phase shifter in a Mach Zehnder Interferometer is reduced by the presence of thermal cross-talk between the two arms. Indeed, we would like to heat one waveguide only, but instead the refractive index of the second arm is going to be influenced by the power dissipation as well. This cross-talk effect will affect even different phases in case of more complex circuits.

To reduce this problem we decided to remove the metal conductive bridge between the two waveguides, in order to increase the thermal insulation between the heater and the adjacent waveguide. So that, with reference to Figure 5.9, R_{cross} is maximized.

Doing so, in a MZI with arms at a distance of $127\ \mu m$, we were able to reduce the power dissipation that induces a 2π phase shift of around 15%, from $0.49\ W$ to $0.42\ W$. Results are shown in Figure 5.10 while Figure 5.11 shows a microscope image of the trial chip. To get a further improvement in the cross-talk reduction, one

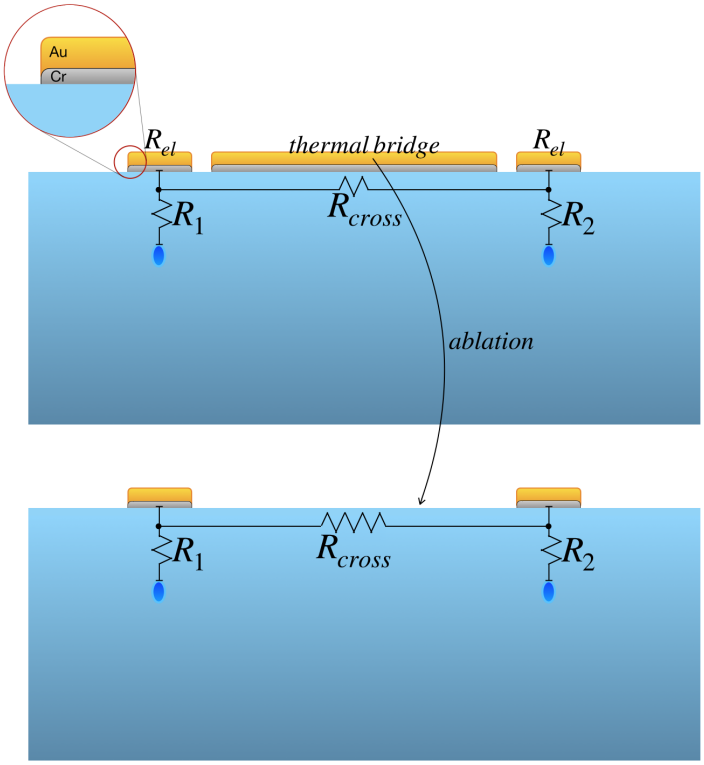

Figure 5.9: *This image shows the schematic of the cross section of a device on which electrodes have been fabricated. In the upper panel the metal in between the two electrical resistors was not ablated, in the bottom one it was. Thus, we reduce thermal cross-talk between the waveguides, removing the component due to thermal conduction of the metallic layer.*

could dig some trenches between the two waveguides, as proposed by Chaboyer *et al.*[67]. This kind of solution, though, is not easily implementable in our fabrication process, so it will require further studies.

5.3 Geometry of the electrodes

The tests on the heaters described above were performed on resistors whose length was $5\ mm$. Such dimension is the standard one we use for the evaluation of the performance of such micro-heaters. Thus, typically, the length of the straight part within the two couplers in a MZI is $5\ mm$ as well, to make sure that the whole

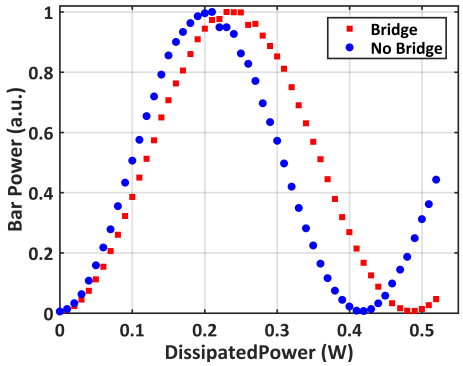

Figure 5.10: *This plot presents a comparison between the period of oscillation of the phase in a MZI tuned by a micro-heater in the presence (blue dots) and absence of thermal bridge between the waveguides (red dots). Removing the metallic layer between the two guides allows to get a reduction of about the 15% of the period.*

thermally induced phase shift is going to take place in this straight region.

In our case, though, because of the constraint concerning losses, we wanted the overall length of the device to be as small as possible, so we couldn't have a straight portion that long. We opted for the following parameters: bending radius $R = 60\ mm$, coupling length $cl = 700\ \mu m$, coupling distance $cd = 12 \mu m$, straight guide in the MZI of $1\ mm$. The expected total length of the device was around $4.6\ cm$ which should ensure losses within specifications.

From the electrical point of view we did not want to fabricate too short heaters, in order to avoid operation temperatures excessively high. The reason for this stems from the Black equation. It provides us with an estimate for the mean time to failure ($MTTF$) of the resistance due to electromigration

$$MTTF = \frac{A}{j^n} exp\left\{\frac{Q}{kT}\right\}$$

where A is a constant, j is the current density, n is a model parameter, k is the Boltzmann constant, Q is an activation energy and T is the absolute temperature. This tells us that the higher the temperature of operation, the more probable is that the resistor is going to break and that the dependence on temperature of $MTTF$, being exponential, is actually much stronger than the one on the current density.

So, as a first attempt, we decided to fabricate bending heaters, extending the interaction region onto the bending guide too and getting relatively close to the

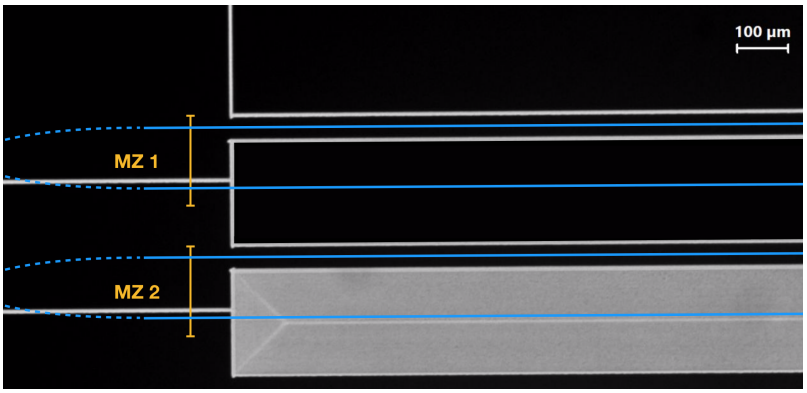

Figure 5.11: *The microscope image shows the difference between the case in which the metallic bridge between waveguides is ablated (MZ2) and when it is not (MZ1). The position of waveguides is highlighted by the light blue trace.*

coupling region. This kind of solution had already be tested. This geometry provides a lower efficiency with respect to the one of straight resistors, since the distance between the heater and the guide we do not want to heat is, on average, smaller than it would be in the case of the straight heater[60]. In turn they allow to have a very compact device, minimizing propagation losses. Figure 5.12 shows the final geometry of the electrodes pattern. With respect to the schematic of Figure 4.3, a sixth electrode (the circled one) was added to have a fine tuning of possible phase accumulated in the "ring" delimited by MZ 2 and 5. We decided to realize a pattern allowing us to keep all the electrodes on the same side of the chip, so that, if necessary, we could contact two devices on the same sample.

The standard procedure for defining the electrodes pattern is based on the ablation of the metallic layer in a fabrication different from the one of waveguides inscription. The "trick" used to obtain a good alignment of electrodes with respect to the former fabrication consisted in the realization of some markers on the glass surface when fabricating the waveguides. These will be used as a reference for the second fabrication. The etching process, though, degrades the quality of these markers whose width passes from a few micrometers to around $100\ \mu m$. This is actually a critical point of the etching process. It leads to a relatively high uncertainty in the alignment of the heaters circuit. Having several markers one reaches a precision in the order of about $10 - 15\ \mu m$, to be compared to the one of $1 - 5\ \mu m$ of a non etched sample. Markers before and after etching are shown in Figure 5.13.

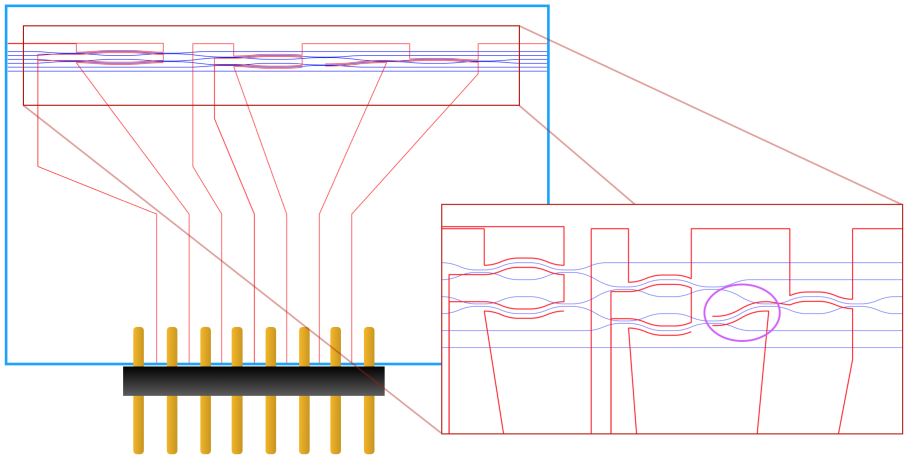

Figure 5.12: *This Figure shows the geometry of micro-heaters. In order to have resistors of length comparable with the one of the micro-heaters used to characterize the new recipe we preferred to design bending electrodes. They extend over the bending guide and approach the interaction region of couplers. This implies that we are going to lose some efficiency in the tuning, but permits to have relatively long phase shifters (which we knew were reliable from the electrical point of view) on a compact device. Beside the electrodes pattern, we also ablated the thermal bridge as explained in former section.*

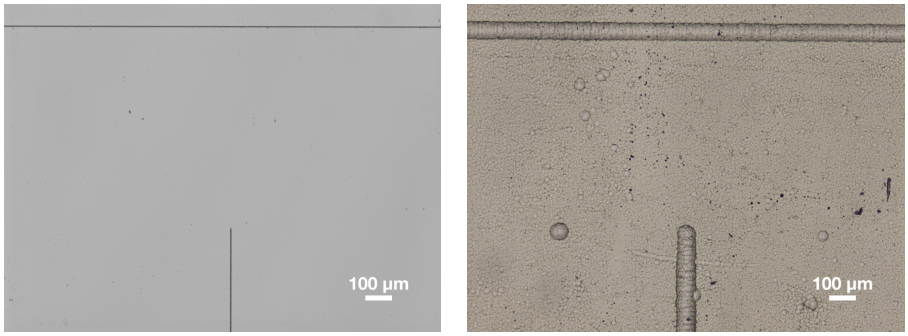

Figure 5.13: *These are microscope images of the same superficial ablation before and after etching. These ablations are used as reference for the alignment of the sample when fabricating the electrodes to match the position of the waveguides.*

Chapter 6

Classical light characterization

In this last Chapter we deal with the experimental results obtained on a first realization of the final device. In Section 6.1 the performance of the passive device are presented, while Section 6.2 shows the results concerning reconfigurability. Finally in Section 6.3 an alternative design for the electrodes pattern, which should allow to get a higher efficiency in tuning the various phases, is proposed.

6.1 Passive device characterization

The final device, whose schematic is reported in Figure 6.1 for convenience, was characterized using a single mode fiber to launch light in one of the waveguide and collecting the output of all waveguides at ones with a fiber array. This allowed us to be sure that the output signals were actually being wholly collected. Thus we were sure to estimate correctly both the losses and the splitting ratios of the various MZI.

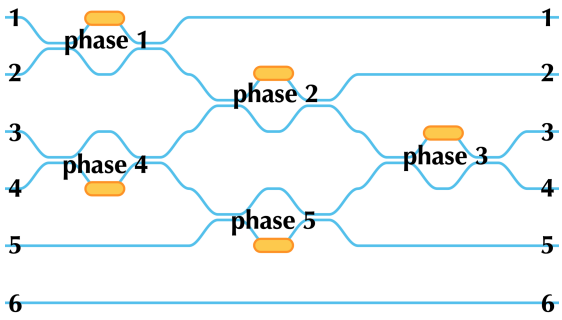

Figure 6.1: *This schematic of the final device is re-proposed here for convenience, since in the following pages we will often refer to various phases and ports.*

For what regards propagation losses we obtained again the good results found for the straight waveguides at the beginning of the characterization of the process, i.e. propagation losses of $0.29\ dB/cm$. Considering also other contributions (Fresnel and coupling losses), we observed an overall transmission of around 61% for the straight guide and 59% for the guide with more bends. The alignment of the chip with the excitation and collection optics was extremely precise, thank to the use of the couple of hexapods mentioned before. Actually we used no index matching, so in principle one could enhance slightly the overall transmission getting rid of Fresnel losses.

The distribution of the output power was perfectly in line with the expectation for all waveguides. This proves the good stability of fabrication parameters. In particular this means that variability in the splitting ratio of couplers and spare contribution to phases introduced by fluctuations in the fabrication process were basically negligible. This can be appreciated in the following Figures where a set of histograms present the measured output compared with the expected one, i.e. the output one would get with perfectly balanced couplers and no unwanted phase introduced by any of the Mach Zehnder Interferometers.

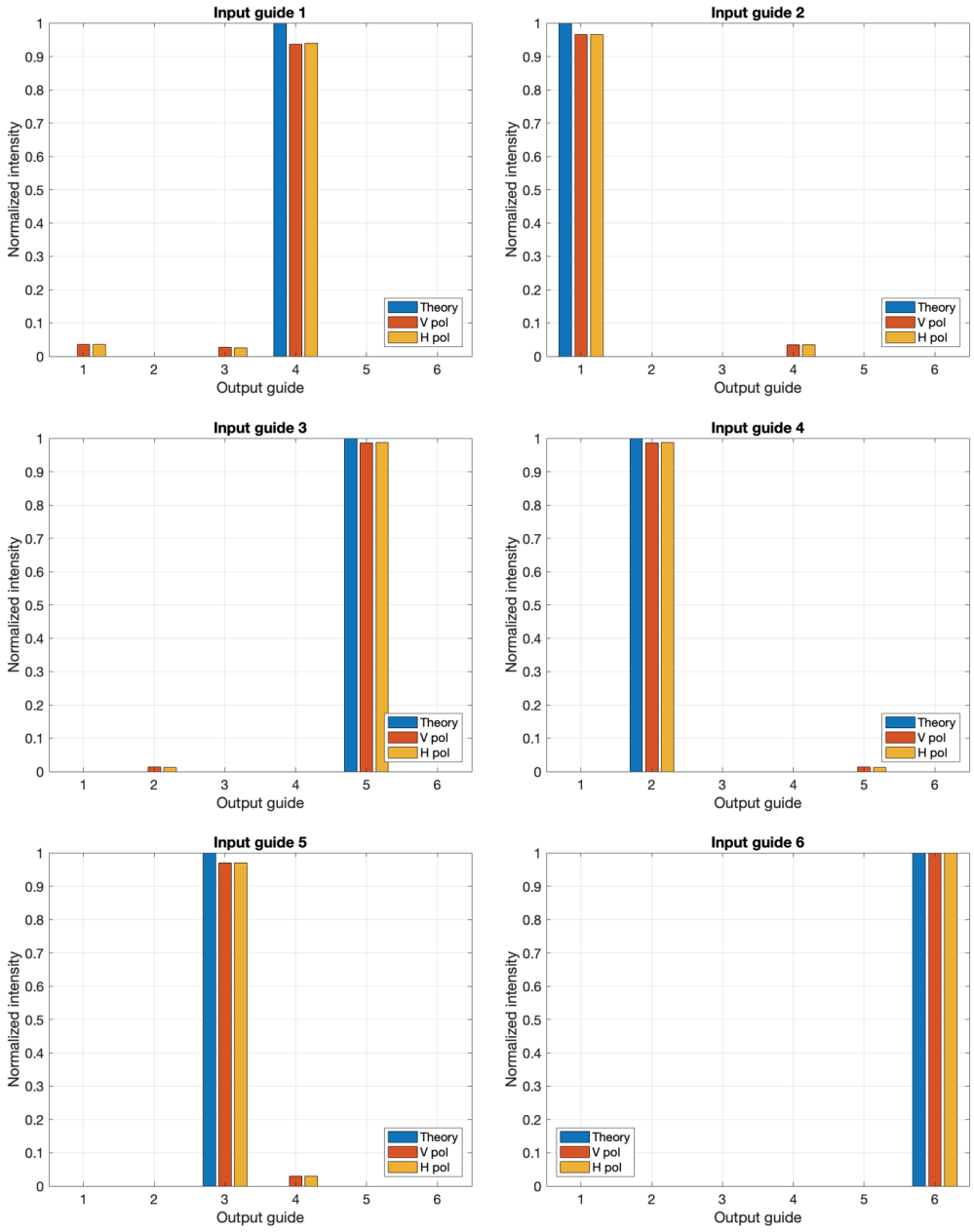

Figure 6.2: *These histograms show the output pattern as light was coupled to one input. We only report a comparison between the theoretical expectation (assuming perfectly balanced couplers and zero phases), and the cases of horizontal and vertical polarization.*

A quantitative estimate of the performance in terms of correctness of these distribution is the value of the so called Fidelity $\mathcal{F}$, measuring how similar the experimental distribution is with respect to the theoretical one. It is defined through

$$\mathcal{F} = \frac{\sum_j \sqrt{D_j D'_j}}{\sum_j D_j \sum_j D'_j}$$

being the D_js the theoretical distributions and D'_j the experimental ones. Neglecting the trivial case of the sixth input (which is a straight guide) we had fidelities between 93.7%, for the output distribution associated to the first input, and 98.6%, for the third and the fourth one.

The splitting ratios were directly accessible from the distribution of the output power in four cases out of five. For the only remaining MZ, i.e. the fourth, it could be retrieved combining the output distributions and the other estimated splitting ratios. Just to make some examples, possible ways to retrieve the splitting ratio are:

- When injecting light in the first input, the splitting ratio of MZ1, SR_1, can be found as:
$$SR_1 = \frac{P_1}{P_2 + P_3 + P_4}$$
being P_i the power at the i^{th} output port. Analogously,
$$SR_3 = \frac{P_3}{P_4}$$
$$SR_2 = \frac{P_2}{P_3 + P_4}$$
- Coupling light into the fifth input, instead, we have:
$$SR_5 = \frac{P_5}{P_3 + P_4}$$

Also other combinations led to the same results. Concerning the fourth MZ, instead, it could be demonstrated that, when coupling light in the third input we have:

$$SR_4 = \frac{(1 - R_5)P_2}{(1 - R_2)P_5 + (1 - R_5)P_2}$$

or, equivalently, when launching a signal in the fourth waveguide:

$$SR_4 = \frac{(1 - R_2)P_5}{(1 - R_5)P_2 + (1 - R_2)P_5}$$

Alternatively, SR_4 could have been measured in a way identical to the one used for SR_3, but coupling light from the second output port.

The reasoning described above holds by virtue of the fact that we had already measured the losses of all waveguides, and so could ascribe the output power distribution to phase effects only. An objection that could be moved to this procedure is the fact that possible inhomogeneities and defects of couplers were assumed to be completely negligible. This assumption, though, will be justified by the results presented in the following Section. Indeed, once that phase shifters were fabricated, we were able to verify that a complete power transfer is achieved in all cases, implying that all couplers must be balanced.

The splitting ratio of a Mach Zehnder fully characterizes the device itself. Thus, from these splitting ratio, we could give an estimate of the unwanted phase accumulated due to unbalanced paths. The device on the top of which electrodes were fabricated showed the following intrinsic phases (in radiants):

$$\phi_1 = 0.36,\ \phi_2 = 0,\ \phi_3 = 0.29,\ \phi_4 = 0,\ \phi_5 = 0$$

These values are going to be tuned using thermal phase shifters, so to have a fully reconfigurable device as described in the previous Chapters.

6.2 Active device characterization

At this point we move to the characterization of phase shifters. For this experiment the sample was mounted onto a custom heatsink made in aluminum. The arrangement is shown in Figure 6.3. The goal of such a heatsink was more making sure that the temperature of the sample bottom face was uniform than actually ensuring a high heat dissipation.

We measured the resistance of the various heaters and found the following values:

$$R_1 = 64\ \Omega,\ R_2 = 49\ \Omega,\ R_3 = 55\ \Omega,\ R_4 = 61\ \Omega,\ R_5 = 48\ \Omega,\ R_6 = 42\ \Omega$$

The pins of the various electrodes were connected to a Power supply (KEITHLEY 2231A-30-3) letting us impose a fixed voltage drop across the resistors.

These measurements aimed at reconstructing the matrix A of the coefficients linking the injected Power to the induced phases. These coefficients are basically the α_i of Equation 2.7 and represent the control parameter of each heater on each phase. Suppose that, turning on just the i^{th} heater, to get a full period of the j^{th}

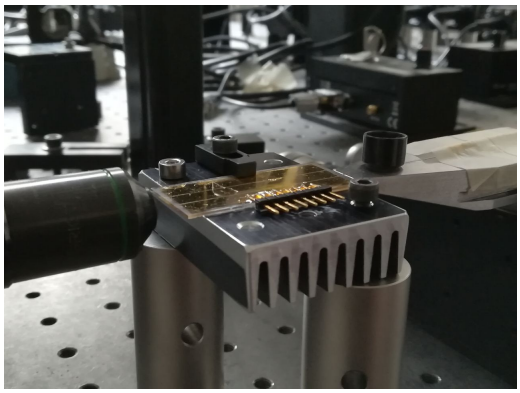

Figure 6.3: *This picture shows the final chip mounted on an aluminum heatsink. This arrangement ensured that the bottom of the sample was kept at a constant temperature. A good thermal conductivity between the glass substrate and aluminum was granted by a thin layer of thermal grease.*

phase you need to inject a Power P_j, then $\alpha_{ij} = 2\pi/P_{j,\,at\,\phi=2\pi}$. For now let us neglect the sixth heater, the one we added with respect to the original design, and concentrate on the other control parameters. Since we are left with five resistors and five phases, A is going to be a squared matrix.

From matrix A one can find the right power distribution to obtain a certain phase configuration according to the following Equation (that neglects for brevity the initial phases) :

$$\begin{pmatrix} \phi_1 \\ \phi_2 \\ \phi_3 \\ \phi_4 \\ \phi_5 \end{pmatrix} = \begin{pmatrix} \alpha_{11} & \alpha_{12} & \alpha_{13} & \alpha_{14} & \alpha_{15} \\ \alpha_{21} & \alpha_{22} & \alpha_{23} & \alpha_{24} & \alpha_{25} \\ \alpha_{31} & \alpha_{32} & \alpha_{33} & \alpha_{34} & \alpha_{35} \\ \alpha_{41} & \alpha_{42} & \alpha_{43} & \alpha_{44} & \alpha_{45} \\ \alpha_{51} & \alpha_{52} & \alpha_{53} & \alpha_{54} & \alpha_{55} \end{pmatrix} \begin{pmatrix} P_1 \\ P_2 \\ P_3 \\ P_4 \\ P_5 \end{pmatrix} \tag{6.1}$$

From the fabrications dedicated to the study of the new recipe for the metallic film, we knew that having a MZI working with straight waveguides at distance of $127\ \mu m$ and at a wavelength of $780\ \mu m$, the power to be injected in a $5\ mm$ long electrode to have a full period is around $T_{2\pi} = 450\ mW$ (see also Figure 5.10). In our final device, though, we were working at 1546nm, so, from equation 2.6 we expect an increase of a factor 2. Furthermore we are dealing with bended electrodes so, again with reference the same equation, the average distance between guides will be even smaller than the $82\ \mu m$ separating the waveguides when they are straight.

Considering also that after the etching we had the guides as far as $25\mu m$ from the top surface (instead of $30\ \mu m$ as in the trial fabrications) , we were expecting a period of about $1\ W$ to control the i^{th} phase with the i^{th} heater. This is higher than the period of the micro-heaters described in Chapter 4, but still far from the breaking point of the metallic layer.

To make the measurements we could control the voltage drop at the pins of the resistors. Our micro-heaters are strongly nonlinear with temperature, as any gold resistance. This means that as they operate at a temperature larger than T_{room}, their R is larger than the one reported above.

We started coupling light to the first input port and applying a sweep from $0V$ to V_{max} to R_1. V_{max} was extracted from the relation $P_{th} = 1\ W = V_{max}^2/R_i$. Since the value of all the resistors increases during the usage because of temperature effects, the power actually dissipated P_{diss} is going to be smaller than $1\ W$. Figure 6.4 shows the power measured at the first output. To build the matrix collecting the control parameters we will make reference to the power actually dissipated, obtained as $P_{diss} = VI$. Reasoning in terms of P_{diss} we retrieve a sinusoidal behavior from which we can immediately extract the period necessary to have a full period and thus $\alpha = 2\pi/T_{2\pi}$.

The red dots in Figure 6.4 could already be fitted to extract the first α: α_{11}, telling us how good is the control of the first heater on ϕ_1, but we preferred to see the full period. The measure was repeated increasing the upper limit of the sweep and collecting all the outputs: see Figure 6.5. The result was compatible with what we were expecting, as can be deduced from Figure 6.6. From a sinusoidal fit we got $T_{2\pi}^{R_1 \to \phi_1} = 1.37\ W$, a bit larger than expected but still acceptable and corresponding to a control parameter $\alpha_{11} = 4.6\ rad/W$.

At this point we kept coupling light to the device from input 1, but turned off R_1 and made a Voltage sweep across R_4, to estimate the cross-talk between the fourth heater and the first phase. The power distribution is shown in Figure 6.7. This time the period is: $T_{2\pi}^{R_4 \to \phi_1} = 2.57\ W$, i.e. about a factor 2 larger than $T_{2\pi}^{R_1 \to \phi_1}$ which is a good result, telling us that we will be able to tune ϕ_1 using R_1 even when some power is being dissipated by R_4.

Analogous measurements were performed for all couples heater-phase. From

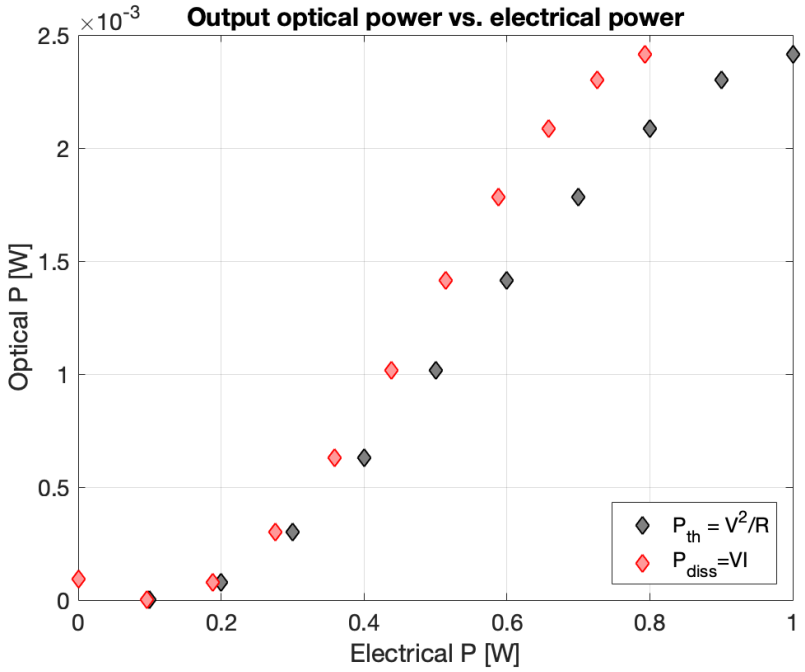

Figure 6.4: *This plot shows the output power at the first output as a funciton of the injected electrical power. The correct curve is the one of red spots which is referred to* $P_{diss} = VI$*, the black one refers to* $P_th = V^2/R(T_{room})$ *which would be reasonable if the temperature dependence of resistivity were negligible. The higher the power, the higher the temperature, the more evident this effect.*

the output distribution we reconstructed the following matrix (values in rad/W):

$$A = \begin{pmatrix} 4.6 & 0 & 0 & -2.01 & 0 \\ 0 & 6.56 & 0 & 0 & -2.52 \\ 0 & 0 & 4.93 & 0 & 0 \\ -2.45 & 0 & 0 & 2.79 & 0 \\ 0 & -3.21 & 0 & 0 & 4.11 \end{pmatrix} \tag{6.2}$$

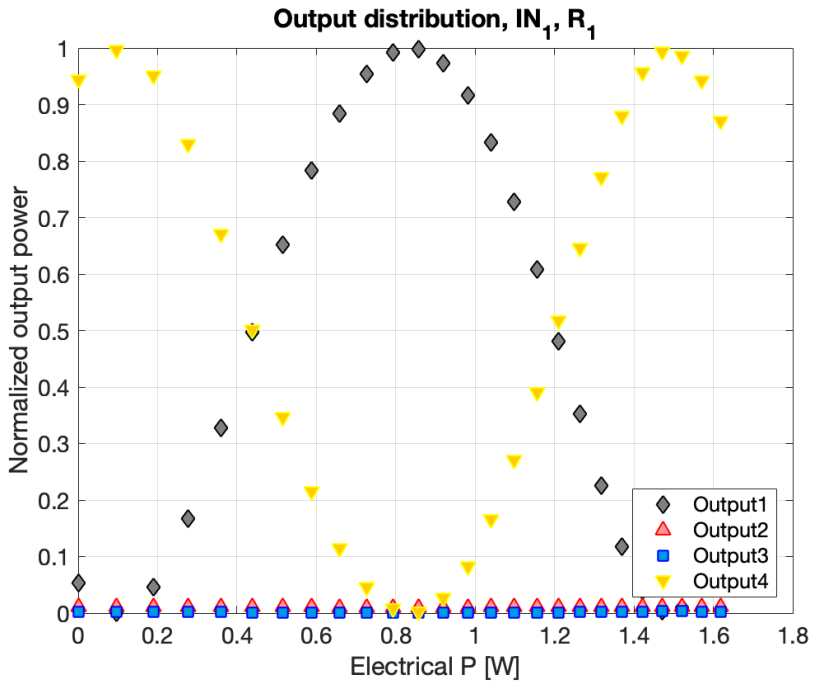

Figure 6.5: *The plot shows the normalized output power distribution on all the waveguides related to the first input. By virtue of the configuration of phases 2 and 3 no effect can be appreciated on the second and the third output. A full power transfer can be appreciated between the first and the fourth one.*

corresponding to the periods (in W) shown in $\mathcal{P}$:

$$\mathcal{P} = \begin{pmatrix} 1.27 & 0 & 0 & 3.13 & 0 \\ 0 & 0.96 & 0 & 0 & 2.5 \\ 0 & 0 & 1.27 & 0 & 0 \\ 2.57 & 0 & 0 & 2.25 & 0 \\ 0 & 1.96 & 0 & 0 & 1.53 \end{pmatrix} \tag{6.3}$$

This result is acceptable for all heaters but the fourth. As a matter of fact α_{41} and α_{44} are too close to each other and this does not allow one to choose ϕ_4 independently from ϕ_1. Indeed solving the system stemming from 6.1 and considering $\phi_1 = \pi$ and $\phi_4 = \pi$ we get $P_1 = 1.9\ W$ and $P_4 = 2.8\ W$ which starts to be critical considering that the quantum measurements to be performed on the chip are quasi-static and will last several weeks.

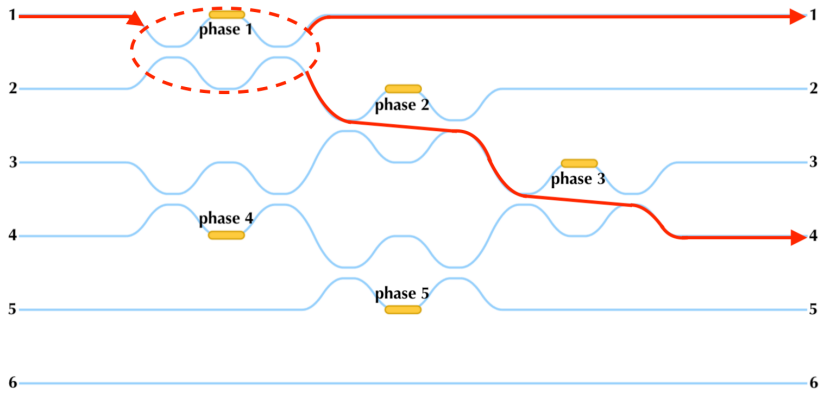

Figure 6.6: *This schematic shows the path followed by photons given the values of ϕ_2 and ϕ_3 when they are not tuned. The output of Figure 6.5 is perfectly compatible with this scheme, and the power transfer from output four to one and viceversa is due to the tuning of $R1$.*

To find the origin of these poor performance we verified the alignment of heaters with respect to waveguides with a microscope. It was found out that, due to a slight misalignment both in the light propagation direction and in the tilting, the fourth resistor fallen almost in between the two waveguides of its MZ. Luckily in the other cases the combination of translation and rotation with respect to the optimum was not as critical as in this.

This misalignment was actually of just a few micrometers and we expected it to be negligible. The reason why it was so critical comes from the compactness of the device that brought to the decision of designing bending electrodes and in the fact that waveguides are closer than in other analogous chips. The point is that we don't expect to obtain a better alignment than this, given the intrinsic uncertainty stemming from the dimension of markers after the etching process (see the former Chapter). Thus, we decided to exploit the misaligned heaters as a new reference to re-fabricate in a free portion of metal the fourth electrode.

The design is shown in Figure 6.8. In this way the fourth electrode will end up being slightly misaligned with respect to the ideal situation, but still in a better position than before. To fit the new resistor in the available space it was necessary to choose a length smaller of about the 20% than usual, i.e. $3.9\ mm$. After the fabrication, the new resistance was $R'_4 = 36\ \Omega$.

First of all we measured again the α coefficients. Obviously all the ones related

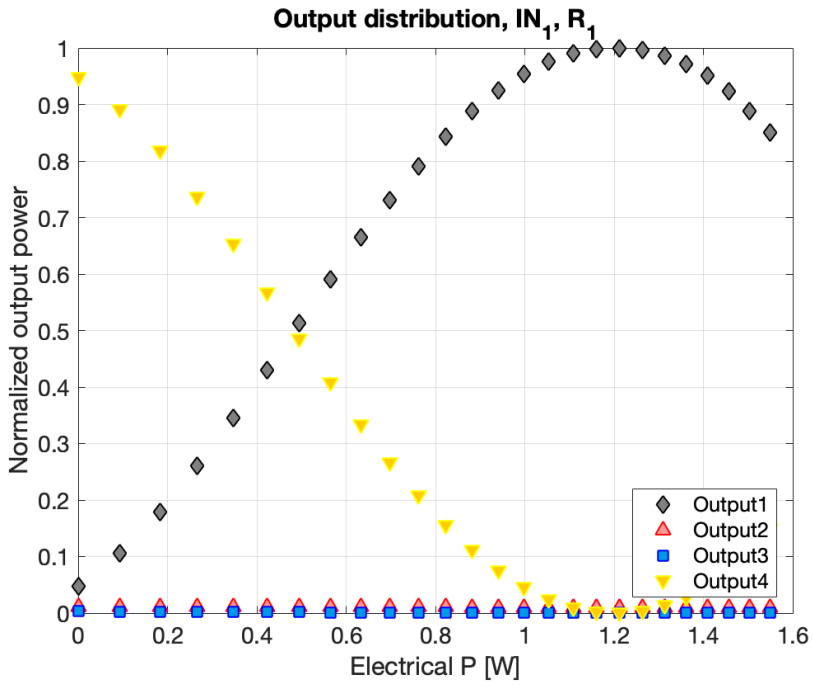

Figure 6.7: *The plot shows the normalized output power distribution on all the waveguides related to the first input. This time, though, instead of injecting power in R_1 we turned on R_4 to measure the cross-talk term: this oscillation comes from the effect of heater 4 on ϕ_1 The period is almost doubled with respect to the case of Figure 6.5.*

to the other electrodes hadn't changed. The new α_{41} and α_{44} are:

$$\alpha_{41} = -2.57\ rad/W,\ \alpha_{44} = 6.14\ rad/W$$

So in terms of control we got a very good result. We could also test this shorter resistor in terms of long term reliability. We performed tests similar to the ones shown in the former Section 5.2.1 and results identical to the ones of longer resistors. We concluded that the new recipe for the metallic layer can successfully be used to fabricate shorter heaters.

So the reprocessing had worked as we hoped. At this point the less efficient heater was the fifth one. The geometry of electrodes could allow the same procedure implemented on R_4. To decide whether re-fabricate the fifth electrode or not we considered that it shows a high cross-talk with ϕ_2 and computed P_2 and P_5 needed to induce a π shift both on ϕ_2 and ϕ_5: we got $P_2 = 1.10\ W$ and $P_5 = 1.63\ W$.

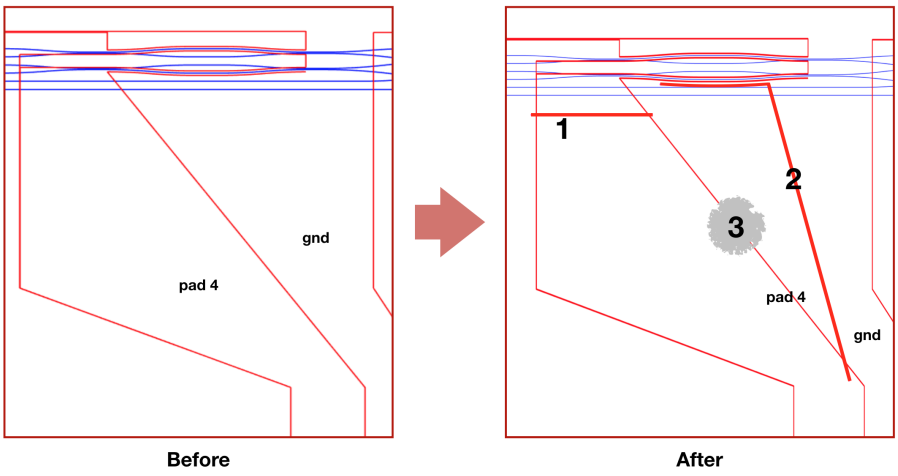

Figure 6.8: *In the image is presented the pattern of electrodes before and after the re-fabrication. In particular, we disconnected through ablation (1) the original heater, fabricated a new resistor with ablation (2), and connectorized it with a drop of conductive glue (3).*

These are not as low as they could be, but are still accessible. So we didn't make any other re-fabrication.

Now let us go back to the sixth resistor. Its position is such that we cannot trivially access ϕ_6 from the output Power distribution. It induces a phase shift on the electric field entering the third MZ, and that phase contribution remains untouched at the output since, accordingly to Equation 2.5,

$$\begin{pmatrix} |E_{out,1}|e^{i\phi_1} \\ |E_{out,2}|e^{i\phi_1} \end{pmatrix} = e^{i\frac{\Delta\phi}{2}} \begin{pmatrix} Re^{i\frac{\Delta\phi}{2}} - Te^{-i\frac{\Delta\phi}{2}} & 2i\sqrt{RT}\cos\left(\frac{\Delta\phi}{2}\right) \\ 2i\sqrt{RT}\cos\left(\frac{\Delta\phi}{2}\right) & Re^{-i\frac{\Delta\phi}{2}} - Te^{i\frac{\Delta\phi}{2}} \end{pmatrix} \begin{pmatrix} |E_{in,1}|e^{i\phi_1} \\ |E_{in,2}|e^{i\phi_1} \end{pmatrix} \tag{6.4}$$

The value of α_{66} could be extracted from an interferential measurement. Knowing that our collaborators in Vienna will re-calibrate the control parameters (since they are going to use a different controller and to implement a Current control rather than a Voltage control as we did) we didn't characterize it for now. What we did was verifying that $\alpha_{i6} = 0 \; \forall i = 1, ..., 5$, so we know the sixth heater is not introducing an unwanted phase shift on other phases. Furthermore, checking by visual inspection with a microscope the alignment of the resistor with respect to

the waveguide was good. Therefore it's reasonable to assume that the sixth heater will have performance comparable with the others.

In general the conclusion we reached is that obtaining an optimal alignment after having etched the sample is not trivial. For this reason, specially in cases of relatively compact devices as the one object of this work, one should always fabricate more electrodes than the number of phases to be controlled arranging in a clever way these extra heaters. The next section shows a possible interpretation of this idea that could be implemented on a replica of the chip.

6.3 An alternative design

To justify why the addition of extra electrodes could improve the performance of the device, reducing the control effort, one can consider a device having two MZI disposed as in Figure 6.9. In terms of the reference frame for phases proposed in the schematic, R_1 will induce a positive phase shift on ϕ_1 and a negative one on ϕ_2, and viceversa for R_2. On the other hand, to explore different phase configuration on an interval of length π, this disposition allows only to explore the region $\phi_1 \times \phi_2 = [0, \pi] \times [0, \pi]$. The addition of R_3 allows to tune the phases in the region $\phi_1 \times \phi_2 = [-\pi/2, \pi/2] \times [-\pi/2, \pi/2]$ reducing for sure the control effort for all the cases in which we are setting both ϕ_1 and $\phi_2 < 0$ (intuitively because now only one resistor will be turned on).

From a quantitative point of view, taking inspiration from the measured α in our device, we could hypothesize the following parameters for matrix A in this case:

$$A = \begin{pmatrix} 6 & -2.5 & -3 \\ 3.5 & 6 & -3 \end{pmatrix} \tag{6.5}$$

In this condition we calculated the power needed to obtain a set of configuration on an interval of length 2π activating all three heaters or using only R_1 and R_2. The result of this simulation are presented in Figure 6.10. With reference to the plot: in the case of three heaters, the first nine points are obtained keeping $\phi_1 = -\pi$ and letting ϕ_2 span from $-\pi$ to π. Then, from case 10 to case 18, ϕ_1 was kept fixed at $-\frac{3}{4}\pi$ and ϕ_2 varied between $-\pi$ and π, and so on till the last group where ϕ_1 was fixed to π. The case of two heaters followed an identical scheme, apart from the fact that the angles ranged from 0 to 2π. In the latter case the average power consumption was of $1.80\ W$, while in the presence of the third electrode

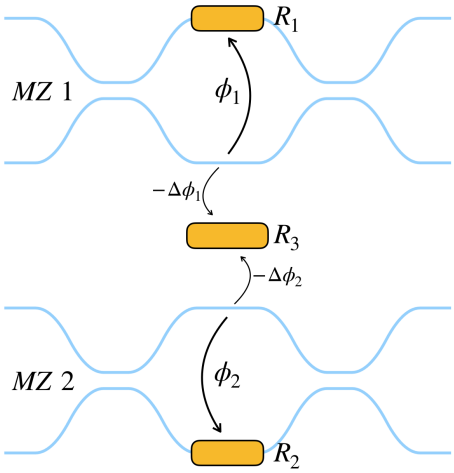

Figure 6.9: *The addition of a third electrode between the two MZI allows to induce a negative phase shift (with respect to the reference frame proposed in the Figure) and thus to span the same range of configuration of a two electrodes configuration with a smaller power consumptions.*

it was reduced to $1.04\ W$. Moreover the maximum power consumption in case of a three electrodes scheme never exceeded $2\ W$. For the other geometry, even for both phases not larger than π, it reached $2.5\ W$.

The algorithm used for the two resistors case was the optimal one, while the solution for the three heaters arrangement is not always the optimal (since the system is underdetermined and the problem is periodic). So the power saving could be even more substantial.

As briefly touched, we wanted to have the possibility to connectorize more than one device per sample. Thus the number of pads per device, given the dimensions of the sample itself, was too high to implement a solution of this kind since the beginning. Giving up the possibility of realizing the electrodes on more than one device (which is reasonable after the validation of the good performance of the one we finished) and having the possibility to connectorize a single device exploiting both sides of the sample, this approach could be followed on a second prototype of our chip.

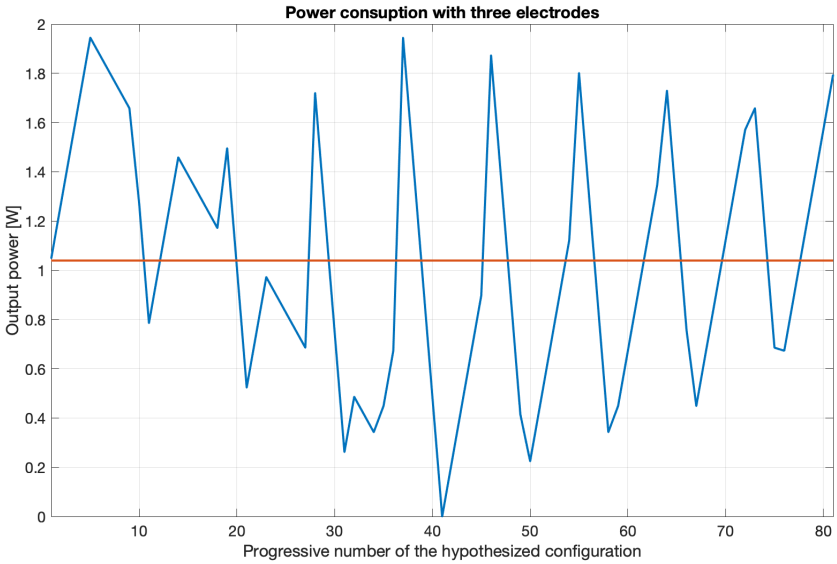

(a) Power consuption with three electrodes

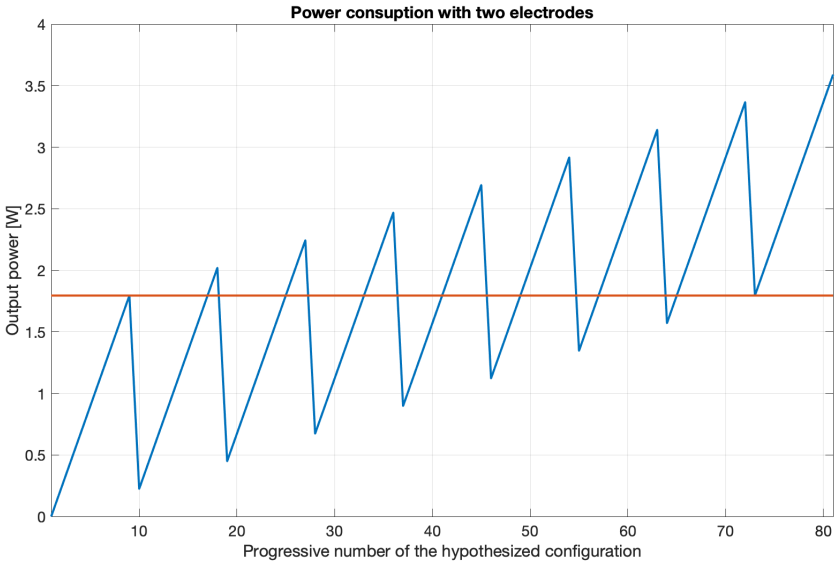

(b) Power consuption with two electrodes

Figure 6.10: *Both cases explore a set of phases of magnitude* $[2\pi \times 2\pi]$*, so they share the same capability of reconfigurability. The presence of the third electrodes reduces the average power consumption (indicated by the red line) from* $1.80\ W$ *to* $1.04\ W$*.*

Conclusions

In this work the realization of a reconfigurable integrated optical circuit has been reported. The device was realized with the technique of FLM. After the optimization of fabrication parameters we obtained polarization insensitive waveguides supporting a single mode and showing propagation losses smaller than $0.3\ dB/cm$ for photons at a wavelength of $1546\ nm$. To get such a transmission it was necessary to use a fabrication depth of $220\ \mu m$, which *per se* would have been incompatible with the requirement of reconfigurability. Thus a new fabrication step was introduced: an isotropic etching of the sample allowed us to disentangle the fabrication depth and the final distance between the glass top surface and waveguides, which was reduced to $30\ \mu m$. The full reconfigurability of phases has been achieved through thermal phase shifters fabricated onto the glass substrate after the deposition of two metallic layers (Chromium and Gold). To make sure that the splitting ratio of all the various Mach Zehnder Interferometers were fully tunable between zero and one, we used fabrication parameters leading to balanced couplers.

A classical characterization of the chip showed a transmission around the 60%, a fidelity between the 93.7% and the 98.6% for the passive device and a complete reconfigurability of phases. The electrical power to be dissipated on the chip to achieve such tunability was smaller than the critical one (thank to the good performance of the new electrodes), but considerably higher than the usual one observed for this kind of devices. This issue stems from two factors:

- the wavelength of the photons at which the device was supposed to work, that was doubled with respect to the one used in the testing of heaters,
- the high thermal cross-talk.

Clearly the first issue comes from specifications and not there is not much that can be done about it. The high thermal cross-talk was partially reduced (of about the 15%, from our estimation) removing the metallic bridge on the top surface of

the glass substrate, increasing the thermal resistance between the two "controlled" waveguides, but a non negligible crosstalk is still taking place across the glass.

A further improvement could come from the thermal isolation of waveguides, for example realizing some trenches on the top of the glass, between the two arms of a MZI. The optimal implementation of this idea consists in the realization of these trenches in the same fabrication step of waveguides. This could be done fabricating the waveguides "upside down" (i.e. close to the bottom surface of glass) and then removing material between them through water-assisted laser ablation[68] (see the Figure in the next page). If a good fabrication window for integrated optical devices close to the bottom surface was found for this kind of upside down fabrication, one could also think to skip the etching process with benefits both for the processing time and the mechanical properties of the sample.

Straight waveguides performing well in terms of transmission for photons at a wavelength of $780\ \mu m$ obtained with the approach described above have recently been fabricated in our laboratories, so there are possibilities to be explored in this sense. A main issues of this approach comes from the nonlinear optical effects that might take place in the sample (e.g. self focusing) and stemming from the thick amount of glass the writing beam is supposed to go through before being focused. This could result in a poor repeatability of the writing process. It was worth pointing out, though, that for what the state of the art is, we couldn't have achieved a high transmission for the straight waveguide, low bending losses for an acceptable curvature radius, a good repeatability of the fabrication process and a high reconfigurability without the etching step.

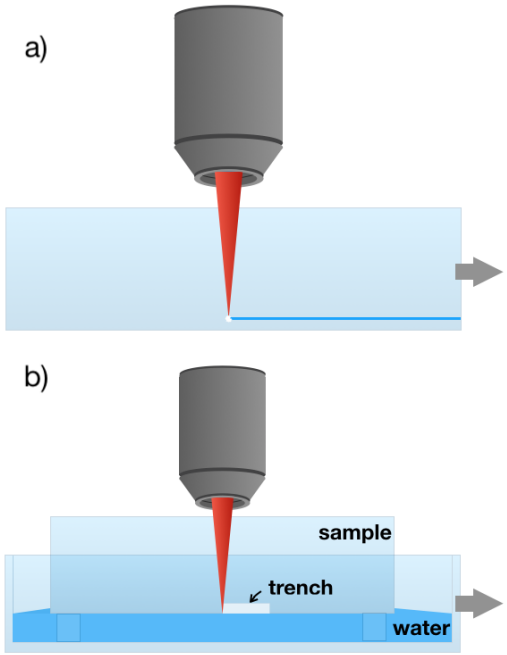

This figure shows a schematic of the two processes proposed as possible solutions to improve the state of the art technology. ***a****: after we verified the good performance of waveguides to a depth of* $295\ \mu m$*, good quality single mode straight waveguides working for photons at* $780\ \mu m$ *were fabricated in a borosilicate glass at a distance of* $30\ \mu m$ *from the bottom surface.* ***b****: the ablation of the material takes place at the bottom of the sample, making sure that the modified material is always below the focus position, so that the beam is not distorted*.

Bibliography

[1] R. P. Feynman, "Simulating physics with computers," *International Journal of Theoretical Physics*, vol. 21, 1982.

[2] A. Friedenauer, H. Schmitz, J. T. Glückert, D. Porras, and T. Schätz, "Simulating a quantum magnet with trapped ions," *Nature Physics*, vol. 4, pp. 757–761, 2008.

[3] K. Kim, M.-S. Chang, S. Korenblit, R. Islam, E. E. Edwards, J. K. Freericks, G.-D. Lin, L.-M. Duan, and C. Monroe, "Quantum simulation of frustrated ising spins with trapped ions," *Nature*, vol. 465, pp. 590–593, 2010.

[4] Z. Li, M.-H. Yung, H. Chen, D. Lu, X. P. J. D. Whitfield, A. Aspuru-Guzik, and J. Du, "Solving quantum ground-state problems with nuclear magnetic resonance," *Scientific Reports*, vol. 1, pp. 88 EP –, 2011.

[5] R. Hanson and D. D. Awschalom, "Coherent manipulation of single spins in semiconductors," *Nature*, vol. 453, pp. 1043–1049, 2008.

[6] J. Q. You and F. Nor, "Superconducting circuits and quantum information," *Physics Today*, vol. 58, p. (11) 42, 2005.

[7] X. song Ma, B. Dakic, W. Naylor, A. Zeilinger, and P. Walther, "Quantum simulation of the wavefunction to probe frustrated heisenberg spin systems," *Nature physics*, vol. 7, pp. 399–405, 2011.

[8] A. Crespi, R. Osellame, R. Ramponi, D. J. Brod, E. F. Galvao, N. Spagnolo, C. Vitelli, E. Maiorino, P. Mataloni, and F. Sciarrino, "Integrated multimode interferometers with arbitrary designs for photonic boson sampling," *Nature Photonics*, vol. 7, pp. 545 – 549, 2013.

[9] I. M. Georgescu, S. Ashhab, and F. Nori, "Quantum simulation," *arXiv:1308.6253v3*, 2014.

[10] A. Aspuru-Guzik and P. Walther, "Photonic quantum simulators," *Nature physics*, vol. 8, p. 285, 2012.

[11] C. K. Hong, Z. Y. Ou, and L. Mandel, "Measurement of subpicosecond time intervals between two photons by interference," *Phys. Rev. Lett.*, vol. 59, pp. 2044–2046, Nov 1987. [Online]. Available: https://link.aps.org/doi/10.1103/PhysRevLett.59.2044

[12] C. Abellán, A. Acín, A. Alarcón, O. Alibart, C. K. Andersen, F. Andreoli, A. Beckert, F. A. Beduini, A. Bendersky, M. Bentivegna, P. Bierhorst, D. Burchardt, A. Cabello, J. Cariñe, S. Carrasco, G. Carvacho, D. Cavalcanti, R. Chaves, J. Cortés-Vega, A. Cuevas, A. Delgado, H. de Riedmatten, C. Eichler, P. Farrera, J. Fuenzalida, M. García-Matos, R. Garthoff, S. Gasparinetti, T. Gerrits, F. Ghafari Jouneghani, S. Glancy, E. S. Gómez, P. González, J. Y. Guan, J. Handsteiner, J. Heinsoo, G. Heinze, A. Hirschmann, O. Jiménez, F. Kaiser, E. Knill, L. T. Knoll, S. Krinner, P. Kurpiers, M. A. Larotonda, J. Å. Larsson, A. Lenhard, H. Li, M. H. Li, G. Lima, B. Liu, Y. Liu, I. H. López Grande, T. Lunghi, X. Ma, O. S. Magaña-Loaiza, P. Magnard, A. Magnoni, M. Martí-Prieto, D. Martínez, P. Mataloni, A. Mattar, M. Mazzera, R. P. Mirin, M. W. Mitchell, S. Nam, M. Oppliger, J. W. Pan, R. B. Patel, G. J. Pryde, D. Rauch, K. Redeker, D. Rieländer, M. Ringbauer, T. Roberson, W. Rosenfeld, Y. Salathé, L. Santodonato, G. Sauder, T. Scheidl, C. T. Schmiegelow, F. Sciarrino, A. Seri, L. K. Shalm, S. C. Shi, S. Slussarenko, M. J. Stevens, S. Tanzilli, F. Toledo, J. Tura, R. Ursin, P. Vergyris, V. B. Verma, T. Walter, A. Wallraff, Z. Wang, H. Weinfurter, M. M. Weston, A. G. White, C. Wu, G. B. Xavier, L. You, X. Yuan, A. Zeilinger, Q. Zhang, W. Zhang, J. Zhong, and T. B. B. T. Collaboration, "Challenging local realism with human choices," *Nature*, vol. 557, no. 7704, pp. 212–216, 2018. [Online]. Available: https://doi.org/10.1038/s41586-018-0085-3

[13] D. Rauch, J. Handsteiner, A. Hochrainer, J. Gallicchio, A. S. Friedman, C. Leung, B. Liu, L. Bulla, S. Ecker, F. Steinlechner, R. Ursin, B. Hu, D. Leon, C. Benn, A. Ghedina, M. Cecconi, A. H. Guth, D. I. Kaiser, T. Scheidl, and A. Zeilinger, "Cosmic bell test using random measurement settings from high-redshift quasars," *Phys. Rev. Lett.*, vol. 121, p. 080403, Aug 2018. [Online]. Available: https://link.aps.org/doi/10.1103/PhysRevLett.121.080403

[14] C. Gerry and P. Knight, *Introductory Quantum Optics*. Cambridge University Press, 2005.

[15] S. Lloyd, "Universal quantum simulators," *Science*, vol. 273, no. 5278, pp. 1073–1078, 1996. [Online]. Available: http://science.sciencemag.org/content/273/5278/1073

[16] G. Ortiz, J. E. Gubernatis, E. Knill, and R. Laflamme, "Quantum algorithms for fermionic simulations," *Phys. Rev. A*, vol. 64, p. 022319, Jul 2001. [Online]. Available: https://link.aps.org/doi/10.1103/PhysRevA.64.022319

[17] L. García-Álvarez, I. L. Egusquiza, L. Lamata, A. del Campo, J. Sonner, and E. Solano, "Digital quantum simulaiton of minimal ads/cft," *arXiv:1607.08560v1*, 2016.

[18] C. Sparrow, E. Martín-López, N. Maraviglia, A. Neville, C. Harrold, J. Carolan, Y. Joglekar, T. Hashimoto, N. Matsuda, J. O'Brien, D. Tew, and A. Laing, "Simulating the vibrational quantum dynamics of molecules using photonics," *Nature*, vol. 557, 05 2018.

[19] *Principles of Quantum Computation and Information Vol.1*. World Scientific Publishing Co. Pte. Ltd., 2004.

[20] D. S. Abrams and S. Lloyd, "Quantum algorithm providing exponential speed increase for finding eigenvalues and eigenvectors," *Physical Review Letters*, 1999.

[21] A. Peruzzo, J. McClean, P. Shadbolt, M.-H. Yung, X.-Q. Zhou, P. J. Love, A. Aspuru-Guzikan, and J. L. O'Brien, "A variational eigenvalue solver on a quantum processor," *Nature Communications*, vol. 5, 2014.

[22] J. K. L. MacDonald, "On the modified ritz variation method," *Phys. Rev.*, vol. 46, pp. 828–828, Nov 1934. [Online]. Available: https://link.aps.org/doi/10.1103/PhysRev.46.828

[23] R. Santagati, J. Wang, A. A. Gentile, S. Paesani, N. Wiebe, J. R. McClean, S. Morley-Short, P. J. Shadbolt, D. Bonneau, J. W. Silverstone, D. P. Tew, X. Zhou, J. L. O'Brien, and M. G. Thompson, "Witnessing eigenstates for quantum simulation of hamiltonian spectra," *Science Advances*, vol. 4, no. 1, 2018. [Online]. Available: http://advances.sciencemag.org/content/4/1/eaap9646

[24] B. P. Lanyon, J. D. Whitfield, G. G. Gillett, M. E. Goggin, M. P. Almeida, I. Kassal, J. D. Biamonte, M. Mohseni, B. J. Powell, M. Barbieri, A. Aspuru-Guzik, and A. G. White, "Towards quantum chemistry on a quantum computer,"

Nature Chemistry, vol. 2, p. 106–111, jan 2010, n/a. [Online]. Available: http://www.nature.com/doifinder/10.1038/nchem.483

[25] E. Knill, R. Laflamme, and G. J. Milburn, "A scheme for efficient quantum computation with linear optics," *Nature*, vol. 409, pp. 46 EP –, 01 2001. [Online]. Available: https://doi.org/10.1038/35051009

[26] A. Politi, M. J. Cryan, J. G. Rarity, S. Yu, and J. L. O'Brien, "Silica-on-silicon waveguide quantum circuits," *Science*, vol. 320, no. 5876, pp. 646–649, 2008. [Online]. Available: http://science.sciencemag.org/content/320/5876/646

[27] A. Crespi, R. Ramponi, R. Osellame, L. Sansoni, I. Bongioanni, F. Sciarrino, G. Vallone, and P. Mataloni, "Integrated photonic quantum gates for polarization qubits," *Nature Communications*, vol. 2, pp. 566 EP –, 11 2011. [Online]. Available: https://doi.org/10.1038/ncomms1570

[28] G. Corrielli, A. Crespi, R. Geremia, R. Ramponi, L. Sansoni, A. Santinelli, P. Mataloni, F. Sciarrino, and R. Osellame, "Rotated waveplates in integrated waveguide optics," *Nature Communications*, vol. 5, pp. 4249 EP –, 06 2014. [Online]. Available: https://doi.org/10.1038/ncomms5249

[29] S. Atzeni, A. S. Rab, G. Corrielli, E. Polino, M. Valeri, P. Mataloni, N. Spagnolo, A. Crespi, F. Sciarrino, and R. Osellame, "Integrated sources of entangled photons at the telecom wavelength in femtosecond-laser-written circuits," *Optica*, vol. 5, no. 3, pp. 311–314, Mar 2018. [Online]. Available: http://www.osapublishing.org/optica/abstract.cfm?URI=optica-5-3-311

[30] G. Corrielli, S. Atzeni, S. Piacentini, I. Pitsios, A. Crespi, and R. Osellame, "Symmetric polarization-insensitive directional couplers fabricated by femtosecond laser writing," *Opt. Express*, vol. 26, no. 12, pp. 15 101–15 109, Jun 2018. [Online]. Available: http://www.opticsexpress.org/abstract.cfm?URI=oe-26-12-15101

[31] A. Crespi, "Integrated optical circuits for biosensing and quantum information by femtosecond laser microfabrication," Ph.D. dissertation, Politecnico di Milano, 2011.

[32] G. Corrielli, "Integrated photonic circuits by femtosecond laser writing for qubit manipulation, quantum cryptography and quantum-optical analogies," Ph.D. dissertation, Politecnico di Milano, 2015.

[33] S. Atzeni, "On-chip photon-pair sources by direct laser writing with a femtosecond laser," Master's thesis, Politecnico di Milano, 2016.

[34] S. Piacentini, "Femtosecond laser writing of polarization insensitive photonic circuits for quantum optics and astrophotonics applications," Master's thesis, Politecnico di Milano, 2018.

[35] R.Osellame, G.Cerullo, and R.Ramponi, *Laser Micromachining, Photonic and Microfluidic Devices in Transparent Material.* Springer, 2012.

[36] G. Corrielli, S. Atzeni, S. Piacentini, I. Pitsios, A. Crespi, and R. Osellame, "Symmetric polarization-insensitive directional couplers fabricated by femtosecond laser writing," *Optics Express*, vol. 26(12), pp. 15 101–15 109, 2018.

[37] J. F. Bauters, M. J. R. Heck, D. John, D. Dai, M.-C. Tien, A. L. Jonathon S. Barton, R. G. Heideman, D. J. Blumenthal, and J. E. Bowers, "Ultra-low-loss high-aspect-ratio si3n4 waveguides," *Optics Express*, vol. 19, no. 3163-3174, 2011.

[38] G. D. Valle, R. Osellame, and P. Laporta, "Micromachining of photonic devices by femtosecond laser pulses," *Journal of Optics A: Pure and Applied Optics*, vol. 11, 2012.

[39] J. L. M. MourouGandHuntAJ, "Optics at critical intensity applications to nanomorphing," *PNAS*, vol. 101, pp. 5856–5861, 2004.

[40] L. V. Keldysh, "Ionization in the field of a strong electromagnetic wave," *Soviet Physics*, vol. 20, pp. 1307–1314, 1965.

[41] T. Gorelik, M. Will, S. Nolte, A. Tuennermann, and U. Glatzel, "Transmission electron microscopy studies of femtosecond laser induced modifications in quartz," *Applied Physics A*, vol. 76, no. 3, pp. 309–311, Mar 2003. [Online]. Available: https://doi.org/10.1007/s00339-002-1813-x

[42] V. Apostolopoulos, L. Laversenne, T. Colomb, C. Depeursinge, R. P. Salathe, M. Pollnau, R. Osellame, G. Cerullo, and P. Laporta, "Femtosecond-irradiation-induced refractive-index changes and channel waveguiding in bulk ti 3 + : Sapphire," *Applied Physics Letters*, 2004.

[43] T. Johnston, "Beam propagation (m 2) measurement made as easy as it gets: the four-cuts method," *Applied Optics*, vol. 37(21), p. 4840, 1998.

[44] R. R. Gattass and E. Mazur, "Femtosecond laser micromachining in transparent materials," *Nature Photonics*, vol. 2, pp. 219–225, 2008.

[45] R. Osellame, N. Chiodo, V. Maselli, A. Yin, M. Zavelani-Rossi, G. Cerullo, P. Laporta, L. Aiello, S. D. Nicola, P. Ferraro, A. Finizio, and G. Pierattini, "Optical properties of waveguides written by a 26 mhz stretched cavity ti:sapphire femtosecond oscillator," *Optics Express*, vol. 13, p. 612, 2005.

[46] R.Osellame, M.Lobino, N.Chiodo, M.Marangoni, G.Cerullo, R.Ramponi, R. Thomson, H. Bookey, N. Psaila, and A. Kar., "Femtosecond laser writing of waveguides in periodically poled lithium niobate preserving the nonlinear coefficient," *Applied Physics Letters*, vol. 90, 2007.

[47] N. Psaila, R.R.Thomson, H.T.Bookey, N.Chiodo, S.Shen, R.Osellame, G. Cerullo, A. Jha, and A. Kar., "Er:yb-doped oxyfluoride silicate glass waveguide laser fabricated using ultrafast laser inscription," *IEEE Photonics Technology Letters*, vol. 20, pp. 126–128, 2008.

[48] G. Cerullo, R. Osellame, S. Taccheo, M. Marangoni, D. Polli, R. Ramponi, P. Laporta, and S. D. Silvestri, "Femtosecond micromachining of symmetric waveguides at 1.5 um by astig- matic beam focusing." *Optics Letters*, vol. 27, pp. 1938–1940, 2002.

[49] R. Osellame, S. Taccheo, M. Marangoni, R. Ramponi, P. Laporta, D. Polli, S. D. Silvestri, and G. Cerullo, "Femtosecond writing of active optical waveguides with astigmatically shaped beams." *Journal of the Optical Society of America*, vol. 20, pp. 1559–1567, 2003.

[50] Y.Cheng, K.Sugioka, K.Midorikawa, M.Masuda, K.Toyoda, M.Kawachi, and K. Shihoyama., "Control of the cross-sectional shape of a hollow mi- crochannel embedded in photostructurable glass by use of a femtosecond laser," *Optics letters*, vol. 28(1), pp. 55–57, 2003.

[51] M. Ams, G. Marshall, D. Spence, and M. Withford., "Slit beam shaping method for femtosecond laser direct-write fabrication of symmetric waveg- uides in bulk glasses." *Optics Express*, vol. 13(15), pp. 5676–5681, 2005.

[52] R.R.Thomson, A.S.Bockelt, E.Ramsay, S.Beecher, A.H.Greenaway, A. Kar, and D. Reid., "Shaping ultrafast laser inscribed optical waveguides using a deformable mirror." *Optics Express*, vol. 16(17), pp. 12 786–12 793, 2008.

[53] W.Yang, P.G.Kazansky, Y.Shimotsuma, M.Sakakura, K.Miura, and K.Hi-rao, "Ultrashort-pulse laser calligraphy," *Applied Physics Letters*, vol. 93 (17), p. 171109, 2008.

[54] A. Yariv, "Coupled-mode theory for guided-wave optics," *IEEE Journal of Quantum Electronics*, vol. 9(9), pp. 919–933, 1973.

[55] A. M. Streltsov and N. F. Borrelli, "Fabrication and analysis of a directional coupler written in glass by nanojoule femtosecond laser pulses." *Optics Letters*, vol. 26(1), pp. 42–43, 2001.

[56] R. Osellame, V. Maselli, N. C. andD. Polli, R. Martinez-Vazquez, R. Ramponi, and G. Cerullo., "Fabrication of 3d photonic devices at 1.55 m wavelength by femtosecond ti:sapphire oscillator." *Electronics Letters*, vol. 41, 2005.

[57] A. M. Kowalevicz, V. Sharma, E. P. Ippen, J. G. Fujimoto, and K. Minoshima, "Three-dimensional photonic devices fabricated in glass by use of a femtosecond laser oscillator," *Opt. Lett.*, vol. 30, no. 9, pp. 1060–1062, May 2005. [Online]. Available: http://ol.osa.org/abstract.cfm?URI=ol-30-9-1060

[58] K. Minoshima, A. Kowalevicz, E. Ippen, and J. Fujimoto, "Fabrication of coupled mode photonic devices in glass by nonlinear femtosecond laser materials processing," *Optics Express*, vol. 10(15), pp. 645–652, 2002.

[59] F. Flamini, L. Magrini, A. Rab, N. Spagnolo, V. D'ambrosio, P. Mataloni, F. Sciarrino, T. Zandrini, A. Crespi, R. Ramponi, and R.Osellame, "Thermally-reconfigurable quantum photonic circuits at telecom wavelength by femtosecond laser micromachining," *arXiv 1512.04330*, 2015.

[60] A. Beccari, "Reconfigurable integrated photonic circuits for quantum machine learning," Master's thesis, Politecnico di Milano, 2017.

[61] A. Killi, A. Steinmann, J. Dorring, U. Morgner, M. Lederer, D. Kopf, and C. Fallnich, "High-peak-power pulses from a cavity-dumped yb:ky(wo4)2 oscillator," *Optics Letters*, vol. 30(14), pp. 1891–1893, 2005.

[62] A. Arriola, S. Gross, N. Jovanovic, N. Charles, P. G. Tuthill, S. M. Olaizola, A. Fuerbach, and M. J. Withford, "Low bend loss waveguides enable compact, efficient 3d photonic chips," *Optics Express*, vol. 21(3), pp. 2978–2986, 2013.

[63] J. Gerratt, D. L. Cooper, P. B. Karadakov, and M. Raimondi, “Modern valence bond theory,” *Chem. Soc. Rev.*, vol. 26, pp. 87–100, 1997. [Online]. Available: http://dx.doi.org/10.1039/CS9972600087

[64] E. C. da Silva, J. Gerratt, D. L. Cooper, and M. Raimondi, “Study of the electronic states of the benzene molecule using spin-coupled valence bond theory,” *The Journal of Chemical Physics*, vol. 101, pp. 3866–3887, 1994.

[65] K. E. Haq, K. H. Behrndt, , and I. Kobin, “Adhesion mechanism of gold-underlayer film combinations to oxide substrates.” *Journal of Vacuum Science and Technology*, vol. 6, pp. 148–152, 1969.

[66] J. R. Rairden, C. A. Neugebauer, and R. A. Sigsbee, “Interdiffusion in thin conductor films — chromium/gold, nickel/gold and chromium silicide/gold,” *Metallurgical Transactions*, vol. 2, no. 3, pp. 719–722, Mar 1971. [Online]. Available: https://doi.org/10.1007/BF02662726

[67] Z. Chaboyer, A. Stokes, J. Downes, M. J. Steel, and M. J. Withford, “Design and fabrication of reconfigurable laser-written waveguide circuits,” *Opt. Express*, vol. 25, no. 26, pp. 33 056–33 065, Dec 2017. [Online]. Available: http://www.opticsexpress.org/abstract.cfm?URI=oe-25-26-33056

[68] H. Degawa, N. Urano, and S. Matsuo, “Laser fabrication of miniature internal thread in glass substrate,” *Micromachines*, vol. 8, no. 2, 2 2017.